Dissertation
submitted to the
Combined Faculties of the Natural Sciences and Mathematics
of the Ruperto-Carola-University of Heidelberg, Germany
for the degree of
Doctor of Natural Sciences

Put forward by

Peter Reimitz
born in Waiblingen
Oral examination: 04.11.2020

Phenomenology of sub-GeV Dark Matter

Monte-Carlo based developments and Search Strategies

Referees: Prof. Dr. Tilman Plehn
Prof. Dr. Björn Malte Schäfer

Abstract

The nature of dark matter is one of the most exciting questions of fundamental physics. In terms of a particle physics model the mass spectrum for possible dark matter candidates is huge. Extensive experimental programs seek to unveil the microscopic physics governing dark matter. While indirect and direct detection as well as collider searches have excluded a large class of dark matter models at the weak scale, the region below the GeV scale is relatively unexplored by these experiments. Therefore, it is particularly interesting to study the phenomenology of sub-GeV dark matter.

One of the leading constraints in the MeV to GeV range is expected to be set by indirect detection. However, a theoretical description of dark matter annihilation processes into Standard Model quarks is missing yet. In a Monte-Carlo based implementation in Herwig, we provide, for the first time, a modeling of these annihilations for dark matter models with vector mediators. This allows for a comprehensive study of sub-GeV dark matter annihilations in indirect detection searches.

In the sub-MeV mass range, low energy experiments and astrophysical as well as cosmological observations can set constraints on dark matter couplings to the Standard Model. If the dark matter candidate does not couple to the Standard Model Higgs, standard collider searches are not able to probe dark matter masses at the order of a few eV. We sytematically study a wealth of constraints on scalar and pseudoscalar dark matter candidates over a large range of dark matter masses. In addition, we introduce a novel search strategy at the LHC that extends the reach of complementary searches for light dark matter candidates.

Zusammenfassung

Die Beschreibung der Natur von Dunkler Materie ist eine der spannendsten Fragen der fundamentalen Physik. Das Massenspektrum für mögliche Dunkle-Materie-Kandidaten ist groß.

Unzählige experimentelle Projekte versuchen die mikroskopischen physikalischen Eigenschaften von Dunkler Materie zu enthüllen. Während indirekte und direkte Suchen, ebenso wie Experimente an Teilchenbeschleunigern, eine Reihe von Dunkle-Materie-Modellen an der elektroschwachen Skala ausgeschlossen haben, sind Massenbereiche unterhalb der GeV-Skala weitgehend unerforscht. Diesen Bereich phänomenologisch zu ergründen ist folglich besonders interessant.

Eine theoretische Beschreibung von Dunkle-Materie-Annihilationen in Standardmodell-Quarks fehlt bisher jedoch. In einer Monte-Carlo-basierten Implementation in Herwig bieten wir zum ersten Mal eine Modellierung dieser Prozesse für Dunkle-Materie-Modelle mit Vektoraustauschteilchen. Das ermöglicht eine umfassende Analyse von Dunkle-Materie-Annihilationen in indirekten Suchen unterhalb der GeV-Skala.

Im Bereich unterhalb von MeV-Massen können Niedrigenergiephysik-Experimente, astrophysikalische, sowie kosmologische Beobachtungen Dunkle-Materie-Kopplungen an das Standardmodell stark einschränken. Für den Fall, dass der Dunkle-Materie-Kandidat nicht an das Standardmodell-Higgsteilchen koppelt, können übliche Teilchenbeschleuniger-Suchen Dunkle-Materie-Teilchen mit eV-Massen bisher nicht testen. Wir untersuchen systematisch eine Vielzahl an Tests für skalare und pseudoskalare Dunkle-Materie-Kandidaten über einen großen Massenbereich. Darüber hinaus führen wir eine neue Art von Suchen am LHC ein, die die Reichweite von komplementären Suchen nach leichten Dunkle-Materie-Kandidaten erweitert.

Contents

Preface

The research presented in this thesis was conducted at the Institute for Theoretical Physics at Heidelberg University from October 2017 to August 2020. The contents of the Chapters 4 and 5 are based on work in collaboration with other authors and have previously been published as

[1] T. Plehn, P. Reimitz and P. Richardson,
"Hadronic Footprint of GeV-Mass Dark Matter",
SciPost Phys. **8** (2020), 092, `arXiv:1911.11147 [hep-ph]`

[2] M. Bauer, P. Foldenauer, P. Reimitz and T. Plehn,
"Light Dark Matter Annihilation and Scattering in LHC Detectors",
to appear in *SciPost Phys.*, `arXiv:2005.13551 [hep-ph]`

Finally, the author is involved in ongoing projects that have not been ready for publication at the time of writing this thesis.

1 | Introduction

Exploring the nature of dark matter (DM) is one of the biggest fundamental physics questions of our time. The existence of DM has been evidently proven from galactic scales up to cosmological scales. Besides, DM had a tremendous impact on the evolution of the Universe and shaped the present Universe through its gravitational interaction with luminous matter. Below the galactic scale, DM has evaded observations and its microscopic structure remains unresolved. In particular, there has not been any sign of non-gravitational interactions so far. In this thesis, we explore the phenomenology of DM models with DM masses in the range of 10^{-22} eV to $\mathcal{O}(1)$ GeV.

Guided by the great success of the Standard Model (SM) and standard cosmology, a microscopic particle physics model is a logical way to connect the dark and visible matter content of the Universe and explain macroscopic astrophysical observations. However, we know very little about its elementary properties in terms of a quantum field theoretical description. A wealth of Beyond the Standard Model (BSM) descriptions for DM exist. The mass of the DM agent ranges from $m_{\mathrm{DM}} = 10^{-22}$ eV up to masses of a 100 TeV, in some special cases even up to 10 solar masses as shown in Fig. 1.1. It is a big challenge for the DM community to systematically study a mass spectrum that covers more than 40 orders of magnitude. Each of these mass scales is related to a certain kind of DM production mechanism in order to reproduce the observed amount of DM in the Universe. Furthermore, the energy scale of DM processes is often determined by the DM mass. Thus, DM mass ranges can be probed by experiments that operate in the related energy region. To cover many orders of magnitude in DM masses experimental searches range from atomic spectroscopy in the sub-eV range via LHC experiments at the weak scale up to cosmic ray searches in the multi-TeV region.

Especially DM masses around the weak scale, down to the GeV scale, have been tested by the LHC in missing energy searches [3, 4] where the missing momentum is expected to be of the order of the DM mass. The same mass range is covered by relatively model-independent direct detection experiments [5]. In those experiments, one makes use of the local DM density in our galaxies and probes its recoils with detector materials in DM-SM scattering processes. Energy threshold for observing recoils, bound the mass reach of direct detection searches from below [6]. Standard indirect searches study possible annihilation or decay processes of DM into SM particles by looking at dense regions of the sky [7–10]. Those produced particles, if not already stable, decay into stable SM particles, i.e. $e^{\pm}, p/\bar{p}, \gamma, \nu$'s, at the end of a decay chain. Finally, these stable particles come with certain energy and hit telescopes or detectors. For DM masses above around 10 GeV, FERMI constrains these processes by studying signatures of photons in dwarf spheroidal galaxies [11, 12], while AMS covers leptonic final states [13, 14]. In addition, precision measurements of the Cosmic Microwave Background (CMB) [15] also set constraints on DM annihilation and decay process with their sensitivity to the total ionizing energy injected at the time of recombination. Particularly exciting is the sub-GeV DM mass range where the INTEGRAL telescope [16] is providing data and the eASTROGAM program will cover energies from 300 keV to 3 GeV [17].

On the theoretical side, the description of stable leptonic and hadronic DM annihilation products, i.e. $e^{\pm}, p/\bar{p}, \gamma, \nu$'s for indirect searches can be modeled by multi-purpose High-Energy-Physics (HEP) Monte Carlo generators like PYTHIA [18] and HERWIG [19]. The PPPC4DMID [20] tool provides energy spectra of stable final SM particles in tabulated form based on PYTHIA. Inspired by PPPC4DMID [20], standard DM tools like MICROMEGAS [21, 22], MADDM [23, 24], or DARKSUSY [25, 26] include similar tables or link their programs to PYTHIA directly. While current Monte-Carlo tools can cover DM annihilations to leptons from production threshold up to multi-TeV energies, DM annihilation into hadronic final

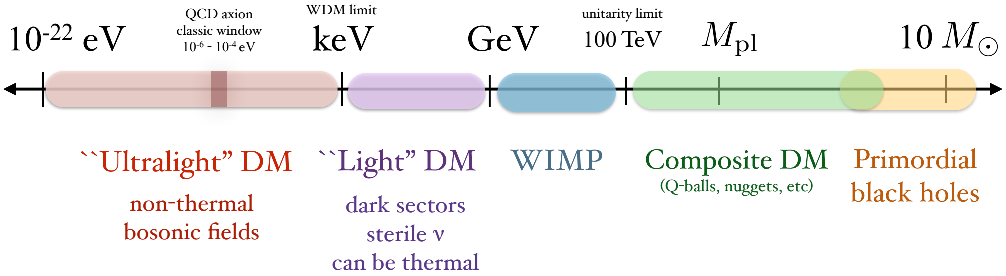

Figure 1.1: Mass range of DM candidates [27].

have not been available in Monte-Carlo generators below 5 GeV.

The production mechanism of DM depends on the DM mass. For DM models in the multi-GeV to TeV range that can be experimentally probed by the mentioned experiments, it is usually assumed that the DM candidate has been in thermal contact with SM particles at some point in the evolution of the Universe. Being part of a thermal bath, DM cannot be a relativistic degree of freedom from a certain age of the Universe onwards in order to be consistent with Big Bang Nucleosynthesis (BBN) [28, 29] and the formation of structures in the Universe. This sets a lower limit on the mass of thermal DM of about $m_{\mathrm{DM}} \gtrsim \mathcal{O}(1)$ MeV [30].

Lighter non-thermal DM can be fermionic or bosonic. The non-relativistic nature of DM nowadays with velocities fixed by the escape velocity of galaxies to $v \sim 10^{-3}$ leads to a direct translation of the DM momentum to its mass. For a fixed local DM mass density, the number density n_{DM} is increasing with decreasing mass. With a de Broglie wavelength λ_{dB} being inverse proportional to the DM mass and the number density, the occupation number scales like $\sim n_{\mathrm{DM}}\lambda_{\mathrm{dB}}^3 \propto m_{\mathrm{DM}}^{-4}$. As a consequence, below a few 100 eV, the DM candidate can only be bosonic due to the Pauli exclusion principle. While DM candidates with high masses and momenta are best described as particles, for $m_{\mathrm{DM}} \leq 1$ eV, the occupation is so huge that DM can be described as a classical wave. This non-thermal bosonic field is referred to as ultralight dark matter (ULDM) or fuzzy DM. In order to allow for galaxy-size structures its de Broglie wavelength cannot be larger than 100 kpc [31]. This sets a lower limit on ULDM masses of $m_{\mathrm{DM}} \gtrsim 10^{-22}$ eV. Search strategies for wave DM can often make use of the variation of fundamental constants due to an additional scalar degree of freedom. These variations can be probed in atomic spectroscopy [32–35], laser interference [36], Eot-Wash and ULDM-fifth-force experiments [37, 38].

In the end, it is a matter of taste and interest of where to enter the DM hunt. Multi-GeV to TeV DM candidates have been intensely under investigation by direct and indirect searches and collider-based experiments. Many models in that mass region have been excluded and thermally produced DM has been pushed more and more to the sub-GeV range. Forced by great experimental efforts, theoretical models and experimental searches of sub-GeV DM have become more popular recently. The phenomenology of sub-GeV is relatively new but is gaining more and more interest. We follow that line of research and study phenomenological implications of sub-GeV DM. Between ~ 10 MeV and 1 GeV, DM can still be thermal and DM annihilations can be related to its production mechanism in the Early Universe that explains the observed relic abundance of DM.

In Chapter 2 essential steps of the thermal history of the Universe. In Section 2.1, we introduce the basic concepts for calculating the evolution of number densities of particle species in the thermal bath of the Universe in order to determine their abundance today. In Section 2.2 , we discuss two crucial epochs, i.e. namely BBN and CMB, that every DM model has to be consistent with.

Besides its consistency with the thermal history of the Universe, DM models also have to pass constraints from direct and indirect detection and collider-based experiments. We explain the most prominent ways of searching for DM signals in those experiments in Chapter 3. In Section 3.1, we put special emphasis on the calculation of event rates in indirect detection. The chapter is complemented with low energy experiments probing ULDM and supernova constraints on light new particles.

In Chapter 4, we investigate annihilation channels of DM into quarks in the sub-GeV DM mass region. Indirect searches are expected to set one of the leading constraints in that mass range. The main assumption of indirect detection is that DM annihilations produce SM particles. In this context, the calculation of energy spectra of final stable remnants of DM annihilations is of particular importance. First, we present energy spectra of standard DM tools and show their limitations for lower DM masses in Section 4.1. A major technical problem is the description of annihilations in the hadronic resonance region of $\rho-, \omega-$ and $\phi-$mesons. We describe how to calculate DM annihilations into a vector mediator coupling to quarks for energies in the range of the hadronic resonance region. In Section 4.2, we present energy spectra for sub-GeV DM in a HERWIG-based implementation of these processes. We conclude the Chapter in Section 4.3 with directions of DM searches that would need these spectra as well as further tasks on the DM tool side.

On the lower edge of the mass spectrum $m_{\mathrm{DM}} \gtrsim 10^{-24}$ eV, more and more experimental searches have been proposed and some measurements can already cover a wide range of couplings of DM to the SM. In Chapter 5, we study the phenomenology of scalar and pseudoscalar ULDM candidates. Aside from the relatively model-independent $H \to$ inv. constraint, there hasn't been any LHC study dedicated to ULDM, yet. Therefore, we look at new scenarios of DM interactions inside LHC detectors. The DM can for instance be produced at the LHC in Higgs decays or through new mediators. The most promising signature is DM inelastic scattering off the detector material. It would leave displaced jets inside the detector. It is extremely unlikely that such signals appear as SM background. And they are fundamentally different from other displaced signatures such as displaced vertices from decaying massive particles or emerging jets [39]. We study in which way this LHC study can complement existing searches that probe ULDM.

In Chapter 6, we will summarize the results and give an outlook to further directions and ideas for exploring sub-GeV DM. The research described in this thesis investigates the phenomenology of DM in the mass range of 10^{-22} eV to $\mathcal{O}(1)$ GeV. In fact, we tackle both edges of that range and move towards intermediate masses. We provide a collection of astrophysical and cosmological observation as well as experimental searches that probe DM in the sub-GeV range. Furthermore, we extend phenomenological studies in that mass range. For one, we extend the theoretical basis of indirect detection searches by Monte-Carlo based developments in order to generate energy spectra for sub-GeV DM. This sets the ground for future indirect detection studies in the MeV to GeV mass range. For another, we introduce ULDM models to study a large number of constraints spanning over the whole sub-GeV range down to 10^{-22} eV. We are especially driven by the question of how the LHC could impact the parameter space for these models.

2 | Thermal History of the Universe

The evolution of the Universe is based upon the Friedmann-Robertson-Walker cosmological model, known as standard cosmology [40, 41]. It is describing the evolution of the Universe from the hot big bang until now. Looking out in space, we can see the history of the Universe unfolding in front of us. The isotropy of the CMB shows us that the matter of the Universe was distributed homogeneously in the Early Universe. From the CMB spectrum, we can tell that this matter was in causal contact in a primordial thermal bath. The measurement of rare abundances of particles that cannot be explained by solar processes allows us to speculate about even earlier times than the CMB. The validity of standard cosmology extends further back to the epoch of primordial nucleosynthesis where fossil abundances have been formed.

The theory of strong and electroweak interactions of the SM provides a profound basis for describing the fundamental interactions at very high energies in the early Universe. Equipped with the particle content of the SM and its fundamental forces, it is possible to deduce astrophysical and cosmological observations from first principles. The remarkable success of standard cosmology is linking thermal processes of microscopic physics at early times to macroscopic observations today. Whereas standard cosmology is predicting the abundancy of DM it is missing to provide a quantum field theoretical description for it. Under the assumption that DM is a particle, it is unclear if it was in thermal contact with the “primordial soup” of SM particles in the Early Universe.

In this chapter, we introduce some important steps of the thermal history of the Universe. In order to understand the measured abundances of elements today, we describe the evolution of number densities of particle species in Section 2.1. This involves a thermal freeze-out condition of particle processes. For the possibility of DM also interacting thermally with SM particles, we discuss possible structures of interaction cross-sections and their consequences on cosmology and astrophysics. We then take a closer look at BBN and the CMB in Section 2.2. We close the chapter with a discussion about the observed DM abundance in Section 2.3. Therein we elaborate on the properties a DM particle has to bring along to be a valid DM candidate.

2.1 Thermal Relics

The expansion of the Universe can be described by the scale parameter $a(t)$. More specifically, the Hubble parameter defined by $H \equiv \dot{a}(t)/a(t)$ encodes the rate at which space is expanding. The expansion is closely related to the total energy density ρ of the Universe via the first Friedmann equation that can be written like

$$H^2 = \frac{8\pi G}{3}\rho \tag{2.1}$$

for a flat Universe and the gravitational constant G. The total energy density budget ρ is the sum of radiaton ρ_r, contributions from matter ρ_m, and a vacuum energy contribution ρ_Λ. Each of them is dominant at a certain time in the Universe. The scaling of these contributions with a is determined by a continuity equation $\dot{\rho} + 3H(\rho + P)$ that is describing the evolution of the density of a fluid with a certain pressure P in the expanding Universe. The solutions for the continuity equation yield

$$\rho \approx \begin{cases} a^{-3} & \text{matter} \\ a^{-4} & \text{radiation} \\ a^{0} & \text{vacuum .} \end{cases} \tag{2.2}$$

The different scaling of $a(t)$ of radiation, matter, and the vacuum energy implies that the Universe was dominated by a single component at a certain time. In the following, we will work in a radiation-dominated Universe since all epochs discussed in this chapter fall into this era.

2.1.1 Time Evolution of Particle Number Densities

A number density can simply change by an expansion of the volume that surrounds these particles. Likewise, particle interaction can produce or annihilate particles. In the following, we discuss how particle species evolve in an expanding Universe. That implies a description of the thermodynamics of these particle in the thermal bath. To compute the time evolution of a number density n and energy density ρ, we consider a dilute and weakly-interacting gas of particles with g internal degrees of freedom, energy E and momentum $\mathbf{p}$. Whereas fermions follow the Fermi-Dirac statistics, bosons are described by the Bose-Einstein statistics. In both cases, the number density and energy density can be written like

$$\begin{aligned} n &= \frac{g}{(2\pi)^3} \int f(\mathbf{p}) \mathrm{d}^3 p \\ \rho &= \frac{g}{(2\pi)^3} \int E(\mathbf{p}) f(\mathbf{p}) \mathrm{d}^3 p \end{aligned} \tag{2.3}$$

with a phase space distribution function

$$f(\mathbf{p}) = \frac{1}{e^{(E(\mathbf{p})-\mu)/T} \pm 1}, \tag{2.4}$$

describing the occupation number in phase space for a given particle in kinetic equilibrium. The $(-)$ sign corresponds to bosons and the $(+)$ sign to fermions. $E(\mathbf{p}) = \sqrt{\mathbf{p}^2 + m^2}$ is the energy and μ is the chemical potential of the particle.

Relativistic Species In the ultra-relativistic regime where $T \gg m, \mu$ and $E \approx |\mathbf{p}| \equiv p$, we get

$$\begin{aligned} n &= \frac{g}{(2\pi)^3} \int_0^\infty \frac{4\pi p^2 \mathrm{d}p}{e^{p/T} \pm 1} = \begin{cases} \frac{3}{4\pi^2}\zeta(3) g T^3 & \text{for fermions} \\ \frac{1}{\pi^2}\zeta(3) g T^3 & \text{for bosons ,} \end{cases} \\ \rho &= \frac{g}{(2\pi)^3} \int_0^\infty \frac{4\pi p^3 \mathrm{d}p}{e^{p/T} \pm 1} = \begin{cases} \frac{7}{8}\frac{\pi^2}{30} g T^4 & \text{for fermions} \\ \frac{\pi^2}{30} g T^4 & \text{for bosons .} \end{cases} \end{aligned} \tag{2.5}$$

with the Riemann zeta function $\zeta(3) = 1.20206$.

For a radiation-dominated Universe, the Hubble parameter in eq. 2.1 can now be explicitly written as a sum over all relativistic densities $\rho_r = \sum_i \rho_i$

$$H = 1.66 g_*^{1/2} \frac{T^2}{M_P} \tag{2.6}$$

where $M_P = 1/G = 1.22 \times 10^{19}$ GeV is the Planck Mass and the temperature dependent relativistic number of degrees of freedom is given by

$$g_* = \sum_{\text{bosons}} g_i \left(\frac{T_i}{T}\right)^4 + \frac{7}{8} \sum_{\text{fermions}} g \left(\frac{T_i}{T}\right)^4 . \tag{2.7}$$

Once the mass of the particle is larger than the temperature and the particle becomes non-relativistic, g_* decreases. As a good approximation the expansion of the Universe can be treated adiabatically, so that the total entropy S is constant. With the second law of thermodynamics $T\mathrm{d}S = \mathrm{d}(\rho V) + P\mathrm{d}V$, the pressure-density relation for a relativistic gas $P = \frac{1}{3}\rho$ and continuity equation, the entropy density $s = S/V$ is

$$s = \sum_i \frac{\rho_i + P_i}{T_i} = \frac{2\pi^2}{45} g_{*s}(T) T^3 \ , \tag{2.8}$$

with the effective number of degrees of freedom in entropy $g_{*s} = \sum_{\text{bosons}} g\left(\frac{T_i}{T}\right)^3 + \frac{7}{8}\sum_{\text{fermions}} g\left(\frac{T_i}{T}\right)^3$. The conservation of entropy implies that $s \propto a^{-3}$ and $g_{*s}(T)T^3a^3 = \text{const}$. As long as relativistic particle species are not at the threshold of becoming non-relativist, we can assume g_{*s} to be constant and $T \propto a^{-1}$.

Non-Relativistic Species In the non-relativistic limit, with $T \ll m$ and $T \ll m - \mu$, we can approximate $E = m + p^2/2m$ and consequently, the denominator of eq. 2.4 becomes $e^{(E-\mu)/T} \pm 1 \approx e^{(E-\mu)/T}$. In this case both bosons and fermions are described by Maxwell-Boltzmann statistics. For the number density, this yields

$$n = g\left(\frac{mT}{2\pi}\right)^{3/2} e^{-(m-\mu)/T} \ . \tag{2.9}$$

We see that for non-relativistic particles, the number density is exponentially suppressed by the Boltzmann-factor $e^{-m/T}$ for decreasing temperatures.

As the number density is the number of particle N per volume V, we expect the number density of a particle species in the Universe to scale like $n \sim N/V \sim N/a^3$ for an expanding Universe with the increasing scale-factor $a(t)$. With a constant number of particles, the number density would decrease and the gas would dilute. This also means that the number of particles in a comoving volume is constant, i.e.

$$\frac{\mathrm{d}}{\mathrm{d}t}(na^3) = 0 \Leftrightarrow \frac{\mathrm{d}n}{\mathrm{d}t} + 3Hn = 0 \tag{2.10}$$

if there are no processes that change the number density.

To describe number densities that are effected by interactions that produce or destroy these particles, we exemplary go through the case of the annihilation and production of one particle species χ into another particle species f. Later on, we relate that to certain particle processes, one of them being DM annihilation to SM particles. So far, we haven't specified the type of the particles χ and f. They could be Majorana or Dirac fermions, vector or scalar bosons. They can be elementary particles or even nuclear species like protons and neutrons. For now, we only assume that $m_\chi > m_f$. At high enough temperatures of the thermal bath, particles are able to annihilate as well as being produced

$$\chi\bar{\chi} \leftrightarrow f\bar{f} \ . \tag{2.11}$$

As the temperature decreases with time in the history of the Universe, it drops below $T < m_\chi$. From then onwards, there is not enough kinetic energy available anymore to produce χ in thermal equilibrium. Therefore, the process drops out of thermal equilibrium and goes preferably to the lighter particles

$$\chi\chi \rightarrow f\bar{f} \tag{2.12}$$

As a consequence, the χ number density n_χ drops very fast. This process with $m_\chi > m_f$ is possible as long as two χ particles can meet and annihilate to f particles. Since the Universe expands, the mean free path for χ is increasing and it is not likely that χ annihilations into f occur. Consequently, any reaction of the form of eq. 2.11 freezes out. The evolution of number densities in a comoving volume is depicted in Fig. 2.1.

The freeze-out condition that defines the time $x_f = m_\chi/T_f$ at which the process decouples from the thermal bath is given by

$$\Gamma \equiv \tau^{-1} \equiv \sigma_{\chi\chi} v_{\text{rel}} n_\chi \overset{!}{=} H \tag{2.13}$$

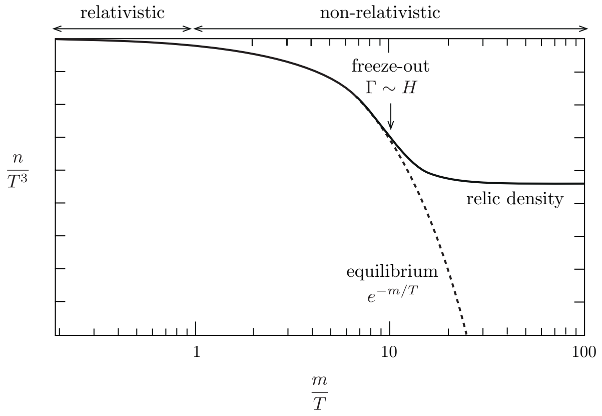

Figure 2.1: Freeze-out of a massive particle species [41]. With a decreasing temperature of the Universe, massive particle species become non-relativistic and its number density is therefor Boltzmann-suppressed. After freeze-out $\Gamma \sim H$, the comoving number density is slowly approaching its relic abundance value.

where v_{rel} is the relative velocity between the incoming particles, Γ the annihilation rate, and τ the mean free path of a χ particle in the thermal bath. Of particular importance here is to note that with a number density of a non-relativistic species as in eq. 2.9, we have an exponential x-dependence in the freeze-out condition in eq. 2.13. As also depicted in Fig. 2.1, the sharp drop of the equilibrium density tells us that the moment of freeze-out x_f cannot vary too much in order to reproduce a specific number density. To reproduce the observed DM abundance, this value should be around $x_f \sim 20$. In the following, we will take that as a reference value whenever we insert numbers into our calculations for DM estimates.

Once the process and its particles have decoupled from thermal equilibrium, its number densities mostly change due to the expansion of the Universe and little by further annihilations occurring. To be more precise, we have to include both effects to calculate the present abundance of that species. The depletion rate from χ-pair annihilations

$$\Gamma_{\text{ann.}} \sim \langle \sigma v_{\text{rel}} \rangle n_\chi^2 \tag{2.14}$$

describes the probability of χ-pair annihilations with a thermally-averaged χ-pair annihilation cross-section $\langle \sigma v_{\text{rel}} \rangle$. Including that into the time evolution of the number density yields the Boltzmann equation

$$\left(\frac{\mathrm{d}n_\chi}{\mathrm{d}t} + 3Hn_\chi \right) = -\langle \sigma v_{\text{rel}} \rangle (n_\chi^2 - n_{\text{eq.}}^2) \ . \tag{2.15}$$

It is convenient to define the densities normalized by the time dependent volume $a(t)^{-3}$. Since the entropy density scales like $s \sim 1/a^3$, we can define the yield as a fraction

$$Y = \frac{n_\chi}{s} \ . \tag{2.16}$$

Notice that the yield remains constant in the absence of number-changing processes. Its derivative is given by

$$\frac{\mathrm{d}Y}{\mathrm{d}t} = \frac{\mathrm{d}}{\mathrm{d}t} \left(\frac{a^3 n_\chi}{a^3 s} \right) = \frac{1}{s} \left(3Hn_\chi + \frac{\mathrm{d}n_\chi}{\mathrm{d}t} \right) \ . \tag{2.17}$$

This allows us to rewrite the Boltzmann equation as

$$\frac{\mathrm{d}Y}{\mathrm{d}t} = -s \langle \sigma v_{\text{rel}} \rangle (Y^2 - Y_{\text{eq.}}^2) \ . \tag{2.18}$$

With the dependencies $a \propto T^{-1}$ and $x \propto T^{-1}$, we conclude that $\frac{\mathrm{d}}{\mathrm{d}t}(a/x) = 0$ and hence, $\frac{\mathrm{d}x}{\mathrm{d}t} = Hx$. With dimensionless parameter $x = m_\chi/T$ and the particle species mass m_χ, we can define $H(x)$ as follows

$$H(x) = Hx^2 \equiv H(x=1)x^2 \ . \tag{2.19}$$

In its final form, the Boltzmann-equation for the evolution of particle yields can be written as

$$\begin{aligned}\frac{\mathrm{d}Y}{\mathrm{d}x} &= -\frac{sx\langle\sigma v_{\mathrm{rel}}\rangle}{H(x)}(Y^2 - Y_{\mathrm{eq.}}^2) \\ &= -\frac{\lambda\langle\sigma v_{\mathrm{rel}}\rangle}{x^2}(Y^2 - Y_{\mathrm{eq.}}^2)\end{aligned} \tag{2.20}$$

where we defined

$$\begin{aligned}\lambda &= \frac{2\pi^2}{45}\frac{M_P}{1.66}\frac{g_{*s}}{g_*^{1/2}}m_\chi \\ &\approx 0.26\frac{g_{*s}}{g_*^{1/2}}M_P m_\chi \ .\end{aligned} \tag{2.21}$$

Eq. 2.20 is the Riccati equation. Solutions are obtained numerically. For late times, $x \gg x_f$, we can assume that $Y \gg Y_{\mathrm{eq.}}$ simplifying the equation to

$$\frac{\mathrm{d}Y}{\mathrm{d}x} \approx -\frac{\lambda\langle\sigma v_{\mathrm{rel}}\rangle}{x^2}Y^2 \ . \tag{2.22}$$

Being a separable equation, we can integrate it from freeze-out time x_f up to nowadays $x_\infty \gg x_f$, i.e.

$$\int_{Y_f}^{Y_\infty} \mathrm{d}Y\frac{1}{Y^2} = \int_{x_f}^{x_\infty} \left(-\frac{\lambda\langle\sigma v_{\mathrm{rel}}\rangle}{x^2}\right) \ . \tag{2.23}$$

WIMP miracle We complete the discussion about the evolution of number densities with the example of a DM candidate that has been in thermal equilibrium at some point in the Early Universe. We assume that the annihilation cross section of DM $\langle\sigma v_{\mathrm{rel}}\rangle$ is independent of x. Furthermore, we expect the yield at DM freeze-out Y_f to be larger than the yield today $Y_\infty = Y_{\mathrm{DM}}$. For a rough estimate of the DM abundance, we can ignore the $1/Y_f$ boundary term in eq. 2.23 and finally obtain

$$Y_{\mathrm{DM}} = \frac{x_f}{\lambda\langle\sigma v_{\mathrm{rel}}\rangle} \ , \tag{2.24}$$

For the DM relic abundance, we get

$$\Omega_\chi h^2 \equiv \frac{\rho_{\mathrm{DM}}}{\rho_c}h^2 = \frac{m_{\mathrm{DM}}n_{\mathrm{DM}}}{\rho_c}h^2 = \frac{m_{\mathrm{DM}}Y_{\mathrm{DM}}sh^2}{\rho_c}, \tag{2.25}$$

where h is the dimensionless scaling factor for the Hubble expansion rate defined by $H_{\mathrm{today}} \equiv H_0 = 100\ h\ \mathrm{km\ s^{-1}Mpc^{-1}}$. Using the critical density $\rho_c = 1.053672 \cdot 10^{-5}h^2\ \mathrm{GeV\ cm^{-3}}$ [42], the measured value of the entropy $s = 2891.2\ \mathrm{cm}^{-3}$ [42], and $x_f \approx 20$ as a reference value, we can explicitly write out the relic density as

$$\begin{aligned}\Omega_\chi h^2 &\approx \frac{3\times10^{-27}\mathrm{cm^3s^{-1}}}{\langle\sigma v_{\mathrm{rel}}\rangle} \\ &\approx \frac{10^{-10}\mathrm{GeV}^{-2}}{\langle\sigma v_{\mathrm{rel}}\rangle} \ .\end{aligned} \tag{2.26}$$

It is easy to see that weak-scale cross-sections $\sigma \sim G_F^2 m_{\mathrm{DM}}^2 \sim 3\times10^{-26}\mathrm{cm^3s^{-1}}$ with the Fermi-constant $G_F \sim 10^{-5}\mathrm{GeV}^{-2}$ and DM masses of a few GeV's yield the correct relic abundance $\Omega_\chi h^2 \sim \mathcal{O}(10^{-1})$ for DM. It is the so-called WIMP-miracle of a weakly-interacting massive particle (WIMP) acting as DM. In the discussion about indirect detection signals in Section 3.1, we will use this weak-scale cross section as a reference value.

2.1.2 Velocity Dependence of Annihilation Cross Sections

For the case of DM we have assumed that the velocity-averaged cross section σv_{rel} is velocity-independent. This assumption is true as long as the leading term of the velocity expansion of the cross section is constant. Nevertheless, the constant contribution might be absent and $\langle\sigma v_{\mathrm{rel}}\rangle$ might be temperature dependent. In general, we can expand $\langle\sigma v_{\mathrm{rel}}\rangle$ in terms of x [43]. Following the calculations performed in [44], we write the non-relativistic thermal average as

$$\langle\sigma v_{\mathrm{rel}}\rangle = \frac{\int f(\mathbf{p}_1)f(\mathbf{p}_2)\sigma v_{\mathrm{rel}}\mathrm{d}^3p_1\mathrm{d}^3p_2}{\int f(\mathbf{p}_1)f(\mathbf{p}_2)\mathrm{d}^3p_1\mathrm{d}^3p_2} \ . \tag{2.27}$$

With the findings of Section 2.1.1, the thermally-averaged cross-section can be simplified to

$$\langle\sigma v_{\mathrm{rel}}\rangle = \frac{\int e^{-p_{\mathrm{tot}}^2/2mT}e^{-p_{\mathrm{rel}}^2/2mT}\sigma v_{\mathrm{rel}}p_{\mathrm{tot}}^2p_{\mathrm{rel}}^2\mathrm{d}p_{\mathrm{tot}}\mathrm{d}p_{\mathrm{rel}}}{\int e^{-p_{\mathrm{tot}}^2/2mT}e^{-p_{\mathrm{rel}}^2/2mT}\mathrm{d}p_{\mathrm{tot}}\mathrm{d}p_{\mathrm{rel}}} \tag{2.28}$$

where we have defined the total momentum $\mathbf{p}_{\mathrm{tot}} = \mathbf{p}_1 + \mathbf{p}_2$ and the relative momentum $\mathbf{p}_{\mathrm{rel}} = \mathbf{p}_1 - \mathbf{p}_2$. We introduce the kinetic energy per unit mass in the lab frame, ε, defined by

$$\varepsilon = \frac{s - 4m^2}{4m^2} \ . \tag{2.29}$$

For small velocities compared to the mass of the particles, we have $p_{\mathrm{rel}}^2 = s - 4m^2$ and hence, ε is related to the relative momentum via $p_{\mathrm{rel}}^2 = 4m^2\varepsilon$. The assumption of being able to perform that expansion breaks down around resonances or thresholds where new annihilation channels are opening. We expand σv_{rel} in powers of ε

$$\sigma v_{\mathrm{rel}} = \sum_{n=0}^{\infty}\frac{a^{(n)}}{n!}\varepsilon^n \tag{2.30}$$

where $a^{(n)}$ indicates the n-th derivative of σv_{rel} with respect to ε evaluated at $\varepsilon = 0$. Inserting that expansion into 2.28, we obtain the well-known result of the thermally-averaged cross-section in the non-relativistic limit

$$\langle\sigma v_{\mathrm{rel}}\rangle = a^{(0)} + \frac{3}{2}a^{(1)}x^{-1} + \frac{15}{8}a^{(2)}x^{-2} + \frac{35}{16}a^{(3)}x^{-3} + \mathcal{O}(x^{-4}) \ . \tag{2.31}$$

Often enough, it is sufficient to keep the temperature-independent component only, i.e. $\langle\sigma v_{\mathrm{rel}}\rangle \sim a^{(0)}$. Nevertheless, in some cases the constant term is absent and the thermally-averaged cross-section is dominated by its $a^{(1)}$-term. In order to see which terms dominate, we relate the cross-section to its non-relativistic expansion in terms of partial waves [45]

$$\sigma v_{\mathrm{rel}} \sim \sum_L c^{(L)}v_{\mathrm{rel}}^{2L}, \tag{2.32}$$

where L is the orbital angular momentum of the initial state DM pair. Implicitly, we already expanded the cross-section in terms of relative velocities when we look at eq. 2.30. We mentioned that the expansion parameter ε as defined in eq. 2.29, can be related to the relative momentum via $p_{\mathrm{rel}}^2 = m^2v_{\mathrm{rel}}^2 = 4m^2\varepsilon$. So with $\varepsilon = v_{\mathrm{rel}}^2/4$, both expansions 2.30 and 2.32 are just the same if we redefine the coefficients $a^{(n)} \to c^{(L)}$ and explicitly identify the summation index with the orbital angular momentum. This tells us that, with quantum number arguments, we can now already tell if the coefficients are zero or non-zero and might even be able to tell how they should scale with the mass scales of the process [46, 47]. The recipe for constructing annihilation matrix elements is very well described in [46]. It can be structured as follows

1. For each interaction structure, one can identify its transformations under charge conjugation C and parity P as well as identify the total angular momentum J quantum number.
2. We match those DM bilinears to SM final state bilinears with the same J quantum number.

DM bilinears	$^{(2S+1)}L_J\,(J^{PC})$
$\bar{\psi}\psi$	$^3P_0\,(0^{++})$
$i\bar{\psi}\gamma^5\psi$	$^1S_0\,(0^{-+})$
$\bar{\psi}\gamma^0\psi$	(0^{+-})
$\bar{\psi}\gamma^i\psi$	$^3S_1/^3D_1\,(1^{--})$
$\bar{\psi}\gamma^0\gamma^5\psi$	$^1S_0\,(0^{-+})$
$\bar{\psi}\gamma^i\gamma^5\psi$	$^3P_1\,(1^{++})$
$\phi^\dagger\phi$	$^1S_0\,(0^{++})$
$i\mathrm{Im}(\phi^\dagger\partial^0\phi)$	none
$i\mathrm{Im}(\phi^\dagger\partial^i\phi)$	$^1P_1\,(1^{--})$

Interaction Structure	velocity-suppressed?
$\bar{\psi}\psi\bar{q}q$	Yes
$\bar{\psi}\gamma^5\psi\bar{q}q$	No
$\bar{\psi}\psi\bar{q}\gamma^5 q$	Yes
$\bar{\psi}\gamma^5\psi\bar{q}\gamma^5 q$	No
$\bar{\psi}\gamma^\mu\psi\bar{q}\gamma_\mu q$	No
$\bar{\psi}\gamma^\mu\gamma^5\psi\bar{q}\gamma_\mu\gamma_5 q$	$\propto m_q^2/m_{\mathrm{DM}}^2$
$\phi^\dagger\phi\bar{q}q/\phi^2\bar{q}q$	No
$\phi^\dagger\phi\bar{q}\gamma^5 q/\phi^2\bar{q}\gamma^5 q$	No
$\phi^\dagger\partial_\mu\phi\bar{q}\gamma^\mu q$	Yes
$\phi^\dagger\partial^\mu\phi\bar{q}\gamma^\mu\gamma^5 q$	Yes

Table 2.1: Quantum numbers for two fermion-bilinears $\bar{\psi},\psi$ or scalar-bilinears $\phi^\dagger\phi/\phi^2$ in the initial states (left) and all possible interaction structures and velocity dependence's of annihilation cross section for fermionic SM bilinears in the final states (right)

3. Finally, we check if the matrix element is chirality suppressed by m_f/m_{DM}. Knowing J of the final states, we can get the J_z projections and find the possible helicities of the final state fermion and anti-fermion. If the SM bilinear cannot have fermions with the appropriate helicities, the annihilation cross section is suppressed.

For $2 \to 2$ annihilation processes, we look at the transformation under charge conjugation C and parity P given by

$$C : (-1)^{L+S} \quad P : (-1)^{L+1}, \tag{2.33}$$

for a fermion/anti-fermion pair in the initial states and

$$C : (-1)^{L+S} \quad P : (-1)^{L}, \tag{2.34}$$

for a boson/anti-boson pair in the initial states. We call $L = 0$ states s-wave, and $L = 1$ states p-wave referring to spectroscopic terminology. To give an explicit example, we go through the case of two DM fermions $\bar{\psi},\psi$ in the initial states. A more general treatment with scalar and vector particles can be found in [46]. Also using the spectroscopic notation $^{(2S+1)}L_J\,(J^{PC})$ with $L = S, P, D$ standing for $L = 0, 1, 2$, respectively, we list all possibilities of DM fermionic bilinears in the left table of Tab. 2.1. We now try to find final state SM bilinears with the same J quantum number. In the simplest case, we just consider fermionic bilinears $\bar{q}q$ again. So we can just combine all $J = 0$ DM bilinears with $J = 0$ SM bilinears and for the $J = 1$ states correspondingly. This yields the possibilities as given in the right table of Tab. 2.1. Interactions are velocity-suppressed if its initial states have $L = 1, 2, ...$ instead of $L = 0$ as in the unsuppressed case. Note that there won't be any C-odd DM bilinears with Majorana fermions since charge conjugation of Majorana fermions is always even. As one can see in Tab. 2.1, the axial vector bilinear combination is chirality-suppressed by m_f^2/m_{DM}^2. The axial vector bilinear with $^3P_1(1^{++})$ is an $L = 1$ velocity-suppressed mode. However, it also contains a pseudoscalar $^1S_0(0^{-+})$ component. One way to look at it is that the pseudoscalar coupling part is proportional to the final fermion mass m_f which yields a helicity-suppression of m_f^2/m_{DM}^2 [47]. Another way to understand it is that an odd number of Dirac matrices tells us that the fermions should be from different Weyl spinors in order to be able to build a SM bilinear. That includes that we have a $S_z = 0$ state. Nevertheless, from a $S = L = J = 1$ state, we only get fermion helicities from the same Weyl spinor. Hence, there will be a chirality flip arising from a mass-insertion. For the sake of completeness, we also added scalar DM bilinears to Tab. 2.1.

In calculations of the DM relic abundance or indirect detection constraints, the velocity-dependence plays a crucial role. For p-wave annihilation processes, $\langle\sigma v_{\mathrm{rel}}\rangle$ is suppressed by $x^{-1} = T/m_{\mathrm{DM}}$, which is a factor of $x_f^{-1} \sim \mathcal{O}(1/20)$ at DM freeze-out as discussed above. In indirect detection experiments probing DM annihilations in Galactic halos with DM velocities around $v \sim 10^{-3}$, p-wave annihilations yield suppressions of the order $x^{-1} \sim v^2 \sim \mathcal{O}(10^{-6})$. Hence, the velocity dependence of $\langle\sigma v_{\mathrm{rel}}\rangle$ can have large effects on late-time signatures and also influence DM annihilations at earlier times.

2.2 The Observable Early Universe

Two Early Universe epochs that are very well understood experimentally and theoretically are the BBN and the CMB [40]. Therefore, they set strong constraints on DM processes that could influence these epochs. In this section, we describe BBN and CMB in standard cosmology and indicate in which way DM contributes or could influence both scenarios.

2.2.1 Big Bang Nucleosynthesis

BBN marks the earliest testable era of the Universe through measurements of fossil SM elements. It occurred at $t \sim 0.01 - 100$ s after the Big Bang. That translates to temperatures from 10 MeV down to 0.1 MeV. BBN describes the production of the first light elements. In the case of Helium-4 (^{4}He) and Deuterium (D) no other astrophysical processes can account for their observed substantial abundances. BBN produces about 5 times more ^{4}He than stellar processes altogether. For D, the abundance is very low. But any other astrophysical processes destroy the weakly-bounded D which burns at relatively low temperatures of $T \sim 0.5 \cdot 10^6$ K. BBN also determines precisely the baryon density. For $\Lambda_B \sim 1$, we would expect an underproduction of D and an overproduction of ^{4}He and ^{7}Li. The initial phase setting the starting condition for BBN can be separated into three major steps. At around $T = 10$ MeV, protons p and neutrons n were almost equally abundant, i.e. $n/p \sim 1$. The balance was maintained by the processes

$$\begin{aligned} n &\leftrightarrow p + e^- + \bar{\nu}_e \\ \nu_e + n &\leftrightarrow p + e^- \\ e^+ + n &\leftrightarrow p + \bar{\nu}_e \ . \end{aligned} \tag{2.35}$$

When these interactions are in chemical equilibrium, we have

$$\mu_n + \mu_\nu = \mu_p + \mu_e \ . \tag{2.36}$$

As outlined Section 2.1, the number density of a non-relativistic nuclear species $A(Z)$ with mass number A and charge Z in kinetic equilibrium can be written

$$n_A = g_A \left(\frac{m_A T}{2\pi}\right)^{3/2} \exp\left(\frac{\mu_A - m_A}{T}\right) \ . \tag{2.37}$$

With the nuclear chemical potential $\mu_A = Z\mu_p + (A-Z)\mu_n$ and the definition of the binding energy $B_A \equiv Zm_p + (A-Z)m_n - m_A$, we can rewrite the number density in terms of the proton and neutron densities, n_p and n_n as

$$n_A = g_A A^{3/2} 2^{-A} \left(\frac{2\pi}{m_n T}\right)^{3(A-1)/2} n_p^Z n_n^{A-Z} \exp(B_A/T) \tag{2.38}$$

Similar to introducing the particle yield Y as done in eq. 2.16, it is useful to define quantities that are independent of the scale factor $a(t)$. We define mass fractions

$$X_A \equiv \frac{n_A A}{n_N} \tag{2.39}$$

of the total nucleon density $n_N = n_n + n_p + \sum_i (An_A)_i$. It implies that $\sum_i X_i = 1$. For the neutron-to-proton ratio, it follows that

$$\frac{n}{p} \equiv \frac{n_n}{n_p} = \frac{X_n}{X_p} = \exp\left(-\frac{Q_{np}}{T} + \frac{\mu_e - \mu_\nu}{T}\right) \tag{2.40}$$

where the neutron-proton mass difference can be approximated as $Q_{np} = m_n - m_p = m_d - m_u + \alpha\Lambda_{\mathrm{QCD}}$. We expect $\mu_e/T, \mu_\nu/T \ll 1$ [40] and therefore take

$$\left(\frac{n}{p}\right)_{\mathrm{EQ}} = \exp(-Q/T) \ , \tag{2.41}$$

for the equilibrium value of the neutron-to-proton ratio. Using eq. 2.38, the equilibrium nuclear abundances for Deuterons X_2, Helium-3 X_3, Helium-4 X_4, and metals like ^{12}C denoted by X_{12} are given by

$$\begin{aligned} X_2 &= 16.3(T/m_N)^{3/2}\eta \exp(B_2/T) X_n X_p \\ X_3 &= 57.4(T/m_N)^{3/2}\eta^2 \exp(B_3/T) X_n X_p^2 \\ X_4 &= 113(T/m_N)^{9/2}\eta^3 \exp(B_4/T) X_n^2 X_p^2 \\ X_{12} &= 3.22 \cdot 10^5 (T/m_N)^{33/2}\eta^{11} \exp(B_{12}/T) X_n^6 X_p^6 \ . \end{aligned} \tag{2.42}$$

With the baryon-to-photon ratio $\eta \equiv \frac{n_N}{n_\gamma} \ll 1$ being very small, all additional nuclear species are suppressed. It is noteworthy that the different scaling of the neutron and proton mass ratios $X_{n/p}$ shows that the value of the ratio n/p is also playing a role in determining the relative abundances of species. In thermal equilibrium and temperatures at around $T \sim 10$ MeV, we expect $X_n \simeq X_p \simeq 0.5$ and get

$$\begin{aligned} X_2 \simeq 6 \cdot 10^{-12}, \quad X_3 \simeq 2 \cdot 10^{-23} \\ X_4 \simeq 2 \cdot 10^{-34}, \quad X_{12} \simeq 2 \cdot 10^{-126} \end{aligned} \tag{2.43}$$

To estimate the temperature at the weak interaction freeze-out T_{weak}, we use the general freeze-out condition as introduced in eq. 2.13 with the interactions as defined in eq. 2.35, i.e. $\Gamma_{pe\to\nu n}$. One finds that

$$\Gamma_W/H \sim (T_F/0.8 \text{ MeV})^3 \tag{2.44}$$

for $T \gtrsim m_e$. More precise calculations [48] yield a weak freeze-out temperature of

$$T_F = \frac{b m_W^{4/3} \sin^{4/3}(\theta_W)}{\alpha^{2/3} M_{\mathrm{Pl}}^{1/3}} \approx 0.75\,\mathrm{MeV} \ . \tag{2.45}$$

At that time, we have

$$\left(\frac{n}{p}\right)_W = \exp\left(-\frac{Q}{T_W}\right) \simeq \frac{1}{6} \ . \tag{2.46}$$

After that, weak interactions only occur occasionally and n/p decreases further dominated by free neutron β-decays. Finally the neutron-to-proton ratio becomes $(n/p)_{\mathrm{BBN}} \sim 1/7$. At that time, we expect the nuclear species to be still in nuclear equilibrium with small abundances of

$$\begin{aligned} X_n \simeq 1/7, \quad X_p \simeq 6/7 \\ X_2 \simeq 10^{-12}, \quad X_3 \simeq 10^{-23} \\ X_4 \simeq 10^{-28}, \quad X_{12} \simeq 10^{-108} \ . \end{aligned} \tag{2.47}$$

For temperatures below $T < 0.5$ MeV, the mass fraction of ^{4}He is expected to rapidly increase and reach unity in nuclear equilibrium. Nevertheless, at around $T \sim 0.5$ MeV it first falls below its equilibrium value. Although the abundances of other light nuclear species exceed their equilibrium value, the rates of processes that synthesize ^{4}He are not fast enough to provide enough “fuel” to produce ^{4}He. Another reason is that Coulomb-barrier suppression is beginning to become significant. At around $T \sim 0.1$ MeV, the abundances of D, ^{3}He, and ^{3}H reach order unity and produce enough ^{4}He to establish the equilibrium abundance. Once these abundances are build up, all neutrons will be pumped in the production of ^{4}He and the resulting mass fraction for ^{4}He is easily calculated with

$$X_4 \simeq \frac{4n_4}{n_N} = \frac{4(n_n/2)}{n_n + n_p} = \frac{2(n/p)_{\mathrm{BBN}}}{1 + (n/p)_{\mathrm{BBN}}} = 0.25 \ , \tag{2.48}$$

where we have used that $(n/p)_{\mathrm{BBN}} \simeq 1/7$.

Since after the freeze-out of weak interactions, mostly the neutron β-decay will change n/p, we can relate the proton-neutron ratio at BBN to the number densities at weak freeze-out via

$$\frac{n_{\mathrm{BBN}}}{p_{\mathrm{BBN}}} = \frac{n_W e^{-\Gamma_n t_{\mathrm{BBN}}}}{p_W + n_W(1 - e^{-\Gamma_n t_{\mathrm{BBN}}})} \,, \tag{2.49}$$

where Γ_n is the neutron decay rate. This will be of particular importance in the discussion of a DM background field causing variations in the fundamental constants of nature. Any change in the fine-structure constant α, the QCD scale Λ_{QCD}, the weak boson masses, or the quark masses changes the neutron decay rate, the weak freeze-out temperature and the neutron-to-proton ratio at weak freeze-out and at BBN which in turn influence the ^{4}He yield. The variation of $\frac{\Delta(n/p)_W}{(n/p)_W}$ and $\frac{\Delta\Gamma_n}{\Gamma_n}$ can be expanded in terms of these constants as [32]

$$\begin{aligned} \frac{\Delta(n/p)_W}{(n/p)_W} &= -0.13\frac{\Delta\alpha}{\alpha} - 2.7\frac{\Delta(m_d - m_u)}{(m_d - m_u)} - 5.7\frac{\Delta M_W}{M_W} + 8.0\frac{\Delta M_Z}{M_Z} \,, \\ \frac{\Delta\Gamma_n}{\Gamma_n} &= -1.9\frac{\Delta\alpha}{\alpha} + 10\frac{\Delta(m_d - m_u)}{(m_d - m_u)} - 1.5\frac{\Delta m_e}{m_e} + 10\frac{\Delta M_W}{M_W} - 14\frac{\Delta M_Z}{M_Z} \,. \end{aligned} \tag{2.50}$$

Finally for small values of $\Gamma_n t_{BBN}$ a possible deviation of the ^{4}He abundance can be traced as

$$\frac{\Delta X_4}{X_4} \approx \frac{\Delta(n/p)_W}{(n/p)_W} - \Delta\Gamma_n t_{BBN} \,. \tag{2.51}$$

For the case of DM only coupling to gluons, Eq. (2.51) becomes particularly simple and one can write [49]

$$\frac{\Delta X_4}{X_4} = \left(-\frac{Q_{np}}{T_W} + t_{\mathrm{BBN}}\frac{\partial_x P(x)}{P(x)}\right)\frac{\Delta Q_{np}}{Q_{np}} \approx 4.82\frac{\Delta Q_{np}}{Q_{np}} \,, \tag{2.52}$$

where $P(x)$ is the phase space in the neutron decay width [49].

To sum up, BBN predicts the primordial abundances of D, ^{3}He, ^{4}He by using standard cosmology and the Standard Model of particle physics. Although, one cannot measure the primordial abundances nowadays, one can measure the present-day abundances in selected astrophysical sites. From there, one can deduce its primordial abundances. Deuterium is very hard to produce and but easy to destroy. Therefore, the primordial abundance is expected to be at least the observed abundance of D. The limit on the D relative to hydrogen H of $D/H \gtrsim 10^{-5}$ is sensitive to the baryon-to-photon ratio η as seen in eq. 2.42. A lower limit on D/H directly translates to an upper limit $\eta \lesssim 10^{-9}$. As η is also related to the baryon abundance via $\eta \sim 2.68 \cdot 10^{-8}$, we can also set an upper limit on the baryon density. Helium-3 is much harder to destroy than D. One does not expect that the primordial abundance of ^{3}He exceeds the measurable pre-solar abundance of ^{3}He by more than a factor of 2. Furthermore, the burning of D produces ^{3}He. Combining both abundances of D and ^{3}He, one can set an upper limit on the ratio $(D + {}^3\mathrm{He})/H$. This can then be translated to a lower limit on η of roughly $\eta \gtrsim 4 \cdot 10^{-10}$.

We can see that only with the measured values of D and ^{3}He, the window for possible values of the baryon-to-photon ratio becomes really narrow with $4 \cdot 10^{-10} \lesssim \eta \lesssim 10 \cdot 10^{-10}$. The tiny fraction of produced $^7\mathrm{Li}/H \sim 10^{-10}$ leaves a small observable trace of ^{7}Li that cannot be explained in any other way than primordial nucleosynthesis. In fact, it is remarkable that the observed abundance of ^{7}Li is equal to the predicted abundance by big bang with a value of η in the limited range set by D and ^{3}He. Hence, consistently combining the results of D, ^{3}He, and ^{7}Li shrinks down the possible range of η even more. In the case of ^{4}He not all but a large part of the measured Helium-4 is expected to be coming from BBN. Measurements yield a value that agrees with its predicted value of around $X_4 \sim 0.25$.

The prediction of the ^{4}He abundance depends on the neutron-to-proton ratio n/p at weak freeze-out, the neutron decay time τ_n and the relativistic degrees of freedom g_*. The latter one would change with new light particles species not being part of the SM. Nevertheless, with limits on η, τ_n and the X_4 abundance, we can set an upper limit on g_*. This is often parameterized as the effective number of neutrino species N_{eff}. It stands for the number of species that contribute to the total energy density of radiation excluding photons. Current limits tell us that there should be less than four relativistic species, i.e. $N_{\text{eff}} < 4$. It is exactly the number of neutrino species in the SM. This sets a sharp limit on new light particles. For example, a thermal DM candidate with a typical freeze-out value of $x_f \sim 20$, should not have a mass lighter than ~ 10 MeV.

2.2.2 The Cosmic Microwave Background

The CMB is known to be the surface of last scattering at a redshift of about $z \sim 1100$ where the age of the Universe was 180 000 yrs. The measured wavelengths of the background radiation range from 0.1 cm to 70 cm consistent with a black body radiation at a temperature of 2.72548 ± 0.00057 K [50]. It can be translated to a photon number density of $n_\gamma \sim 422\text{cm}^{-3}$. Overall the CMB is very uniform with temperature fluctuations of $\Delta T/T \leq 10^{-4}$ on angular scales from 10 arc to 180°. This is the main evidence for an isotropic Universe already from early times onwards until nowadays. It sets strong cosmological requirements on how structures have to be formed. The most attractive explanation for the isotropy of the Universe is inflation [51].

The CMB can be split into three processes: recombination of matter, photon decoupling and the "freeze-in" of residual ionization. Before the CMB is released, matter and radiation are in equilibrium. At that time, there are rapid interactions between photons and electrons in the Universe. At the time of recombination electrons and protons combine in the process

$$p + e^- \to H + \gamma \tag{2.53}$$

and form hydrogen atoms H. As a consequence, the Universe becomes opaque and the number density of free electrons n_e drastically drops. According to eq. 2.9, we have

$$n_i = g_i \left(\frac{m_i T}{2\pi}\right)^{3/2} \exp\left(\frac{\mu_i - m_i}{T}\right), \tag{2.54}$$

for $T < m_i$ in thermal equilibrium. The index stands for $i = e, p, H$, m_i is the mass of the species, and μ_i its chemical potential. In chemical equilibrium, we have $p + e \to H + \gamma$ and therefore $\mu_p + \mu_e = \mu_H$. Hence, we can express the hydrogen number density as

$$n_H = \frac{g_H}{g_p g_e} n_p n_e \left(\frac{m_e T}{2\pi}\right)^{-3/2} \exp(B_H/T) \tag{2.55}$$

with the hydrogen binding energy $B_H \equiv m_p + m_e - m_H = 13.6$ eV. For the pre-exponential factor, we assumed $m_H \approx m_p$. The ionization fraction, i.e. the fraction of protons and electrons that haven't combined to hydrogen atoms, can be expressed as

$$X_e \equiv \frac{n_p}{n_B} \tag{2.56}$$

where $n_B = n_p + n_H$ is the total baryon number density. With $g_p = g_e = 2$, $g_H = 4$, $n_B = \eta n_\gamma$, and neutrality of the Universe $n_p = n_e$, we get an equilibrium fractional ionization of

$$\frac{1 - X_e^{eq.}}{(X_e^{eq})^2} = \frac{4\sqrt{2}\zeta(3)}{\sqrt{\pi}} \eta \left(\frac{T}{m_e}\right)^{3/2} \exp(B_H/T)\ . \tag{2.57}$$

One can loosely define recombination as the point when around 90% of all electrons have combined with protons, i.e. when $1 - X_e^{eq.} = 0.9$. We obtain [40]

$$T_{\text{rec.}} \sim 0.3 \text{ eV}, \tag{2.58}$$

which corresponds to $1+z \sim 1300$. The sharp drop of the electron number density during recombination is accompanied by a rapidly increasing mean free path for photons. Thus, recombination and photon decoupling occur practically simultaneously. Therefore, one can define the moment of recombination

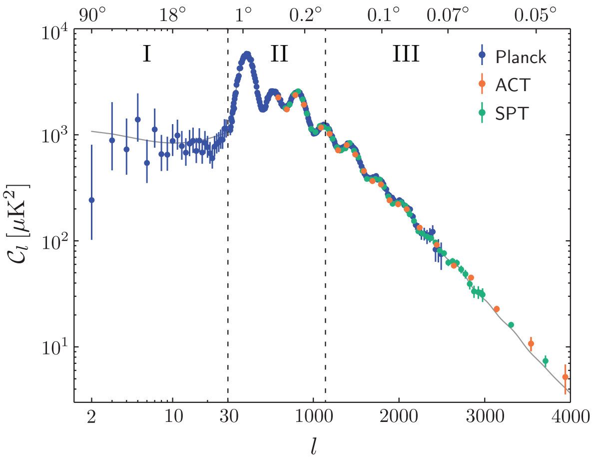

Figure 2.2: The three regimes of the CMB power spectrum [41]. Region I with angular resolutions $> 2°$ are determined by general relativistic effects. The intermediate range II describes oscillations of the photon-baryon fluid at the moment of last-scattering. At small scales, i.e. region III, fluctuations are damped when photon diffusion starts to become important.

and photon decoupling in the standard way with $\Gamma_\gamma \sim H$ where the interaction between photons and electrons is

$$\Gamma_\gamma = n_e \sigma_{\mathrm{T}}, \tag{2.59}$$

with the Thomson cross-section $\sigma_{\mathrm{T}} = \frac{8\pi\alpha^2}{2m_e^2} = 6.65 \cdot 10^{-25}$ cm^2. This more careful calculation yields $z \sim 1100$ and a temperature of $T_{\mathrm{dec.}} = 0.26$ eV. For $(1+z) \leq 1100$ the ionization fraction evolves in the same way as any abundance of a stable, massive particle species as described in Section 2.1.1.

To sum up, recombination of matter, the decoupling of radiation, and the "freeze-in" of residual ionization all occur around $1 + z = 1100$ corresponding to a temperature of $T = 0.26$ eV. After the photons have decoupled, they free-stream through the expanding Universe and cool down to $T_0 \sim 2.73\ K \sim 2.4 \cdot 10^{-4}$ eV.

The measurement of the CMB is hence the last scattering of photons with charged particles before the Universe was made up of neutral bound states. The CMB can be seen as a spherical projection of how the Universe looked like when it was 180 000 yrs old. All the information of the physics at that time is encoded in the temperature fluctuations. The temperature variations can be expressed in spherical coordinates by the expansion in spherical harmonics

$$\frac{\Delta T}{T} := \sum_{l=0}^{\infty} \sum_{m=-l}^{l} a_{lm} Y_{lm}(\theta, \phi) \ . \tag{2.60}$$

Squaring the temperature fluctuations and integrating over the solid angle Ω yields

$$\int \mathrm{d}\Omega \left(\frac{\delta T(\theta, \phi)}{T_0} \right)^2 = \sum_{lm} |a_{lm}|^2, \tag{2.61}$$

where we have used the relation $\int \mathrm{d}\Omega Y_{lm}(\theta, \phi) Y^*_{l'm'}(\theta, \phi) = \delta_{ll'} \delta_{mm'}$. The index m describes the angular momentum in one specific direction. Without any information about special directions in the CMB, we introduce the angular power spectrum

$$C_l := \frac{1}{2l+1} \sum_{m=-l}^{l} |a_{lm}|^2 \ . \tag{2.62}$$

The discrete values C_l can be seen as averaged values over m. Hence, we expect statistical fluctuations to cancel out for large l's, i.e. by averaging over many m's. The spherical harmonics can be expressed in terms of Legendre polynomials $P_l(\cos\theta)$ for which we have the roots

$$P_l(\cos\theta) = 0, \quad \leftrightarrow \cos\theta_l = \cos\left(\pi\frac{4k-1}{4l+2}\right) \ , \quad k = 1, ..., l \ . \tag{2.63}$$

The case $k = 1$ defines a relation between l and the angular resolution θ_l via [52]

$$\theta_l = \frac{3\pi}{4l} \tag{2.64}$$

for large l. If we now know the distance of the surface of last scattering to us, we could even make a statement about the spatial distances on the sphere. The distribution of C_l with respect to l consists of peaks that represent particularly large contributions to the temperature fluctuations. Just before recombination, the Universe was a tightly-coupled baryon-photon fluid, and DM which participated mostly gravitationally to the physics. DM produces gravitational wells and the baryon-photon fluid gets pulled into these regions. The baryon-photon fluid resists to collapse via pressure of the photons. The interplay between gravity and pressure sets up a sound wave in the fluid, and its physics are described by a forced harmonic oscillator. Such an oscillation produces a tower of modes with definite wave lengths. We assign these effects to the dominant peak structures in the power spectrum region from $2°$ to a few arc-minutes as seen in Fig. 2.2. Furthermore, we have the exponentially damped sub-arc-minute region. This is due to the breakdown of the assumption of a perfect fluid and photon diffusion starts to become important. If the scales are smaller than the mean free path of photons, the photons can stream out of over-densities and erase perturbations. The range with angular resolutions $> 2°$ are determined by general relativistic effects, for example the Sachs-Wolfe effect.

Fitting the standard cosmological model to the CMB power spectrum yields precise determination of cosmological parameters. Some of them are listed in Tab. 2.2. Among them, we find the measured value of the relic abundance $\Omega_{\rm DM}h^2 = 0.1200 \pm 0.0012$.

Quantity	Symbol	Value(uncertainty)
scaling factor for Hubble expansion	h	0.674(5)
DM density	$\Omega_{\rm DM}h^2$	0.1200(12)
redshift at matter-radiation equality	$z_{\rm eq}$	3402(26)
age at matter-radiation equality	$t_{\rm eq}$	51.1(8) kyr
redshift at which optical depth equals unity	z_*	1089.92(25)
age at which optical depth equals unity	t_*	372.9(10) kyr
age of the Universe	t_0	13.797(23) Gyr
eff. number of neutrino species	$N_{\rm eff}$	2.99(12)

Table 2.2: Some Cosmological parameters taken from [53] obtained by fitting standard cosmological parameters to the CMB power spectrum.

2.3 What We Know About Dark Matter

Astrophysical and cosmological observations have provided substantial evidence that point towards the existence of a non-luminous, transparent type of matter that is neither emitting nor absorbing light. All measurements in a wide range of astrophysical scales can be described by the inclusion of gravitationally interacting DM.

On the scale of galaxy clusters, the Bullet Cluster (1E 0657-558) is one example of a dynamical system that is influenced by DM. After the collision of two galaxy clusters, the visible components of the cluster show a characteristic shock wave as observed by X-ray telescopes. Through weak-lensing analyses though, one could observe that most of the mass of the system is displaced from the visible part. The accepted interpretation of this observation is that the DM components of the clusters have crossed without interacting significantly [54, 55].

On galactic scales, the most prominent example of how dynamical properties of astrophysical objects are effected by DM are rotation curves of spiral galaxies. Assuming a spherical distribution of matter in the bulge of the galaxy, the rotation velocity is described by $v = \sqrt{GM(r)/r}$ where G is the gravitational constant and $M(r)$ is the mass contained in a radius r. From the visible mass distribution of the spiral galaxy, we would expect a $v \propto r^{-1/2}$ dependence of the the velocity since the visible mass is not increasing in the outer parts of the galaxy. Vera Rubin's observations of rotation curves of spiral galaxies [56, 57] and later studies [58, 59] show that the velocity is only very slowly decreasing and that this flatness of the rotation curves can only be described by introducing a new matter component, with a mass distribution that is $M(r) \propto r$. This mass distribution is what one would expect for a self-gravitational gas of non-interacting particles.

On cosmological scales, DM left its footprint in the anisotropies of the CMB as discussed in chapter 2.2. Non-DM solutions to all these observations like modifications of Newtonian physics can address some problems at galactic scales but fail to describe other scales, i.e. at the level of clusters of galaxies or anisotropies of the CMB.

By now, we know that DM makes up $\sim 85\%$ of the matter density in the Universe and accounts for $\sim 25\%$ of the critical density of the Universe. Besides, DM interacts gravitationally. Assuming that DM is a particle, we can infer further information about the nature of DM. From numerical simulations of structure formation we know that DM already became non-relativistic early in the Universe. It should be electrically neutral, and if not, its electric charge has to be tiny [60]. It is non-baryonic and its lifetime should be larger than the age of the Universe in order not to interfere with the cosmological evolution of the Universe.

Nevertheless, the main particle properties of a DM are still unknown. What mass and spin does it have? What particle processes lead to the observed relic abundance of DM? Is there only one DM particle or is there a whole dark sector? The most important question is probably: Does DM interact with the SM? And if it interacts with the SM, how does the interaction look like? With that many unknown parameters, the variety of models that could describe DM is huge.

3 | Dark Matter Searches

A wealth of DM searches exist to explore the huge mass spectrum that DM candidates can lie in. Every one of them is covering a certain mass range and probes a particular underlying interaction structure. Whereas some searches might make use of the fact that DM can behave like a classical oscillating wave, others study the particle behavior of DM in scattering processes.

In order to understand the motivation behind the work explained in Chapter 4, we will discuss the general concepts behind indirect detection searches in Section 3.1. Furthermore, we present a set of constraints that DM models have to pass in order to be a valid DM candidate. Apart from indirect detection, this covers established search strategies like direct detection and collider searches in Section 3.2 and 3.3, respectively. Closely related to exploring the parameter space of light DM candidates, we give an overview over some low energy experiments in Section 3.4. Therein, we discuss in which way fundamental constants can be effected by oscillating DM fields and explain some necessary steps to calculate BBN constraints. We close the chapter with a description of how to calculate largely mass- and model-independent supernova bounds on light particle species.

3.1 Indirect Searches

Indirect searches for DM study possible visible products of DM interactions originating from the present DM of the Universe. In particular, it is the search of SM particles produced by DM decays or annihilations, and their effects. The big advantage of indirect detection compared to collider-based experiments is that we study the huge abundance of DM in the present Universe. SM final states could either produce signals in detectors or telescopes, or they could effect processes of the Early Universe. Hence, we split the discussion about indirect detection searches into two parts. In 3.1.1, we discuss standard indirect detection searches. That includes the observation of dense DM abundances with only few baryons like dwarf galaxies. DM annihilation processes in these objects could produce visible annihilation products that propagate to the Earth and are detected in telescopes. Another way of studying DM annihilations is to study the secondary effect of the produced particles on, for example, the CMB and BBN. That will be discussed in Section 3.1.2. Furthermore, in Section 3.1.3 we emphasize that energy spectra are an essential particle physics input for theoretical predictions of indirect detection bounds. We discuss the standard way of calculating those spectra and point out its limitations for certain energy ranges.

3.1.1 Standard Indirect Detection

At collider scales, one can assume that some of the final states and decay products in particle processes are stable. In indirect detection we are dealing with astrophysical scales and hence, everything that is not completely stable will decay at a certain time. The signatures that reach the detector are stable particles, i.e. electrons, positrons, protons, antiprotons, photons and neutrinos. We distinguish between two classes of final states, neutral and charged particles. Neutral particles, i.e. neutrinos and photons, travel approximately in straight lines towards the Earth. If we do not take into account the redshift information, i.e. the distance at which a photon was emitted, we only have a two-dimensional view of the sky. Hence, we only care about the number of photons or neutrinos N_0 that arrive in our detectors within a certain time interval dt, with a certain energy E, coming from a volume dV. The number of annihilations per unit volume is given by the depletion rate in eq. 2.14. For decaying DM, the number of decays per unit time per unit volume is determined by the standard decay law $\frac{\mathrm{d}N}{\mathrm{d}V} = n(\mathbf{r})(1-\exp(\Delta t/\tau_{\mathrm{DM}})) \simeq n(\mathbf{r})\frac{\Delta t}{\tau_{\mathrm{DM}}}$ for $\Delta t/\tau_{\mathrm{DM}} \ll 1$. In both annihilation and decay, the number of photons/neutrinos produced with a certain energy in one processes follows the distribution of the energy spectrum given by $\left(\frac{\mathrm{d}N_0}{\mathrm{d}E}\right)$. With a telescope or detector of area A, we get

$$\frac{\mathrm{d}N_0}{\mathrm{d}E\mathrm{d}t\mathrm{d}V} = \left(\frac{\mathrm{d}N_0}{\mathrm{d}E}\right)\frac{A}{4\pi r^2} \times \begin{cases} \frac{1}{2}\langle\sigma v_{\mathrm{rel}}\rangle n(\mathbf{r})^2 & \text{annihilation} \\ \frac{n(\mathbf{r})}{\tau_{\mathrm{DM}}} & \text{decay .} \end{cases} \tag{3.1}$$

Integrating over the line of sight and the solid angle, we obtain

$$\frac{\mathrm{d}N_0}{\mathrm{d}E\mathrm{d}t} = \frac{A}{4\pi}\left(\frac{\mathrm{d}N_0}{\mathrm{d}E}\right) \times \begin{cases} \frac{\langle\sigma v_{\mathrm{rel}}\rangle}{2m_{\mathrm{DM}}^2}\int \mathrm{d}r\mathrm{d}\Omega\rho(r)^2 & \text{annihilation} \\ \frac{1}{m_{\mathrm{DM}}\tau}\int \mathrm{d}r\mathrm{d}\Omega\rho(r) & \text{decay .} \end{cases} \tag{3.2}$$

This expression can be split into a particle physics part and an astrophysical part that is only determined by the distribution of the DM mass density $\rho(r)$, whereas the latter one can be predicted by N-body simulations and/or by gravitational measurements. For annihilations, we can write the spectrum as

$$\frac{1}{A}\frac{\mathrm{d}N_0}{\mathrm{d}E\mathrm{d}t} = \frac{\langle\sigma v_{\mathrm{rel}}\rangle}{m_{\mathrm{DM}}^2}\left(\frac{\mathrm{d}N_0}{\mathrm{d}E}\right)J_{\mathrm{ann}} \tag{3.3}$$

with the so-called “J-factor” of the DM source

$$J_{\mathrm{ann}} \equiv \frac{1}{8\pi}\int \mathrm{d}r\mathrm{d}\Omega\rho(\mathbf{r})^2 \ . \tag{3.4}$$

In general, the J-Factor sensitively depends on the density profile that we choose. For halos, a common choice is the Navarro-Frenk-White (NFW) profile $\rho \propto r^{-1}/(1 + r/r_s)^2$ [61], where r is the distance from the center of the halo and r_s a characteristic scale radius. As an example, dwarf satellite galaxies of the Milky way have J-factors of $J_{\mathrm{ann}} \approx 10^{17-20}$ GeV^2/cm^5. In the region within 1 degree of the Milky Way’s center the J-factor is even larger $J_{\mathrm{ann}} \approx 10^{22}$ GeV^2/cm^5. Nevertheless, astrophysical backgrounds in the region of the Galactic Center are also much larger. Therefore, it might be more challenging to distinguish potential signals from background. Dwarf galaxies instead only contain a few baryons and are hence, a relatively clean target for indirect detection. Another difference between the Galactic Center region and dwarf galaxies is the DM velocity distribution of both regions. The typical velocity of particles in dwarf galaxies is expected to be much smaller than in the Galactic Center. This would reduce the signal in velocity-suppressed annihilations such as p-wave annihilation and increase the annihilation rate in models with Sommerfeld enhancement. Besides, the density profile is sometimes not known precisely and does not take into account substructures that might lead to large enhancements of the J-factor. But the modeling of these dense substructures is highly uncertain and cannot even be resolved in some simulations below a certain mass scale.

For decaying DM, the substructure does not play a role. It is controlled by the density profile integrated over the distance r and the solid angle Ω, i.e. by $\int \rho(\mathrm{r})\mathrm{d}r\mathrm{d}\Omega$. That is essentially the total mass in a certain volume. For the simple case of a very distant object from our detector/telescope, the distant to every point is almost equal to $r \approx R$. So the integral becomes $\frac{1}{R^2}\int \rho(\mathbf{r})\mathrm{d}V = M/R^2$. We can see that the largest signals for decaying DM come from objects with larger total DM mass. In practice, the observation of galaxy clusters is the most promising way to witness decaying DM.

Rough Estimates

To get a feeling for what kind of physics could be tested with current indirect detection experiments, we roughly estimate the expected number of SM particles that might be detected in telescopes. Here, we closely follow [62].

Decaying DM: As a first case, we take a look at decaying DM. DM should be 'almost' stable to explain the present large DM abundance. And it cannot be enormously more abundant in the past at the time of recombination. A significant amount of DM decays from recombination until now would drastically change the well-measured CMB spectrum. Therefore, DM should be stable on scales of the age of the Universe, i.e.

$$\tau_{\mathrm{DM}} \gg \text{age of the Universe} \sim 1.4^{10}\ \mathrm{yr} \sim 10^{17}\ \mathrm{s}\ . \tag{3.5}$$

Such a large suppression of DM decays could be possible with operators that are highly suppressed at low energies. An obvious choice for operators that are highly suppressed are operators suppressed by the scale of a Grand Unified Theory (GUT) $M_{\mathrm{GUT}} \sim 2 \cdot 10^{16}$ GeV. As an example, we consider a dimension-6 operator with a DM candidate mass of $m_{\mathrm{DM}} \sim 1$ TeV. The operator will have a mass suppression of $1/M^2_{\mathrm{GUT}}$. The decay rate is consequently suppressed by $1/M^4_{\mathrm{GUT}}$. Based on dimensional arguments, we therefore have a decay rate $\Gamma_{\mathrm{DM}} \sim \frac{m^5_{\mathrm{DM}}}{M^4_{\mathrm{GUT}}}$. That gives us the lifetime

$$\tau_{\mathrm{DM}} \sim \frac{M^4_{\mathrm{GUT}}}{m^5_{\mathrm{DM}}} \sim \frac{(2 \cdot 10^{16}\ \mathrm{GeV})^4}{(10^3\ \mathrm{GeV})^5} \sim 10^{50}\ \mathrm{GeV}^{-1} \sim 10^{26}\ \mathrm{s} \sim 10^9 \times \text{ age of the Universe}\ . \tag{3.6}$$

Such large DM lifetimes do not cause any observable changes in the history of the Universe. Besides, there is no way that one can probe these DM decays at colliders for example. But can we see those decays in indirect detection?

For simplicity, we assume that one observable particle is produced in every decay, and the energy of the particle, whatever it is, is enough to be counted as a signal in the telescope. Hence, we do not have to "weigh" the number of particles in a certain time frame by the energy spectrum as in eq. 3.2. The rate of observable particles reaching a detector with area A at distance r from dV can be simplified to

$$\frac{\mathrm{d}N}{\mathrm{d}t} = \frac{A}{4\pi} \frac{1}{m_{\mathrm{DM}}\tau_{\mathrm{DM}}} \int \mathrm{d}r \mathrm{d}\Omega \rho(r)\ . \tag{3.7}$$

In the local DM halo with approximately constant $\rho_{\mathrm{DM}} \sim \frac{0.4\mathrm{GeV}}{\mathrm{cm}^3}$ within $R = 1$ kpc, the rate of observable particles is

$$\frac{\mathrm{d}N}{\mathrm{d}t} = A \left(\frac{0.4\ \mathrm{GeV}}{\mathrm{cm}^3}\right) \frac{1\ \mathrm{kpc}}{\tau_{\mathrm{DM}} m_{\mathrm{DM}}}\ . \tag{3.8}$$

With $\tau_{\mathrm{DM}} \sim 10^{26}$ s and $m_{\mathrm{DM}} \sim 1$ TeV, we expect $\frac{\mathrm{d}N}{\mathrm{d}t} = 10^{-4}\frac{1}{\mathrm{s}}$ events for $A = 1\ \mathrm{m}^2$. It would mean that a few thousand events reach the detector in a year. That could be visible in current indirect

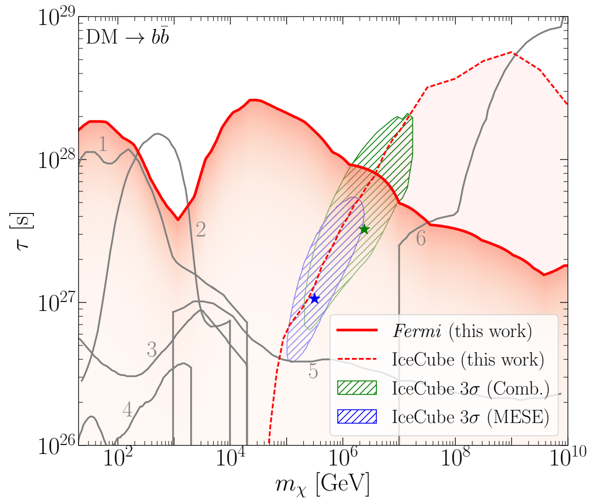

Figure 3.1: Constraints on DM decays to $\bar{b}b$ final states [74]. The numbers in the plot indicate bounds from Fermi (2,3,5), AMS-02 (1,4), and PAO/KASCADE/CASAMIA (6) [78–81].

detection experiments like AMS-02 [63–65] and IceCube [66–69], and earlier detectors like the Fermi Gamma-Ray Space Telescope (Fermi) [70, 71]. An exemplary plot for decaying DM limits can be found in Fig. 3.1. It is remarkable that combining measurements from several experiments is covering DM decay exclusion limits over a wide range of masses. For the sub-GeV range, leading constraints come from CMB [72], X/γ-ray telescopes [73, 74], and Voyager I [75, 76]. Using these measurements, decay constraint can be set around $\tau_{\rm DM} \gtrsim 10^{26}$ s as recently studied in [77] .

Annihilating DM: In case of annihilating DM, the rate of observable particles depends on the strength of the annihilation, i.e. the velocity-averaged annihilation cross section $\langle\sigma v_{\rm rel}\rangle$ that is producing those SM particles. As a reference value, we take the s-wave velocity-averaged cross section $\langle\sigma v_{\rm rel}\rangle \sim 10^{-9}$ GeV$^{-2} \sim 10^{-26}\ \frac{\rm cm^3}{\rm s}$ that is yielding the correct relic abundance as measured by Planck and estimated in Section 2.2. As in the case of the estimate for decaying DM, we take the local DM density as a reference value and integrate over a radius of 1 kpc. Again assuming that we produce one visible particle per annihilation with sufficient energy, eq. 3.2 becomes

$$\frac{{\rm d}N}{{\rm d}t} = \frac{A\langle\sigma v_{\rm rel}\rangle}{2}(1\ {\rm kpc})\frac{\rho_{\rm DM}^2}{m_{\rm DM}^2} \sim 10^{-26}\frac{\rm cm^3}{\rm s}A(1\ {\rm kpc})\left(\frac{0.4\ {\rm GeV}}{m_{\rm DM}}\right)^2 {\rm cm}^{-6}\ . \tag{3.9}$$

For a detector with $A = 1$ m^2 and a DM mass $m_{\rm DM} = 1$ TeV, one would expect roughly one event in a year and consequently not enough to observe it. Nevertheless, with decreasing mass the rate of observed particles is increasing since the number density is increasing and it is more probable that two DM particles meet and annihilate. Already for $m_{\rm DM} = 100$ GeV, a hundred events can be seen in a year. This is already close to the sensitivity limit of current indirect detection searches. This is not surprising by looking at the numbers that we used. Whereas the average local DM density might not be sufficiently dense for indirect detection, we integrate over a generously large radius of 1 kpc yielding a J-factor of $J_{\rm ann} = \frac{1\ {\rm kpc}}{2}\left(\frac{0.4\ {\rm GeV}}{\rm cm^3}\right)^2 \approx 10^{20}$ GeVcm^{-5} which is in the range of dwarf galaxies. Combining that with the generous assumption of one observable particle per annihilation gives us an observable rate. Note that the number of annihilations is increasing with decreasing mass. The $1/m_{\rm DM}^2$ dependence is a feature of annihilation processes since the depletion rate depends on the number density squared. More annihilations cause more detectable particles and as a consequence, strong bounds on DM annihilations can be obtained in the low-mass region for DM.

So far, we have assumed that the produced stable particles propagate to the Earth essentially undistorted. The indirect detection rates we presented and estimates we made should only give us a feeling about the expected rates in indirect detection experiments. We have outlined important ingredients that are needed to obtain those rates. However, particles might be redshifted or absorbed for more distant targets. For more dedicated studies, we refer to [82–86].

3.1.2 Effects on Early Universe Physics

Assuming that DM annihilations had taken place in the Early Universe, these interactions could also modify BBN and the CMB anisotropies, even after DM freeze-out. DM freeze-out only means that DM decouples from the thermal bath. Nevertheless, DM annihilations can still occur really rarely in an expanding Universe. We can approximate the evolution of the number of annihilations by its depletion rate given in eq. 2.14 in a co-moving volume V_c in one Hubble time

$$N_{\rm ann} \approx \frac{n_{\rm DM}^2\langle\sigma v_{\rm rel}\rangle}{2}V_c H^{-1} \propto \frac{\langle\sigma v_{\rm rel}\rangle}{1}a^{-3}H^{-1}\ . \tag{3.10}$$

We have used that the volume scales like $V_c \propto a^3$ and the number density as $n_{\rm DM} \propto a^{-3}$. For a radiation dominated Universe, we have $H \propto T^2$ as given by eq. 2.6. Knowing that $a \propto T^{-1}$, the number of annihilations per Hubble time in a radiation-dominated Universe scales with temperature like

$$N_{\rm ann} \propto \frac{\langle\sigma v_{\rm rel}\rangle}{2}a^{-1} \sim T \quad \text{rad. dominated,} \tag{3.11}$$

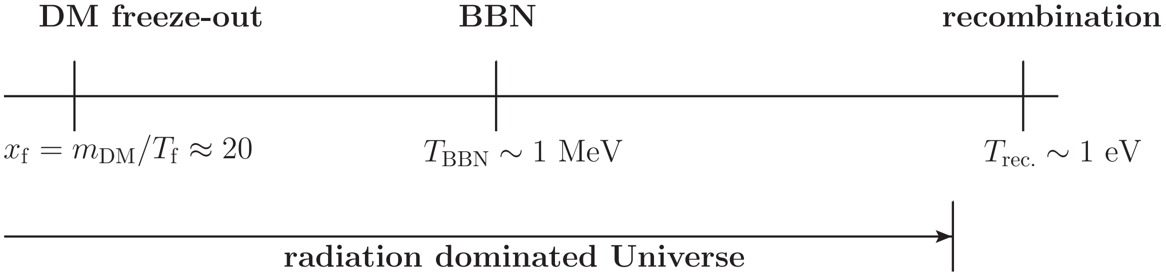

Figure 3.2: Early Universe physics timeline expressed in temperature dependence.

if we consider $\langle \sigma v_\mathrm{rel} \rangle$ to be x-independent, i.e. only the a^0-term in eq. 2.31 contributes.Note that this assumption breaks down for p-wave annihilating DM. We see that with the decreasing temperature of the Universe due to its expansion, the number of annihilations per Hubble time is decreasing as well. A timeline of the epochs is depicted in Fig. 3.2. As a reference value for the number of annihilations, we can consider its value at freeze-out $N_\mathrm{ann}(\text{freeze-out})$. From its definition in eq. 2.13, the freeze-out condition is $\Gamma_\mathrm{f} \sim \langle \sigma v_\mathrm{rel} \rangle n_\mathrm{DM} \overset{!}{=} H$ with an interaction rate Γ_f at freeze-out. Therefore, we expect one annihilation per Hubble time. If we assume the DM candidate mass to be $m_\mathrm{DM} = 100$ GeV, we have $T_f \approx 5$ GeV remembering that $x_f \approx 20$ at DM freeze-out. Consequently, the ratio of DM annihilations at BBN compared to freeze-out is

$$\frac{N_\mathrm{ann}(\mathrm{BBN})}{N_\mathrm{ann}(\text{freeze-out})} \sim \frac{T_\mathrm{BBN}}{T_\mathrm{f}} \sim \frac{1\ \mathrm{MeV}}{5\ \mathrm{GeV}} \sim 1/5 \cdot 10^{-3}\ . \tag{3.12}$$

In order to estimate how BBN is influenced by the annihilations, we have to consider the energy that is injected into BBN. Knowing that the DM abundance is 5 times the abundance of baryonic matter, the power injected at BBN is

$$N_\mathrm{ann}(\mathrm{BBN})\rho_\mathrm{DM} \sim \frac{1}{5} \cdot 10^{-3} \cdot 5 \cdot \rho_\mathrm{B} \sim 1\ \mathrm{MeV} \cdot n_\mathrm{B} \tag{3.13}$$

where $n_\mathrm{B} = \rho_\mathrm{B}/m_p$ is the number density of baryonic matter in the Universe with the proton mass $m_p \sim 1$ GeV. That means that roughly 1 MeV is injected in every baryon of the Universe. That could affect subdominant nuclear abundances produced during BBN.

For even later times, when the CMB is released, we expect the number of DM annihilations to be even less. Nevertheless, the impact these annihilations could have on the time of recombination are much more stringent than constraints on BBN for (sub-) GeV mass DM. As before, we can estimate the energy injected into the Universe at the time of recombination by considering the ratio

$$\frac{N_\mathrm{ann}(\mathrm{rec.})}{N_\mathrm{ann}(\text{freeze-out})} \sim \frac{1\ \mathrm{eV}}{5\ \mathrm{GeV}} \sim 1/5 \cdot 10^{-9} \tag{3.14}$$

and consequently

$$N_\mathrm{ann}(\mathrm{rec.})\rho_\mathrm{DM} \sim 1\ \mathrm{eV} \cdot n_\mathrm{B}\ . \tag{3.15}$$

For simplicity, we assumed that the Universe is radiation-dominated from freeze-out until CMB. This assumption is not strictly correct since matter-radiation equality is reached just before CMB. Nevertheless, it is sufficient to assume it for a rough estimate. Compared to the energy of 13.6 eV required to ionize a hydrogen atom, 1 eV per baryon would lead to the conclusion that DM annihilation could be able to ionize about 10 % of the hydrogen in the Universe. Every extra free electron or charged particle in the Universe after the time of recombination broadens the surface of last scattering for photons. As a consequence, the well-measured image of the CMB anisotropies would look different. That implies that we can set stringent constraints on DM annihilation. Of course not all the energy that is available through DM annihilation is finally ionizing hydrogen atoms. Only a fraction of the energy is converted to hydrogen ionization and is affecting the CMB. The effect can be calculated by public codes [87–91].

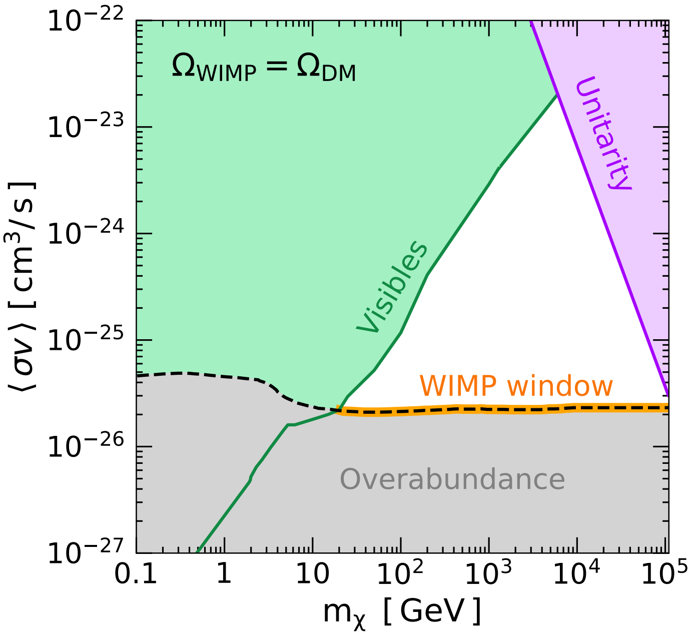

Figure 3.3: Bounds on generic thermal s-wave annihilating WIMP assuming that this process is explaining 100% of the DM [86]. The thermal relic cross section is the dashed line.

Besides, the electromagnetically interacting particles produced in these DM annihilations cool down. The cooling and its duration as well as the efficiency of the energy injection into ionization has been calculated in [85, 92]. A more detailed formula for calculating the energy injection is given by [83]

$$\left(\frac{\mathrm{d}E}{\mathrm{d}t\mathrm{d}V}\right)_{\text{deposited}} = (1+z)^6 \Omega_{\mathrm{DM}}^2 c^2 \rho_c^2 P_{\mathrm{ann}}(z) \tag{3.16}$$

with the DM model dependent annihilation parameter

$$P_{\mathrm{ann}}(z) = f(z) \frac{\langle \sigma v_{\mathrm{rel}} \rangle}{m_{\mathrm{DM}}} \; . \tag{3.17}$$

In the above formulae, z is the redshift, and Ω_{DM} the cosmological DM density as a fraction of the critical density ρ_c. $f(z)$ is a redshift dependent efficiency factor that characterizes the fraction of rest mass energy that is released into the gas. Its redshift dependence for annihilation processes is discussed in [84, 93, 94]. It has been pointed out that for annihilations only the excess ionization at redshift $z \sim 600$ is important. For decays, the signal is dominated by redshift $z \sim 300$ [72, 95]. As current CMB data is only sensitive to energy injection during a rather narrow range of redshifts $z \sim 1000 - 600$ one can neglect the redshift dependence and take f_{eff} to be constant in z. For electron and photon final states these constant coefficients have been calculated in [84] as a function of energy. Finally, given a certain DM model it is possible to calculate an effective efficiency factor that only depends on the DM mass via the electron and photon spectra

$$f_{\mathrm{eff}}(m_{\mathrm{DM}}) = \frac{1}{2m_{\mathrm{DM}}} \int_0^{m_{\mathrm{DM}}} E\mathrm{d}E \left[2 f_{\mathrm{eff}}^{e^+e^-}(E) \left(\frac{\mathrm{d}N}{\mathrm{d}E}\right)_{e^+} + f_{\mathrm{eff}}^{\gamma}(E) \left(\frac{\mathrm{d}N}{\mathrm{d}E}\right)_{\gamma} \right] \; . \tag{3.18}$$

These coefficients have been provided for various annihilation channels [84], however only down to DM masses of $\mathcal{O}(\mathrm{GeV})$ for reasons that will become clear later. As one can see in Fig. 3.3, the CMB and standard indirect detection searches put stringent constraints on GeV WIMPs. In the region below $m_\chi \lesssim 7$ GeV, CMB is most constraining. For energies above 7 GeV combined limits from Fermi and AMS provide the strongest indirect detection constraints up to masses of about a 1 TeV.

Nevertheless, the question is what these constraints really tell us. Let us summarize the assumptions that have been made to calculate the bounds as depicted in Fig. 3.3. They are:

- $\sigma v_{\rm rel}$ is dominated or fully determined by its velocity-independent term, i.e. we approximate $\langle\sigma v_{\rm rel}\rangle$ to be temperature-independent.
- the thermal relic abundance is determined by one single annihilation process.
- the total relic abundance is fully determined by thermal DM annihilation process(es).

So what do the exclusion plots like in Fig. 3.3 tell us? They only tell us that *the relic abundance is not determined by one single velocity-independent annihilation process*! So what happens if we have more than one annihilation process and one of them is velocity-suppressed? How much can a velocity-independent annihilation cross section contribute to the total relic abundance? Is the relic abundance of DM determined by a velocity-dependent cross section? Or one of them has SM final states that are invisible to ID searches? Or is the WIMP even only a sub-component of DM? Another possibility is that DM is not completely symmetric between particles and anti-particles. Sufficiently asymmetric DM weakens the constraints from CMB [96]. In conclusion, if we do not consider the simplest case of thermal DM existing of one annihilation process that is responsible for the total relic abundance of DM, ID constraints become weaker. In that case, especially the GeV/sub-GeV region of DM masses becomes interesting to study.

3.1.3 Particle Physics Input to Indirect Detection

Experimental searches have moved into the sub-GeV energy region such as the INTEGRAL telescope [16] or the eASTROGAM [17] program. On the theory side, however, these processes have only been studied for the case of leptonic final states for X-ray emissions [97] and p-wave annihilations [77]. For hadronic final states the sub-GeV DM mass region is almost unexplored yet. The main reason for this is that predictions for the energy spectra for the sub-GeV region were missing until recently.

An energy spectrum is showing how many stable particles of a specific type we expect to obtain with a certain energy in a DM annihilation process or decay. On astrophysical scales, the only stable particles are $e^{\pm}, p/\bar{p}, \gamma$ and $\nu/\bar{\nu}$'s. They can be produced directly or are the final particles of a longer decay chain in a particle process. So far the calculation of energy spectra is based on Monte-Carlo-Generator tools originally designed for high-energy physics experiments at the LHC. The procedure of these simulations [98] is always as seen in Fig. 3.4. In the following, we will focus on 2 → 2 particle

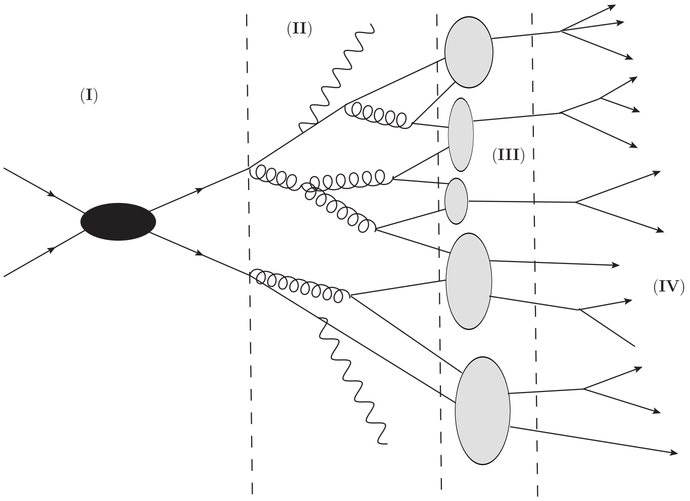

Figure 3.4: DM annihilations into quarks split into matrix element calculation (**I**), QED and QCD parton shower (**II**), hadronization (**III**), and decay of hadrons (**IV**).

processes. One starts at the matrix element level and calculates the perturbative process for a DM annihilation through a mediator decaying to two quarks. Next, the high-energetic final state quarks can radiate off gluons and the gluons can split into quark pairs or gluon pairs. That phase is called parton shower. The splitting of quarks into a quark and gluon $q \to q'g$ and gluon into a gluon pair $g \to gg$ or quark pair $q\bar{q}$ is determined by splitting functions. It is accompanied by the QED parton shower of emitting photons off quarks. Just as the matrix element calculation, parton shower calculations are in the perturbative regime. It is followed by hadronization that is already non-perturbative. As a last step, the mesons and baryons formed in the hadronization decay to stable particles if not already stable. At the end of that decay chain, usually pions decay into stable particles, either through $\pi^0 \to \gamma\gamma$, or $\pi^\pm \to \mu^\pm \overset{(-)}{\nu}_\mu \to e^\pm \overset{(-)}{\nu}_e \overset{(-)}{\nu}_\mu \overset{(-)}{\nu}_\mu$.

A user-friendly way of providing those spectra has been started by Pppc4dmid [20] where they compared the energy spectra obtained by Pythia [18] and Herwig [19] for a wide class of annihilation channels of 2 → 2 annihilations processes. Finally, Pppc4dmid decided to provide tabulated spectra based on Pythia simulations down to 5 GeV DM masses. Standard DM tools like micrOMEGAs [21, 22], MadDM [23, 24], or DarkSusy [25, 26] include similar, if not even the same spectra.

The problem that we are facing below 5 GeV DM processes is that there is no intermediate step of parton shower and transition from a perturbative matrix element to the non-perturbative regime. Below 5 GeV we can not start on a parton level and move to the hadron level. With energy scales that are close to Λ_{QCD}, we are already in the non-perturbative regime of QCD once the DM particles have annihilated. How to calculate energy spectra for those DM masses will be discussed in Chapter 4.

3.2 Collider Searches

Collider searches study the possibility of DM being produced in experiments instead of making use of the abundant DM in the Universe. Based on the interaction of the dark sector, DM models can be tested in searches of missing energy and exotic signatures such as displaced vertices or visible signatures of DM mediators. Both searches are based on the assumption that the DM or dark particle itself is electromagnetically and hadronically invisible, i.e. it does not leave any traces in the tracker and calorimeter systems.

Missing Energy Searches: If the DM particle has a lifetime large enough to escape the detector entirely, the only signature it will leave in the detector is missing energy. Similar to the approach of neutrino 'detection', energy-momentum conservation is applied to the visible objects of the collider process under study. For the case that energy-momentum is not conserved in a process, we expect additional particles to take part in the interaction. In particular, in a head-to-head collision of two particles moving along a beam-line, we expect the total transverse momentum of the process to be zero. We define the missing energy

$$\mathbf{E}^{\text{miss}} = -\sum_i \mathbf{p}_i^{\text{out}} \tag{3.19}$$

where $\mathbf{p}_i^{\text{out}}$ are the momenta vectors of the visible outgoing particles. The misleading name of *missing energy* is historically inherited from 'massless' neutrino searches. So strictly speaking we define missing momentum. Collider analysis usually look at observables in the transverse plane, in particular the missing transverse energy (MET). The major SM backgrounds in missing energy searches are processes including neutrinos and events with undetected leptons or mismeasured hadronic jets. Especially at hadron colliders, if only little MET is expected, it is hard to distinguish MET arising from invisible particles from mismeasurements of jets. The most prominent example of missing energy searches are so-called X+MET searches. DM models could contribute to this class of searches, for example, via $pp \to \chi\chi + X$ where X denotes a SM particle produced along with DM particles that are only seen through MET. These SM particles could be hadronic jets (Mono-jet), photons (Mono-photon), vector bosons (Mono-Z/W) or the Higgs (mono-Higgs) [4, 99].

In models in which the DM candidate couples to the SM Higgs, the Higgs can decay to a pair of DM particles given that the mass of the DM candidate satisfies $m_{\text{DM}} < m_h/2$. Hence, the decay

$h \to \chi\chi$ contributes to the invisible branching ratio of the Higgs boson. Compared to the strongly constrained $Z \to$ inv. searches by LEP [100], bounds on $H \to$ inv. are relatively weak. Indirectly, one can study this decay through combining all visible Higgs decay channels and set an upper bound on all unobserved decay modes. This requires an assumption on the Higgs production cross section that is typically given by the SM prediction. Alternatively, one can directly study the $h \to$ inv. process. The most sensitive channel is Higgs production in vector boson fusion in association with two jets [101, 102]. Other examples are gluon-fusion with an additional jet coming from initial state radiation, or associated production of a Higgs boson together with a massive vector boson. Combining all contributions, the strongest current limit on the branching ratio of Higgs to invisible final states for the LHC and future high-luminosity run of the LHC (HL-LHC) are

$$\begin{aligned} &\mathrm{BR}(h \to \ \mathrm{inv}) \lesssim 26\%, \ \text{(ATLAS)} \ \ [102] \\ &\mathrm{BR}(h \to \ \mathrm{inv}) \lesssim 19\%, \ \text{(CMS)} \ \ [101] \\ &\mathrm{BR}(h \to \ \mathrm{inv}) \lesssim 2\%, \ \text{(HL-LHC)} \ \ [103]. \end{aligned} \tag{3.20}$$

Minimizing the underlying assumptions and interpreting the LHC limits in an effective theory framework hardly changes this limit [104]. Note that bounds on the branching ratio $\mathrm{BR}(h \to \ \mathrm{inv})$ are relatively model-independent and don't even require the invisible particle to be DM. If the invisible state is far below the Higgs mass, we expect robust, mass-independent bounds on the couplings of the Higgs to the new particle.

Mediator Searches: DM models can also be probed without actually producing invisible particles. Simplified models always come with a DM mediator. If the mediator can be produced in interactions with quarks it can also decay to quarks. In this case, one can search for resonances on top of a smooth QCD di-jet background [99, 105, 106]. A challenge for LHC searches, is to trigger on events with low-p_T objects. Hence, di-jet searches lose sensitivity below mediator masses of roughly 1 TeV. One way out is to look for events with di-jets along with other SM particles. An example is a di-jet event with a high-p_T initial state radiation (ISR) object to trigger on. The mediator decay products form a single jet that is explored with jet substructure techniques. In that way LHC searches are sensitive to events with lower mediator masses.

Exotic Searches: MET searches can not be applied to co-annihilation/co-scattering scenarios of DM production at colliders. It does not feature substantial missing energy to be distinguished from the SM background. Nevertheless, if the DM candidate is part of a dark sector including several particles that are accessible at the LHC, these additional states can cause displaced vertices, e.g. displaced soft leptons [107–109].

Another possibility are emerging jets. Introducing a whole new dark gauge group coupled to QCD, one can end up with a zoo of unstable particles [39]. Just like in QCD, dark quarks shower, hadronize and form dark mesons and baryons. Some of them are stable and some of them decay back to the SM. If the decay is very slow, those mesons will first invisibly travel some distance. Once they turn into visible SM particles, jets will emerge in the detector.

In Chapter 5, we will discuss a new kind of signature that is fundamentally different from all collider signatures discussed above.

3.3 Direct Searches

Direct Detection (DD) searches essentially study the interaction of the local DM density in the Milky Way with the target material of an Earth-based detector. In particular, DD experiments study the movements of nucleons that are expected to be at rest in a very well-controlled laboratory environment. The SM background for these events is expected to be very low. This is a big advantage compared to indirect detection and collider searches where the DM topologies are usually accompanied by similar pure SM processes happening in the same astrophysical or collider physics environment. In DD

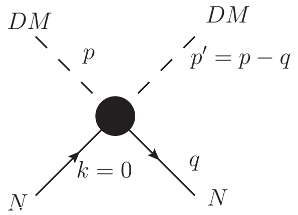

Figure 3.5: Kinematics of DM-nucleus scattering in direct detection experiments.

experiments, the background is very well under control. In a very quiet experimental environment it is possible to measure possible low-energy DM-SM scattering events in the sub-MeV energy range. In the following, we will go through the basic steps to calculate the scattering cross section in the non-relativistic limit [27]. The typical kinetic energy of a nucleus is of the order of kT, where the temperature T is usually far below room temperature. Hence, we can assume that the nucleus is initially at rest. With a process topology as in Fig. 3.5, the non-relativistic total initial and final energy read

$$E_i = \frac{\mathbf{p}^2}{2\,m_{\mathrm{DM}}}\;, \quad E_f = \underbrace{\frac{(\mathbf{p}-\mathbf{q})^2}{2\,m_{\mathrm{DM}}}}_{E_{\mathrm{DM}}} + \underbrace{\frac{\mathbf{q}^2}{2\,m_N}}_{E_R}, \tag{3.21}$$

where E_{DM} is the final DM energy and E_R is the recoil energy of the nucleus with a momentum transfer $\mathbf{q} = \mathbf{p} - \mathbf{p}'$. By defining $\cos(\theta) = \hat{\mathbf{p}} \cdot \hat{\mathbf{q}}$, and the reduced mass for the DM-nucleus system $\mu_{\mathrm{DM}N} = m_{\mathrm{DM}} m_N/(m_{\mathrm{DM}} + m_N)$, we get

$$\frac{\mathbf{p}\cdot\mathbf{q}}{m_{\mathrm{DM}}} = \frac{|\mathbf{p}||\mathbf{q}|\cos\theta}{m_{\mathrm{DM}}} = \frac{\mathbf{q}^2}{2\mu_{\mathrm{DM}N}}\;. \tag{3.22}$$

The maximal momentum transfer is then given for $|\mathbf{q}|_{\max} = 2\nu_{\mathrm{DM}N}|\mathbf{p}|/m_{\mathrm{DM}} = 2\nu_{\mathrm{DM}N}v$ and for the corresponding maximum recoil energy

$$E_R^{\max} = \frac{|\mathbf{q}|^2_{\max}}{2m_N} = \frac{2\mu^2_{\mathrm{DM}N}v^2}{m_N}\;. \tag{3.23}$$

It is easy to see that $E_R^{\max}$ is maximized for $m_{\mathrm{DM}} = m_N$ for fixed DM velocities [52]. Hence, we can expect the strongest constraints on DM if the DM candidate has a mass around the nucleus mass. Typically, we have $\nu_{\mathrm{DM}N} \simeq 10...100$ GeV and consequently $E_R^{\max} \simeq 20...200$ keV for a DM velocity of $v \sim 10^{-3}$. With the given definitions, the final state phase space can be written like [27]

$$\mathrm{d}\Phi_2 = \frac{|\mathbf{q}|^2\mathrm{d}|\mathbf{q}|\,\mathrm{d}\cos\theta\,\mathrm{d}\phi}{(2\pi)^2}\;\frac{1}{v_{\mathrm{DM}}\,|\mathbf{q}|}\delta\left(\cos\theta - \frac{|\mathbf{q}|}{2\,\mu_{\mathrm{DM}N}\,v_{\mathrm{DM}}}\right) \tag{3.24}$$

where we have used that $\mathbf{p} = m_\chi\,\mathbf{v}_\chi$. Now we can write the differential nucleon-DM scattering cross section as [27]

$$\mathrm{d}\sigma_N = \frac{|\mathcal{M}|^2}{4\pi(4m_{\mathrm{DM}}\,m_N)^2\,v_{\mathrm{DM}}^2}\;\mathrm{d}|\mathbf{q}|^2\,d\cos\theta\;\delta\left(\cos\theta - \frac{|\mathbf{q}|}{2\,\mu_{\mathrm{DM}N}\,v_{\mathrm{DM}}}\right)\;. \tag{3.25}$$

For the case of θ-independent squared matrix elements, the total scattering cross section is only an integral over the final nucleon momentum

$$\sigma_N = \int_0^{(2\,\mu_{\mathrm{DM}N}v_{\mathrm{DM}})^2} \mathrm{d}|\mathbf{q}|^2\left(\frac{|\mathcal{M}|^2}{4\pi(4m_{\mathrm{DM}}\,m_N)^2\,v_{\mathrm{DM}}^2}\right)\;. \tag{3.26}$$

Constraints are usually set on the DM-nucleon scattering cross section. Hence, once we calculated eq. 3.26 for specific models, we can constrain the models therein. A full calculation of the interaction rate for DM-nucleus scattering also includes the DM flux of the local DM density. This gives us an additional integration over the galactic DM velocity distribution [110]. It also implies an annual modulation of the DM signal due to the earth's revolution [110].

As a little preparatory work for Chapter 5, we go through matrix elements for DM-nucleon scattering where the DM candidate is either a scalar s or a pseudoscalar a. The matrix element of the effective partonic operator with asymptotic nucleon states is given by

$$\mathcal{M} = \langle N(k')|\mathcal{O}_{\text{eff}}|N(k)\rangle \,. \tag{3.27}$$

For light quarks, we can directly evaluate the nuclear matrix element

$$\langle N(k')|m_q\,\bar{q}q|N(k)\rangle = m_N\; f^n_{T,q}\;\bar{u}_N(k')\,u_N(k)\,. \tag{3.28}$$

In the case of heavy quarks we will integrate out the heavy quark fields via the QCD trace anomaly,

$$m_q\,\bar{q}q \to -\frac{\alpha_s}{12\pi}\,\text{Tr}[G_{\mu\nu}G^{\mu\nu}]\,. \tag{3.29}$$

So the nuclear matrix element for each heavy quarks can be evaluated via

$$\langle N(k')|\alpha_S\;\text{Tr}[G_{\mu\nu}G^{\mu\nu}]|N(k)\rangle = -\frac{8\pi}{9}\,m_N\;f^n_{T,g}\;\bar{u}_n(k')\,u_n(k)\,. \tag{3.30}$$

The coefficients $f^n_{T,q}, f^n_{T,g}$ parameterize the nuclear matrix elements of the scalar parton operators and can be found e.g. in Table II of Ref. [27]. For effective DM operators coupling to quarks like

$$\begin{aligned}\mathcal{O}_{s,q} &= \frac{m_q}{2\Lambda_s^2}s^2\bar{q}q\\ \mathcal{O}_{a,q} &= \frac{p\cdot p'}{2\Lambda_a^4}m_q\bar{q}qa^2\end{aligned} \tag{3.31}$$

this finally yields

$$\begin{aligned}\mathcal{M}_{s,q} &= \frac{m_N}{\Lambda^2}\left(f^n_{T,u}+f^n_{T,d}+f^n_{T,s}+\frac{2}{9}\,f^n_{T,g}\right)\;(2m_N)\,\xi^\dagger_{s'}\xi_s\\ \mathcal{M}_{a,q} &= \frac{p\cdot p'}{\Lambda^4}m_N\left(f^n_{T,u}+f^n_{T,d}+f^n_{T,s}+\frac{2}{9}\,f^n_{T,g}\right)(2m_N)\,\xi^\dagger_{s'}\xi_s\;.\end{aligned} \tag{3.32}$$

where we have used a non-relativistic field expansion as given in [46]. The effective suppression scale Λ is will be specified later in terms of model parameters in Chapter 5. For effective operators directly related to the gluon field strength tensor via

$$\begin{aligned}\mathcal{O}_{s,g} &= \frac{\alpha_S}{2\Lambda_s^2}s^2\,\text{Tr}[G_{\mu\nu}G^{\mu\nu}]\\ \mathcal{O}_{a,g} &= \frac{\alpha_S}{2\Lambda_a^4}(p\cdot p')\;a^2\,\text{Tr}[G_{\mu\nu}G^{\mu\nu}]\;,\end{aligned} \tag{3.33}$$

we get

$$\begin{aligned}\mathcal{M}_{s,g} &= -\frac{8\pi}{9}\frac{m_N}{\Lambda_s^2}f^n_{T,g}(2m_N)\,\xi^\dagger_{s'}\xi_s\\ \mathcal{M}_{a,g} &= -\frac{8\pi}{9}\frac{m_N p\cdot p'}{\Lambda_s^4}f^n_{T,g}(2m_N)\,\xi^\dagger_{s'}\xi_s\;.\end{aligned} \tag{3.34}$$

For the momentum-dependent matrix elements, we can use eq. 3.22 and $p\cdot p' \approx m_a^2 - m_a^2v_a^2 + \mathbf{p}\cdot\mathbf{q}$ in order to write

$$p\cdot p' = m_a^2\left(1 - v_a^2 + \frac{\mathbf{q}^2}{2m_a\mu_{aN}}\right)\;. \tag{3.35}$$

Plugging this into the matrix elements and calculating the cross section as given in eq. 3.26 yields effectively a velocity expanded cross section. Since $v_a \sim 10^{-3}$, the velocity-suppressed terms can be dropped. In Chapter 5, we will go through a set of models that describe these interactions. With the groundwork done here, we only have to replace the suppression scales by explicit parameters of our theory. Followed by squaring the matrix elements and the integration of eq. 3.26, we get expressions for the cross section that we then compare to its limits from several experiments.

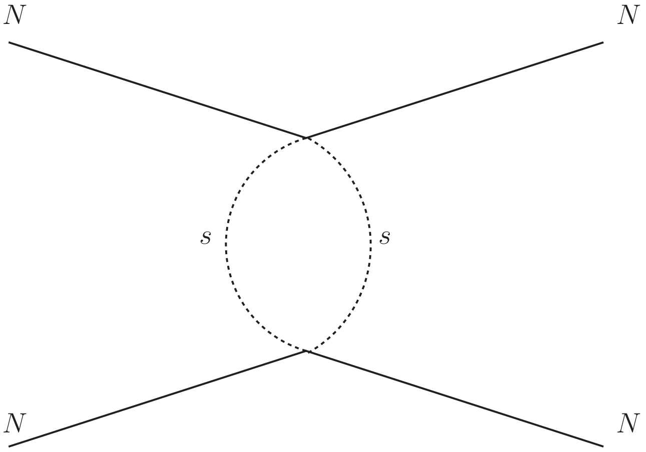

Figure 3.6: Effective nucleon-nucleon-interaction via the coupling of a scalar bilinear to a nucleon-pair as often probed by fifth force searches.

3.4 Low Energy Experiments

For low energy experiments, we will concentrate on the interaction of scalar bilinear interactions with SM particles as we will need them later in Chapter 5. We distinguish between low energy experiments that are based on fifth force searches and some that study the consequences of variations of the fundamental constants due to new scalar fields.

Fifth Force Searches: In fifth force searches, we look at the DM pair exchange between nuclei as depicted in Fig. 3.6. It is often expressed in terms of effective operators of the form

$$\mathcal{O}_s = \frac{1}{\Lambda}\bar{N}N\frac{s^2}{2}, \quad \mathcal{O}_a = \frac{1}{\Lambda^3}\bar{N}N\frac{(\partial^\mu a)^2}{2} \ . \tag{3.36}$$

These interactions are creating a potential that affects measurements of low energy observables [34]. The effects would be seen in experiments like neutron-nucleon scattering [111], Eot-Wash limits on fifth forces based on data from torsion balance experiments [112–114], fifth force experiments based on planar geometry [115, 116], and molecular spectroscopy measurements [117]. All the constraints coming from these measurements do not require the introduced scalar particle to be of DM nature in the first place.

In contrast to that, the MICROSCOPE satellite [118] tests the interactions of eq. 3.36 in the presence of a DM background field. It probes deviations in the orbits of test masses.

Variation of Fundamental Constants: If the DM halo acts like a classical background field $s(t) = s_0 \cos(m_s t)$, it induces oscillating variations in fundamental constants. Measurements that are sensitive to variations in fermion masses m_f, the fine-structure constant α and massive gauge boson masses m_V set stringent constraints on ULDM with masses $\ll$ eV. SM-like operators including m_f, α, and m_V are

$$\mathcal{L}_{\text{SM}} \supset -\sum_f m_f \bar{f} f - \frac{F_{\mu\nu}F^{\mu\nu}}{4} + \sum_V \delta_V m_V^2 V_\mu V^\mu \ , \tag{3.37}$$

with $\delta_W = 1$ and $\delta_Z = 1/2$. These constants are modified by effective interaction operators of the form

$$\mathcal{L} \supset \frac{s^2}{\Lambda_{s,f}^2} m_f \bar{f} f - \frac{s^2}{\Lambda_{s,\gamma}^2} F_{\mu\nu}F^{\mu\nu} - \frac{s^2}{\Lambda_{s,V}^2}\delta_V m_V^2 V_\mu V^\mu \ , \tag{3.38}$$

for scalar bilinears coupling to those SM operators. For pseudoscalar fields entering the operators in derivatives, i.e. $\partial^\mu a$, only the time derivative is important. We have $\partial^0 a = \partial^0(a_0 \cos(m_a t)) = -m_a a_0 \sin(m_a t) = m_a a_0 \cos(m_a + \delta')$ with some arbitrary phase δ' that we will drop. The corresponding effective Lagrangian reads

$$\mathcal{L} \supset \frac{m_a^2 a^2}{\Lambda_{a,f}^4} m_f \bar{f} f - \frac{m_a^2 a^2}{\Lambda_{a,\gamma}^4} F_{\mu\nu} F^{\mu\nu} - \frac{m_a^2 a^2}{\Lambda_{a,V}^4} \delta_V m_V^2 V_\mu V^\mu \ . \tag{3.39}$$

Wherever we treat the DM field as a classical field, we can simply translate these two sets of Lagrangians into each other via $s^2/\Lambda_{s,i}^2 \leftrightarrow m_a^2 a^2/\Lambda_{a,i}^2$. In both the scalar and pseudoscalar case, we insert the classical field solution and rewrite the quadratic (pseudo-) scalar interaction in a constant and a time-dependent part as done in Ref. [32]

$$\begin{aligned} s^2 &= s_0^2 \cos^2(m_s t) \to \frac{s_0^2}{2} \left(1 + \cos(2 m_s t)\right) \\ a^2 &= a_0^2 \cos^2(m_a t) \to \frac{a_0^2}{2} \left(1 + \cos(2 m_a t)\right) \ . \end{aligned} \tag{3.40}$$

In this form the constant term describes a fifth force while the oscillating terms lead to a variation of fundamental constants, for instance the fermion mass is

$$m_f \to m_f \left[1 + \frac{s^2}{\Lambda_{s,f}^2}\right] = m_f \left[1 + \frac{s_0^2}{2\Lambda_{s,f}^2} + \frac{s_0^2}{2\Lambda_{s,f}^2} \cos(2 m_s t)\right] \tag{3.41}$$

The variation of the fine structure constant and the weak boson masses can be derived in complete analogy and accordingly for the derivative case.

Spectroscopy searches are sensitive to time-dependent oscillations of nucleus and electron masses and the fine-structure constant. Since the frequency of these oscillations are related to the mass, $\omega = m_s c^2/\hbar$, the sensitivity of these searches peaks for a mass related to the total measurement time, and the experiment looses sensitivity below the lowest frequency for which one full oscillation can be measured and for frequencies higher than the shortest time between measurements [119]. The strongest constraint comes from measurements with rubidium and cesium at LNE-SYRTE [37,120].

Note that also BBN is affected by the variation of the fundamental constants as already discussed in Section 2.2. To quantify the effect of the oscillating DM field it is useful to relate the field to its energy density. For a non-relativistic oscillating DM field this is given by $\rho \simeq m_s^2 \langle s^2 \rangle$ and evolves according to [33]

$$\bar{\rho}_{DM} = 1.3 \cdot 10^{-6} [1 + z(t)]^3 \ \frac{\text{GeV}}{\text{cm}^3} \,, \tag{3.42}$$

with the redshift parameter $z(t)$. For a non-oscillating DM field, we have $\rho \simeq m_s^2 \langle s^2 \rangle / 2$ and

$$\bar{\rho}_{DM} = 1.3 \cdot 10^{-6} [1 + z(t_m)]^3 \ \frac{\text{GeV}}{\text{cm}^3} \,, \tag{3.43}$$

with $z(t_m)$ defined by $H(t_m) \approx m_s$. Applied to BBN constraints, we always assume that the mean DM energy density during weak freeze-out is much greater than the present-day local cold DM energy density $\langle s^2 \rangle_W \gg \langle s^2 \rangle_0$. In the case of the oscillating field, we make use of the relation $[1 + z(t_m)]/(1 + z_W) = \sqrt{t_W/t_m}$ and take [33]

$$\begin{aligned} t_W &\approx 1.1 \text{ s} \\ z_W &\approx 3.2 \cdot 10^9 \\ H(t_m) \sim 1/(2 t_m) \sim m_s &\to t_m \sim 1/(2 m_s) \end{aligned} \tag{3.44}$$

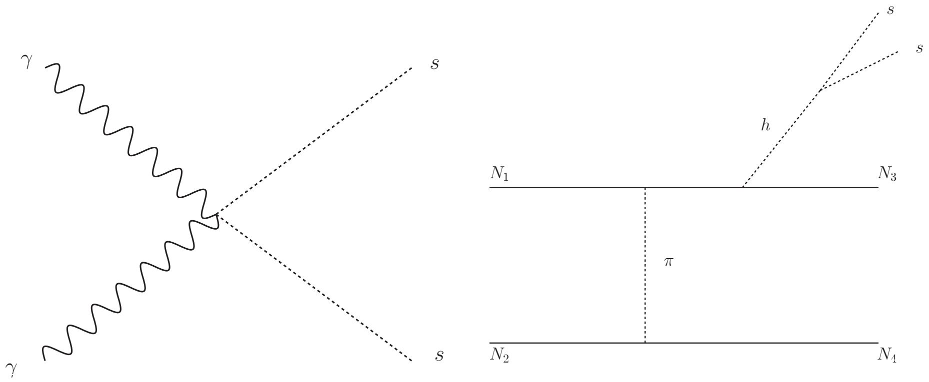

Figure 3.7: Processes for Calculations of Energy-Loss in supernovas. Photon annihilation (left) and bremsstrahlung-like scalar emission in nucleon-nucleon interactions (right).

3.5 Supernova Constraints on Light Particles

Stars can be used as a particle-physics laboratory [121] by studying the energy-loss rate implied by new low-mass particles such as ULDM particles. Any annihilation process from SM to light new particles contributes to supernova cooling. The main assumption in the corresponding calculation is that the produced particles can freely escape the supernova. This is the so-called free-streaming limit. It allows us to set an upper bound on the coupling strength of the additional processes. New particles only cause significant effects if they can compete with the cooling from neutrinos already carrying away energy directly from the interior of stars. The strongest bound comes from the SN1987A [121],

$$\varepsilon_x < 10^{19} \text{ erg g}^{-1}\text{s}^{-1} \ . \tag{3.45}$$

To set constraints, one has to evaluate the novel energy-loss rates at typical core conditions with a temperature and density of around

$$T_{\text{SN}} = 30 \text{ MeV} \qquad \text{and} \qquad \rho_{\text{core}} = 3 \cdot 10^{14} \text{ g cm}^{-3} \ . \tag{3.46}$$

This sets a constraint to the total energy-loss rate per unit mass, volume and time of novel light particles

$$\Gamma = \varepsilon_x \rho_{\text{core}} < 10^{-14} \text{ MeV}^5 \ . \tag{3.47}$$

The most prominent processes considered are photon annihilation and a bremsstrahlung-like emission. As we will focus on quadratic scalar and pseudoscalar couplings to the SM in the further course of the thesis, we shortly discuss pair emission processes as depicted in Fig. 3.7. Generally, the energy-loss rate per unit mass, volume and time due to novel particle emission is given by

$$\Gamma_{xx} = n_{\text{SM}}^2 \langle E \sigma_{ss} v \rangle \ , \tag{3.48}$$

where n_{SM} is the number density of the incident SM particle pair xx and $\langle E \sigma_{ss} v \rangle$ is the thermally averaged cross section for s-pair emission. The crucial ingredient is the cross section of the underlying process. In the case of photon annihilation, it is easy to calculate the cross section for $\gamma\gamma \to ss$ once we know how the new particle couples to the electromagnetic field strength tensor. Nevertheless, the dominant process for scalar DM production in the core is usually nucleon bremsstrahlung $NN \to NN + ss$ [122]. With an effective operator as in eq. 3.36, the energy-loss bound can be estimated as [122]

$$\Gamma_{NN} \sim \sigma_{NN} \frac{n_N^2 T^{7/2} m_N^{3/2}}{12\pi^4 \Lambda^4} < 10^{-14} \text{ MeV}^5 \ . \tag{3.49}$$

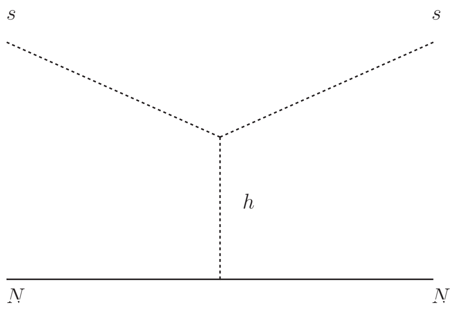

Figure 3.8: Elastic $s - N$ scattering process relevant for the trapping limit in supernova constraints. For the simplified models the Higgs has to be replaced by the new scalar mediator.

For the derivative coupling operator in eq. 3.36, we have [123]

$$\Gamma_{NN} \simeq \frac{1056\sqrt{\pi}}{(2\pi)^6}\left(3 - \frac{2\beta}{3}\right)\left(\frac{n_B^2}{2\Lambda^3}\right)^2\left(\frac{2m_N}{m_\pi}\right)^4\frac{T^{9.5}}{m_N^{4.5}} < 10^{-14}\ \mathrm{MeV}^5 \tag{3.50}$$

for the process $NN \to NNaa$ where the $\beta = 2.0938$ arises from averaging over the nucleon scattering angle, and m_π is the mass of the pion that is exchanged between the nucleons.

After being produced, new particles travel through the SN core and might start interacting with the supernova. The process considered here is elastic scattering $Ns \to Ns$ with a t-channel Higgs or scalar particle exchange. Here, we only mention the scalar s but the same procedure applies to the pseudoscalar. To estimate for which couplings light scalars start to interact with the supernova particles, we compare the radius of the supernova, $R_{\mathrm{SN}} \approx 10$ km, with the mean free path of elastic scattering as depicted in Fig 3.8,

$$\lambda = \frac{1}{n_N(r)\,\sigma_{sN\to sN}}, \quad n_N(r) = \begin{cases} \dfrac{\rho_{\mathrm{core}}}{m_p} & \text{for } r \le R_{\mathrm{SN}}\,, \\ \dfrac{\rho_{\mathrm{core}}}{m_p}\left(\dfrac{R_{\mathrm{SN}}}{r}\right)^m & \text{for } r > R_{\mathrm{SN}}\,, \end{cases} \tag{3.51}$$

and $m = 3\ ...\ 7$ depending on the profile chosen. This condition characterizes the trapping regime, i.e. the point where the new scalars start thermalizing and are trapped such that they cannot escape the supernova freely anymore. Once the scalars are trapped they create a scalar-sphere similar to the axiosphere [121, 124]. In the regime where the free-streaming limit doesn't apply anymore, the sphere still looses energy via black-body-radiation. The radius of the sphere r_0 can be determined by

$$4\pi r_0^2\,\frac{g\pi^2}{120}\,T(r_0)^4 < 10^{53}\ \mathrm{ergs}^{-1}\,, \tag{3.52}$$

with a temperature profile of $T(r) = T_{\mathrm{SN}}(R/r)^{m/3}$ [125] and $g = 1$ the number of effective degrees of freedom. It varies between

$$r_0 = 1.7\ ...\ 7.2 \cdot 10^6\ \mathrm{cm}\,, \tag{3.53}$$

depending on m. The second condition for the black-body radiation of a scalar-sphere with radius r_0 is an upper bound on the optical depth

$$\int_{r_0}^{\infty} \lambda^{-1}\mathrm{d}r \le \frac{2}{3}\ . \tag{3.54}$$

Combining the optical depth criterion with the upper bound on the luminosity of the scalar-sphere, we will set a bound on the couplings of our models discussed in Chapter 5. We call this the trapping limit. Note that the only input from the DM model side to these calculations is only the elastic scattering cross section.

4 | Hadronic Footprint of (sub-) GeV DM

This chapter is based on work in collaboration with Tilman Plehn and Peter Richardson [1]. All tables and figures as well as a significant part of the text are taken from the corresponding publication.

As described in Section 3.1, indirect searches for DM are an important way to directly probe the properties of DM in the Universe. Leading signatures are photons, or charged particles like leptons and anti-protons produced in DM annihilations in dense regions of the sky [7–10]. These photons and charged particles can be produced directly, they can be the decay products of hadrons and in the case of photons produced through radiation from any charged annihilation product. As discussed in Section 3.1, standard indirect detection searches and CMB can set strong constraints on DM annihilations. In fact for DM masses in the range $m_{\text{DM}} = 0.1 \ldots 7$ GeV the CMB provides the leading constraint on thermal DM. If s-wave annihilating DM should account for the total DM relic abundance, models are even excluded by indirect detection below $m_{\text{DM}} \lesssim 10$ GeV .

These constraints are weaker in many non-standard thermal DM scenarios. For example, asymmetric DM is an alternative production model leading to weaker CMB constraints if the DM is sufficiently asymmetric [96]. CMB constraints can be evaded if the ratio of anti-DM over DM is less than $\sim 2 \times 10^{-6}(10^{-1})$ for DM masses $m_{\text{DM}} = 1$ MeV(10 GeV). [96]. Not yet being fully asymmetric, one still gets indirect detection signals. Other modifications weakening the CMB constraints for thermal production are softer spectra from annihilation modes beyond $2 \to 2$ kinematics [126, 127], including $2 \to 3$ bremsstrahlung process [128–143]. As pointed out in Section 2.1.2, velocity-dependent cross sections can have a $x^{-1} = T/m_{\text{DM}}$ suppression in thermal processes. In addition, for DM dense regions at the sky with low expected DM velocities, any velocity-suppressed cross section would lower the signals. These models are not excluded in the sub-GeV range and depend on the modeling of the final states. Recent studies have investigated p-wave annihilations for leptonic final states [77, 97, 144]. Another interesting case is DM that can be captured into bound states through light force carries [145].

For DM annihilations directly into leptonic final states, the energy spectra for positrons, as well as for photons are rather easy to calculate, maybe with the exceptions of τ final states. A major technical problem with DM annihilation into hadrons is that its description is not available through standard Monte-Carlo tools like Pythia once the DM mass drops below around 5 GeV. The only exception is the recent Hazma [146] tool covering DM masses below 250 MeV [30]. This leaves DM annihilation to hadronic final states for masses between 250 MeV and 5 GeV essentially uncovered and yet unstudied.

GeV-scale DM annihilations to SM particles can be mediated through light scalar or vector bosons. For a new scalar mediator we would expect Yukawa-type couplings to SM quarks that roughly reflect the SM mass hierarchy. Vector mediators, instead, are generation-universal. Both scenarios are unexplored and should be investigated for hadronic final states. The advantage in the case of vector mediators coupling to quarks is that one can benefit from a large amount of data of similar processes in the SM, namely e^+e^- annihilation processes. In that case we observe a wealth of hadronic annihilation channels below the $b\bar{b}$ threshold. Guided by these hadronic SM processes, we can deduce the form of interaction that DM is expected to have in these channels. These DM annihilation channels will have distinct photon and lepton spectra, which we will focus on in this study.

In Sec. 4.1 , we review the established implementations. We show how their reliability starts to fade once we go below DM masses of 5 GeV and the tools start to extrapolate beyond their common Pythia input masses. In Sec. 4.2, we provide the first proper description of energy spectra from sub-GeV DM annihilating into hadronic final states based on Herwig with an updated fit to electron–positron data, including several new final states. Especially for the photon spectrum we observe a complete change in the shape of the spectrum when we reduce the DM mass. In addition we provide a first estimate of the impact of the input-data fit uncertainties on the output spectra. In the Appendix we provide all details about our new fit, the underlying parametrizations, the best-fit points, and the error bands.

4.1 Established Tools For Indirect Detection Searches

Energy spectra for different DM annihilation channels to SM particles can be generated by several public tools. As discussed in Section 3.1, the calculation of these energy spectra is based on Monte-Carlo simulations and are limited in DM masses. The approach used by DM tools and their back-end are summarized in Tab. **??**. In the following, we shortly describe their features

- Pppc4dmid [20] provides tabulated energy spectra for indirect detection. The $e^{\pm}$, $\bar{p}$, $\bar{d}$, γ, and $\nu_{e,\mu,\tau}$ fluxes are generated with Pythia8.135 [18] down to $m_\chi = 5$ GeV. We use the provided interpolation routine to extrapolate the results to $m_\chi = 2$ GeV.
- micrOMEGAs [21,22] uses tabulated Pythia spectra for $\gamma, e^+, \bar{p}, \nu_{e,\mu,\tau}$ and extrapolates down to $m_\chi = 2$ GeV. In the manual of version micrOMEGAs2.0 it is mentioned that the strategy for calculating spectra is analogous to that of DarkSusy and that spectra extrapolated to masses below 2 GeV should be taken with care.
- MadDM [23,24] provides two ways of calculating the energy spectra both based on Pythia [147]. The 'fast' calculation is based on the numerical tables provided by Pppc4dmid. In the 'precise' mode, events are generated with MadGraph and then passed to Pythia for showering and hadronization. In this mode it is possible to calculate the fluxes of any final states based on the UFO model implementation.
- DarkSusy [25, 26] provides tables down to 3 GeV for energy spectra of two-particle SM final states based on Pythia6.426 [148]. The tool can interpolate and extrapolate the $\gamma, e^+, \bar{p}, \bar{d}, \pi_0, \nu_{e,\mu,\tau}, \mu$ fluxes for all quark final states. In addition it includes annihilation to $\mu\mu$, $\tau\tau$, gluons, and weak bosons. DM annihilation into e^+e^- pairs appears to not be included.
- Hazma [146] is a Python toolkit to produce energy spectra in the sub-GeV range. It is based on leading order chiral perturbation theory and is valid in the non-resonance region below $m_\chi =$ 250 MeV.

From that list of public tools, it is clear that except of Hazma all are based on Pythia. In general, all multi-purpose Monte Carlo tools, such as Pythia or Herwig can calculate the energy spectra for many hard scattering processes, followed by hadronization or fragmentation and hadron decays as discussed in Section 3.1.3.

Tool	Back-end	$m_\chi^{\min}$	DM models
Pppc4dmid	Pythia8.135 tables	5 GeV	generic DM
micrOMEGAs	Pythia6.4 tables	~ 2 GeV	UFO model
MadDM	Pppc4dmid Pythia8.2 direct	5 GeV ~ 2 GeV	UFO model
DarkSusy	Pythia6.426 tables	~ 3 GeV	generic DM, SUSY

Table 4.1: Comparison of publicly available tools to generate spectra from DM annihilation [1].

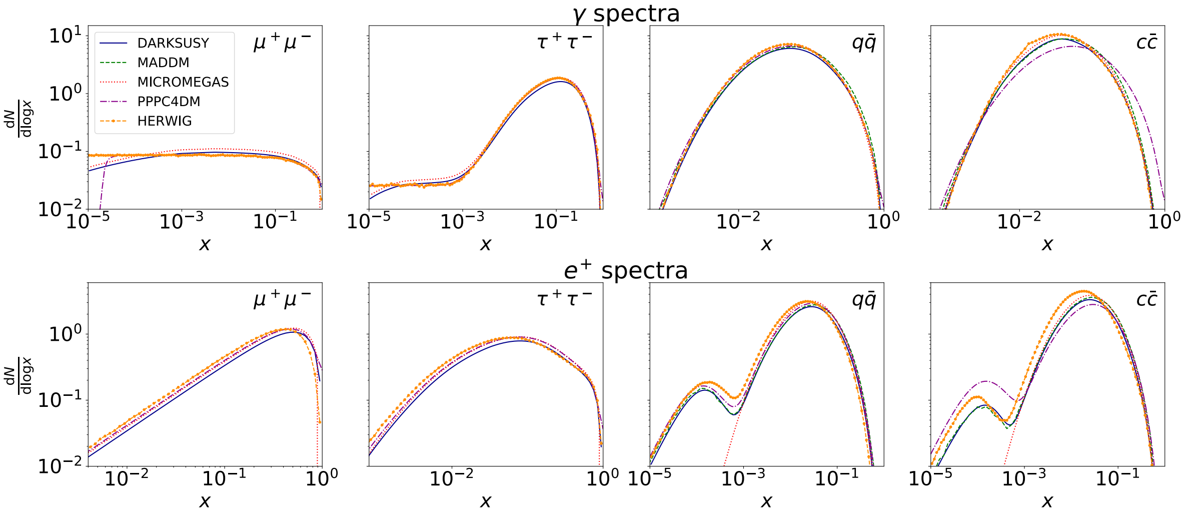

Figure 4.1: Photon and positron spectra $dN/d\log x$ with $x = E_{\text{kin}}/m_\chi$ for $m_\chi = 5$ GeV from the different hard annihilation channels [1]. We show results from DarkSusy, MadDM, micrOMEGAs, Pppc4dmid, and Herwig.

For a detailed comparison of all tools, we assume annihilation processes of the form $\chi\chi \to \mu^+\mu^-/\tau^+\tau^-/\bar{q}q$, and allow for any kinematically allowed SM quark final state. This is identical to the well-known $e^+e^- \to \mu^+\mu^-/\tau^+\tau^-/\bar{q}q$ process, at a given energy $m_{ee} = 2m_\chi$, if we switch off initial state radiation. In Fig. 4.1 we compare the corresponding Pythia-like spectra from the standard tools discussed above. We show the photon and positron spectra from DM annihilation into muon, tau, light-quark (u, d, s) and $\bar{c}c$ pairs and compare them to the standard Herwig output for $e^+e^- \to$ SM pairs. Starting with the left panels of Fig. 4.1 we see a flat photon spectrum from soft-enhanced radiation and a triangular positron spectrum from the μ^+-decay with a three-particle final state $\mu^+ \to e^+\nu_e\bar{\nu}_\mu$. The spectra for taus are characterized by its leptonic and hadronic decays. Especially for the photon spectrum, we observe a flat leptonic region from soft photon emission for low x. In hadronic decays τ leptons produce neutral and charged pions, e.g. in $\tau^- \to \pi^+\pi^0\nu_\tau$ decays, where for instance the decay $\pi^0 \to \gamma\gamma$ dominates the photon spectrum down to $x \approx 10^{-3}$. The dominant contribution to the position spectrum are the hadronic decays into charged pions accompanied by neutral pions and a tau neutrino. Positrons are produced in the subsequent decays of the charged pions into muons into electrons $\pi^+ \to \mu^+ \to e^+$. A sub-dominant contribution is coming from the leptonic β-decay $\tau^+ \to e^+$. Next, light-flavor quarks u, d, s form a range of hadrons which then decay to $\pi^0 \to 2\gamma$. The positron spectrum from these light quarks includes a soft neutron β-decay, which gives rise to the secondary maximum around $x \approx 10^{-4}$. The neutron decay has not been included in the default version of micrOMEGAs we used. Finally, moving to DM annihilation into charms we see that the photon and positron spectra are the same as for the light quarks.

In Fig. 4.2 we show the same spectra, but for a slightly lower DM mass of 2 GeV. This value is already slightly beyond where Pythia output should be used. Almost all radiation and decay patterns remain the same as for 5 GeV, but the different curves start moving apart. An interesting feature appears in the annihilation $\chi\chi \to c\bar{c}$. Here the extrapolated results from Pppc4dmid and DarkSusy still include a secondary peak corresponding to the neutron decay in the light quark channel. However, the lightest charm baryon is Λ_c has a mass of 2.29 GeV, so at $m_\chi = 2$ GeV it cannot be produced on-shell. What we see is likely an over-estimate of off-shell effects or an extrapolation error from the 5 GeV case, which illustrates the danger of ignoring the explicit warning not to use for instance Pppc4dmid or DarkSusy below their recommended mass ranges. For micrOMEGAs the spectrum is significantly softer than from the dedicated MadDM call to Pythia and from Herwig.

Altogether we find that for $m_\chi = 5$ GeV there is a completely consistent picture, where the Pythia-based results are in excellent agreement with e^+e^- results from Herwig. Going to $m_\chi = 2$ GeV leads

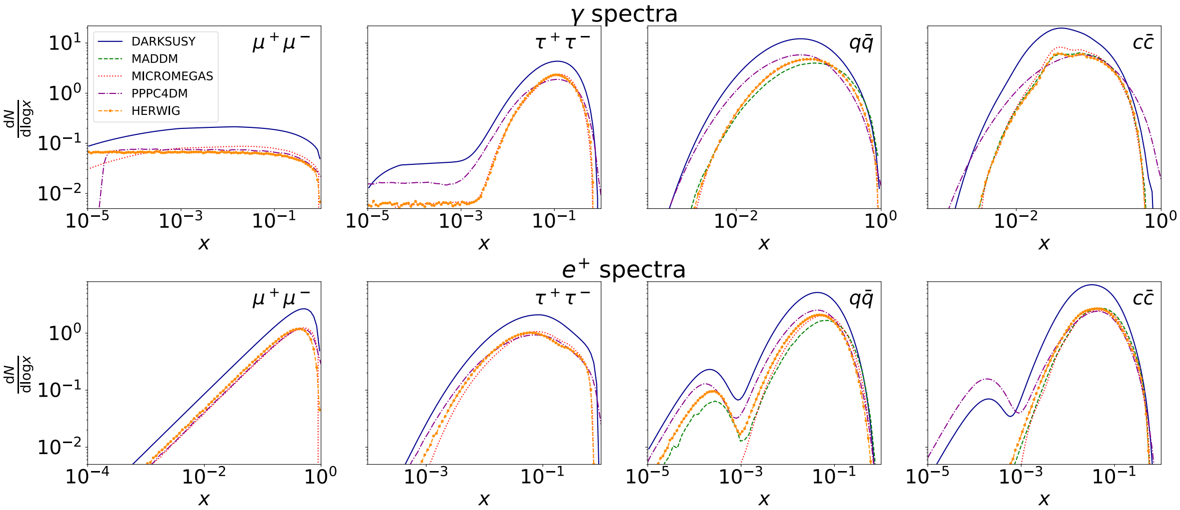

Figure 4.2: Photon and positron spectra $dN/d\log x$ with $x = E_{\text{kin}}/m_\chi$ for $m_\chi = 2$ GeV from the different hard annihilation channels [1]. We show results from DarkSusy, MadDM, micrOMEGAs, Pppc4dmid, and Herwig.

to an increased variation between the different tools and illustrates why we might not want to use the standard tools outside their recommended mass ranges.

4.2 Herwig4DM Spectra

4.2.1 Calculational Details

$e^+e^- \to$ hadrons

If we limit ourselves to DM annihilation through a vector mediator we can relate the DM annihilation process to the corresponding and measurable process

$$e^+e^- \to \text{hadrons}. \tag{4.1}$$

The e^+e^--annihilation cross section to hadrons does not behave that different from annihilations into $\mu^+\mu^-$ above 10 GeV. Both channels are mediated by neutral vector bosons. As we can see in Fig. 4.3, the only exceptions are resonance regions. At the Z-pole e^+e^- dominantly annihilates through the Z boson into kinematically favored hadrons. Down to 10 GeV energies, the ratio of annihilations to hadrons over muons $R = \sigma(e^+e^- \to \text{ hadrons}, s)/\sigma(e^+e^- \to \mu^+\mu^-, s)$ is almost flat. A couple of narrow resonances like the J/Ψ and Υ lie in the range between 3 and 10 GeV where we expect more direct annihilations to mesons with charm and bottom content. As illustrated in blue in Fig. 4.3, the most challenging region is below about 2 GeV. That region is dominated by $\rho-, \omega-$, and ϕ-meson resonances and its excited states. These measurements indicate that instead of a non-resonant photon mediator, the hadronic processes are mediated by light meson propagators. Hence, we expect the photon to mix with the vector mesons leading to an interaction structure of the form $e^+e^- \to \gamma^* \to \rho, \omega, \phi \to$ hadrons. Its matrix element has the form

$$\mathcal{M} = e\ \bar{v}_{e^+}\gamma^\mu u_{e^-}\ d^{\text{em}}_{\mu\nu}\ \langle\text{had}|J^\nu_{\text{em}}|0\rangle \tag{4.2}$$

where $d^{\text{em}}_{\mu\nu}$ is the electromagnetic photon operator, e the electric charge coupling the electron-positron pair to the photon and $J^\mu_{\text{em}} = \sum_{q=u,d,s} e_q \bar{q}\gamma^\mu q$ is the electromagnetic quark current. In order to relate the electromagnetic current to the vector meson propagators, we decompose it into its isospin components $I = 0, 1$. Starting with the isospin doublets $\Psi_q = (ud)^{\text{T}}$ and $\bar{\Psi}_q = (\bar{u}\bar{d})$, we can form

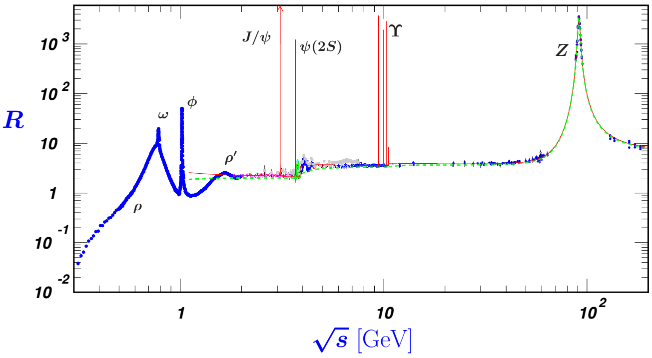

Figure 4.3: World data on the ratio of $R(s) = \sigma(e^+e^- \to \text{ hadrons}, s)/\sigma(e^+e^- \to \mu^+\mu^-, s)$ [42].

an isospin triplet by using Pauli matrices just like in every two-state spin statistic. Two of the three isospin $I = 1$ components are charged currents and can be used for processes involving for example τ's. The third component of the isospin $I = 1$ triplet $J^\mu_{I=1,3} = \frac{1}{\sqrt{2}}(\bar{u}\gamma_\mu u - \bar{d}\gamma_\mu d)$ is neutral. Combined with the isospin singlet $J^\mu_{I=0} = \frac{1}{\sqrt{2}}(\bar{u}\gamma_\mu u + \bar{u}\gamma_\mu d)$, we can rewrite the electromagnetic quark current as

$$J^\mu_{\text{em}} = \frac{1}{\sqrt{2}} J^\mu_{I=1,3} + \frac{1}{3\sqrt{2}} J^\mu_{I=0} - \frac{1}{3} J^\mu_s \,, \tag{4.3}$$

with

$$\begin{aligned} J^\mu_{I=1,3} &= \frac{\bar{u}\gamma_\mu u - \bar{d}\gamma_\mu d}{\sqrt{2}}, \\ J^\mu_{I=0} &= \frac{\bar{u}\gamma_\mu u + \bar{d}\gamma_\mu d}{\sqrt{2}}, \\ J^\mu_s &= \bar{s}\gamma_\mu s \,. \end{aligned} \tag{4.4}$$

Now we can associate the isospin $I = 1$ part with the ρ-meson and and the isospin $I = 0$ part with the ω meson. The strange quark current J^μ_s is related to the ϕ-meson. Note that it can also be counted as an isospin $I = 0$ current. So only by rewriting the electromagnetic quark current, we can decompose the process into its resonant isospin components.

Next, we relate those vector meson resonance contributions to possible final states via G-parity. G-parity is a multiplicative quantum number combining C-parity and isospin symmetry. In general, the G-parity of a particle is given by $G = (-1)^{S+L+I}$. For mesons with $L = 0$, this reduces to $G = (-1)^{S+I}$. For example, pions are pseudoscalar particles with $S = 0$ and isospin $I = 1$. Therefore, they have G-parity $G = (-1)$. Since the quantum number is multiplicative, all even numbers of pion final states have positive G-parity and all odd number of pions in the final state have negative G-parity. For the resonant vector mesons with $S = 1$ that produce these final state particles, we have $G = (-1)^{1+I}$. We see that, in order to preserve G-parity, even number of pion final states are mediated by the $I = 1$ ρ-meson and odd numbers of pions in the final state by the $I = 0$ isospin ω-meson. For the case of annihilations into 3 pions, we also include a ϕ contribution. For final states with half-integer isospins like kaons, it is possible to form $I = 0$ and $I = 1$ contributions and thus, all vector mesons are considered as intermediate particles of the process. For energies above 1 GeV, we also include excited states of ρ's and ω's. Since G-parity is not strictly a symmetry of QCD, but more a guideline for the leading effects, isospin-breaking contributions are considered in some cases. For the three lightest quarks there exists a wealth of measurements to several final states. Based in e^+e^--data we perform fits to the parameterized currents for all channels. For more details on the parameterization and the final states that are included in our calculations, we refer to Appendix A.1.

$\chi\chi \to$ hadrons

In the case of DM annihilations, the procedure is just the same. Instead of the photon propagator $d^{\text{em}}_{\mu\nu}$ coupling to electrons and quarks, we consider a new vector mediator coupling to the DM and quarks. The general matrix element for DM annihilation can be written in the form

$$\mathcal{M} = a_{\text{DM}} \bar{v}(p_1)\gamma^\nu u(p_2) d^{\text{DM}}_{\nu\mu} \langle X | J^\mu_{\text{DM}} | 0 \rangle \tag{4.5}$$

with the DM-mediator coupling a_{DM} and the vector mediator propagator $d^{\text{DM}}_{\nu\mu}$. We decompose the quark DM current $J^\mu_{\text{DM}} = \sum_{q=u,d,s} a_q \bar{q}\gamma^\mu q$ into isospin components and a separate $s\bar{s}$ contribution,

$$J^\mu_{\text{DM}} = \frac{1}{\sqrt{2}} \left((a_u - a_d) J^{I=1,3,\mu} + (a_u + a_d) J^{I=0,\mu} \right) + a_s J^{s,\mu} \tag{4.6}$$

where a_q with $q = u, d, s$ are the couplings of the vector mediator to the light quarks. The isospin currents in eq. 4.6 are just the same as in eq. 4.3. Hence, all e^+e^- annihilation processes can simply be translated to DM annihilations. Depending on values of a_u, a_d, and a_s, one or the other isospin current might vanish. As a consequence, some resonance contributions to the channels might vanish, or even more drastically, pure isospin $I = 0$ channels, for example

$$\chi\chi \to \omega\pi\pi, \eta\omega, \ldots . \tag{4.7}$$

or pure $I = 1$ channels such as

$$\chi\chi \to \pi\pi, 4\pi, \eta\pi\pi, \omega\pi, \phi\pi, \eta'\pi\pi, \ldots \tag{4.8}$$

are absent. We also choose to include the isospin breaking contribution from $\omega \to \pi^+\pi^-$ in the $I = 1$ current for simplicity. With this method we are able to study DM annihilations to hadronic final states down to the threshold of the $\pi^0\gamma$ channel which is just above the pion mass $m_{\text{DM}} \gtrsim m_\pi$.

4.2.2 Toy Model Results

As a toy model for our hadronization we assume that the observed DM density is somehow produced through thermal freeze-out, but with a light vector mediator. We assume that the DM candidate is a Majorana fermion χ, but our results apply the same way to other initial state DM particles. Since our study is based on e^+e^-- data, we have to focus on vector mediator models. A simple mediator choice starts from an additional $U(1)$ gauge symmetry, where we gauge one of the accidental global symmetries related to baryon and lepton number [149–153]. For our purpose of testing DM annihilation into light mesons, the coupling strength of the DM to the mediator can be chosen arbitrarily. We are only interested in the form of the energy spectra from hadronic final states. Crucial are only the couplings of the mediator to quarks. We choose a $B-L$-like model with universal couplings to all light quarks $a_q = 1/3$. An attractive combination is for example $B - 3L_\mu$ [154]. To avoid strong biases from an underlying model we also show results for couplings similar to the Standard Model case of photons coupling to quarks for low energies. For both cases, we assume an approximately on-shell annihilation

$$\chi\chi \to Z' \to q\bar{q} \qquad \text{with} \quad m_{Z'} \approx 2m_\chi \, . \tag{4.9}$$

In our toy models we always assume $m_{Z'} = 2m_\chi$, but changing that should only have a negligible impact on our spectra. Since the mass of the mediator determines the width of the mediator, we calculate the width in the hadronic resonance region within Herwig through its decays to all kinematically allowed hadronic final states listed in Tab. A.1 of the Appendix.

For light DM masses the relevant quarks are u, d, s. The charm quark plays a special role, because its threshold region is poorly understood. Examples for distinct photon spectra from annihilations to c and b quarks are, for example, described in [155]. All we can do for b and c quarks is to rely on the spectra included in the default version of Herwig.

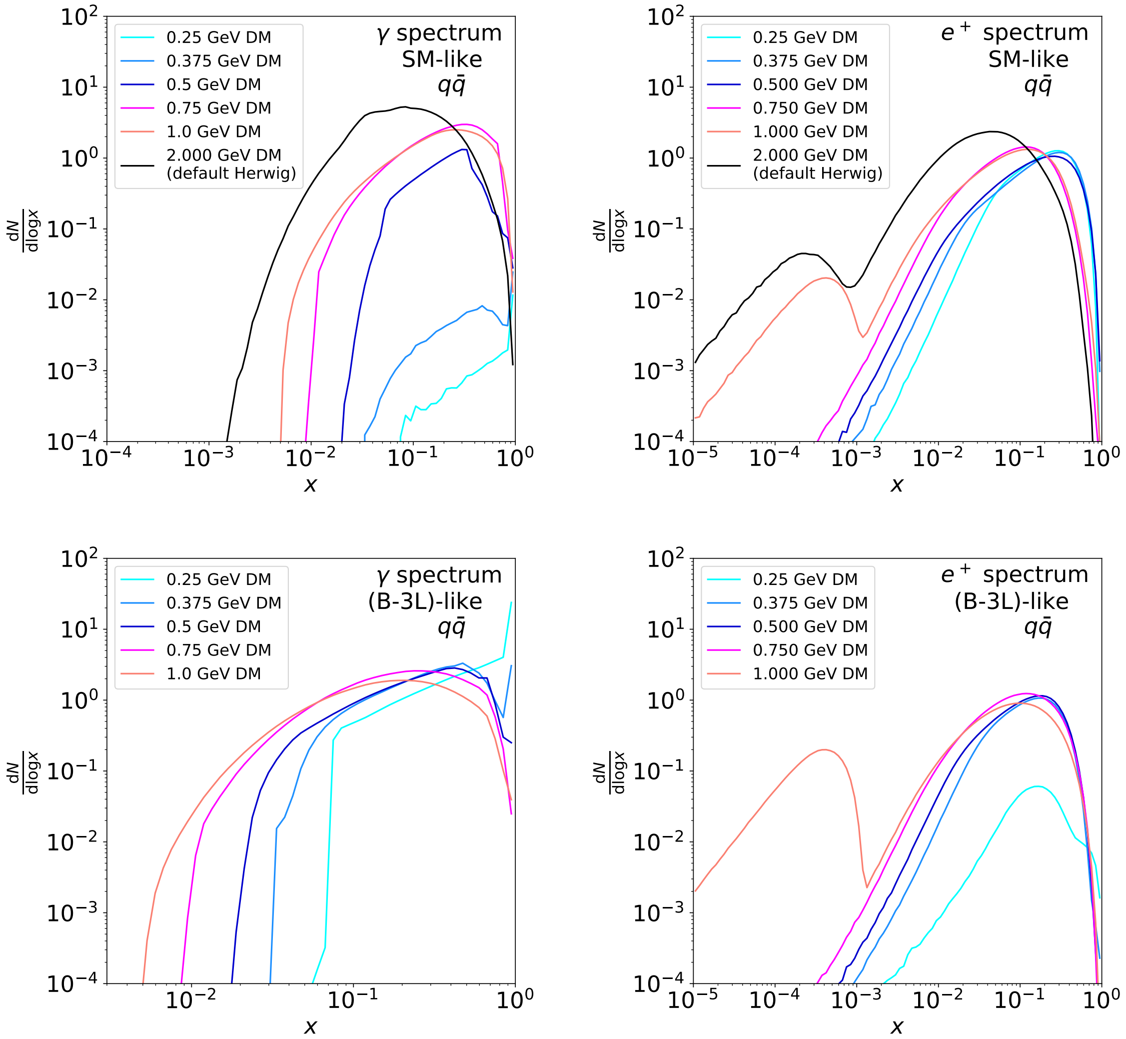

Figure 4.4: Photon and positron spectra $dN/d\log x$ with $x = E_{\rm kin}/m_\chi$ for $m_\chi = 0.25$ ... 2 GeV from u, d, s, c quarks with SM-like and $(B-3L)$-like couplings [1]. We use our modified version of HERWIG7 for all curves below 2 GeV.

Most photons and positrons in hadronic processes come from neutral and charged pion decays, respectively. These pions are either directly produced or are the end of a decay chain of all forms of hadronic states listed in Tab. A.1 in the Appendix. In a few cases, photons can also be directly produced in DM annihilation, for instance

$$\chi\chi \to \eta\gamma, \pi\gamma \ . \tag{4.10}$$

In the left panel of Fig. 4.4 we see how photon production channels drop out when we reduce the DM mass or center-of-mass energy of the non-relativistic scattering process. Whereas for $m_\chi > 1$ GeV all possible hadronic final states contribute to the round shape of the spectrum, for lower energies only photons and positrons from very specific processes give a characteristic energy spectrum.

For example for $m_\chi = 500$ MeV which corresponds to a center-of-mass energy of 1 GeV we expect two kaons from the ϕ resonance to provide most photons through consecutive decays of kaons to pions to photons. This leads to a triangular shape of the photon spectrum. If we go down to 250 MeV, the only remaining annihilation channels are

$$\chi\chi \to \pi^0\gamma, \pi\pi, 3\pi \; . \tag{4.11}$$

Of those, the photons mainly come from the $\pi^0\gamma$ final state, so one photon is produced directly with an energy around the DM mass. It leads to the distinct sharp peak around $x \approx 1$. The additional photons come from the π^0-decay and are responsible for the distribution to roughly $x \approx 10^{-1}$. The same applies for $m_\chi = 375$ MeV with an additional bump-like contribution from neutral pions in the 3π and 4π channels as well as additional photons from the dominantly neutral $\eta\gamma \to (2\gamma)\gamma, (3\pi^0)\gamma$ decay including a direct photon.

The basic shape of the positron spectrum largely depends on neutron pair production. Above the production threshold, we observe an additional peak slightly above $x \sim 10^{-4}$ resulting from positron production in the neutron β-decay. For $m_\chi < 1$ GeV, all positrons come from charged pion decays. The peak position depends on how early that charged pion decay occurs for the dominant processes at the respective center-of-mass energy. For example, for $m_\chi < 500$ MeV, charged pions are mainly produced directly in $\pi\pi, 3\pi, 4\pi$ production and hence the peak of the spectrum is shifted towards $x = 1$.

As mentioned in Sec. 4.2.1, the composition of the DM current depends on the mediator couplings to quarks a_q. In case of any $(B-3L)$-like model with $a_q = 1/3$, the isospin $I = 1$ contribution vanishes and consequently some resonance contributions as well as all channels listed in Eq.(4.8) vanish. For $m_\chi = 250$ MeV this implies that without the $\pi\pi$ channel, $\pi^0\gamma$ becomes the dominant annihilation mode. The direct photon production lifts the photon spectrum, as seen in the upper panels of Fig. 4.4. This is accompanied by a drop in the positron spectrum that only receives contributions from the subdominant 3π final state. If we choose a center-of-mass energy below the 3π threshold, positron spectra from quarks would be completely absent. For $m_\chi = 375$ MeV with an increasing 3π contribution towards the $\omega(782)$ resonance, the position spectra are lifted. For higher energies and the contribution from several channels, the $(B-3L)$-like spectra resemble the SM-like case.

4.2.3 Uncertainty Discussion

Uncertainties on the energy spectra are dominated by the uncertainties from the fits to electron-positron data discussed in the Appendix. We define ranges of model parameters to cover bands in the e^+e^--annihilation cross sections as a function of the energy and propagate those parameter ranges through the hadronic currents into the energy spectra. This means that the error on a given spectrum corresponds to the uncertainty of the dominant channel at the corresponding energy.

In the upper panels of Fig. 4.5 we see that the photon spectrum at $m_\chi = 250$ MeV inherits large uncertainties from the poorly measured dominant $\pi^0\gamma$ channel in that energy range. For $m_\chi = 375$ MeV the more precisely measured 3π channel suppresses the $\pi^0\gamma$ channel, but still leaves us with visible error bands. For even higher energies several channels contribute to the uncertainty of the photon spectrum. We observe the smallest error bands for spectra that benefit from precisely measured dominant processes, for instance peak regions such as the ϕ resonance at 1 GeV in the KK channel, the ρ resonance in the 2π decay, or generally well-measured channels such as 4π. Positron spectra with their dominant $2\pi, 3\pi, 4\pi$ channels are always well measured. The only exception is $m_\chi = 1$ GeV spectrum, especially the lower peak around $\sim 10^{-4}$, which comes from the neutron β-decay. As discussed in the Appendix, the $n\bar{n}$ channel is poorly measured and leaves us with larger uncertainties in that regime.

In $(B-3L)$-like models, we will not get any contributions from well-measured 2π and 4π final states. This means the uncertainties on the position spectrum for $m_\chi = 250$ MeV are slightly larger than in the SM-like case, see the lower panel of Fig 4.5. Nevertheless, as long as no channel drops out and another channel with larger uncertainties starts to dominate, the uncertainties in the $(B-3L)$-like case tend to be smaller. The reason is the absence of the $I = 1$ contributions and their sizable uncertainties.

In Fig. 4.5 so far, we have used the uncertainties on the individual channels bin-wise, add all contributions up and normalize by the sum of their corresponding cross-sections. For channels with large

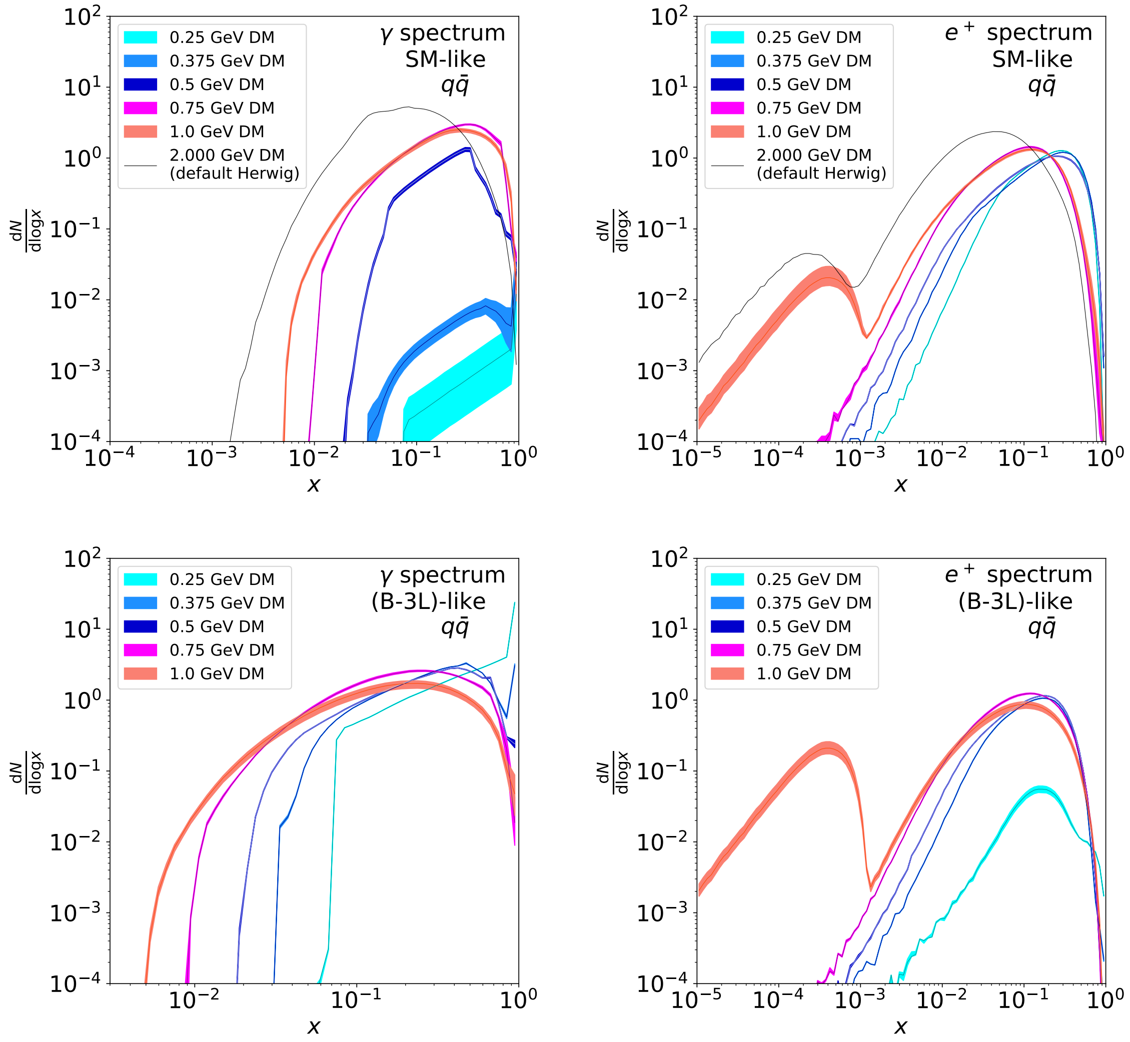

Figure 4.5: Photon and positron spectra $dN/d\log x$ with $x = E_{\text{kin}}/m_\chi$ for $m_\chi = 0.25 \ldots 2$ GeV from u, d, s, c quarks with SM-like and $(B-3L)$-like couplings with uncertainty bands allowing for perfect cancellations [1]. The 2 GeV curve and the central values correspond to Fig. 4.4.

cross-sections that are also giving the main contribution to the total amount of photons/positrons in the spectrum, the error bars can completely cancel for the normalized spectra. This way, we only get sizable uncertainty bands for spectra where one channel is dominating the shape of the spectrum, but is playing a sub-dominant role in the total cross-section. An example is the $\pi^0\gamma$ final state for the SM-like photon spectrum at $m_\chi = 250$ MeV or the lower bump in the 1 GeV positron spectrum caused by $n\bar{n}$. This assumption can be considered somewhat aggressive in a situation where we do not have full control of the full error budget. Instead, we also choose a bit more conservative approach study the uncertainties. We can maximize and minimize all spectra channel by channel and separately normalize them by the smallest and largest total cross-section possible. This way there will be no cancellation for single-channel spectra, and in Fig. 4.6 we indeed see much increased uncertainties. Obviously, the real error bands are going to be somewhere between the results shown in Fig. 4.5 and Fig. 4.6 determined by analysis details beyond the scope of this first analysis.

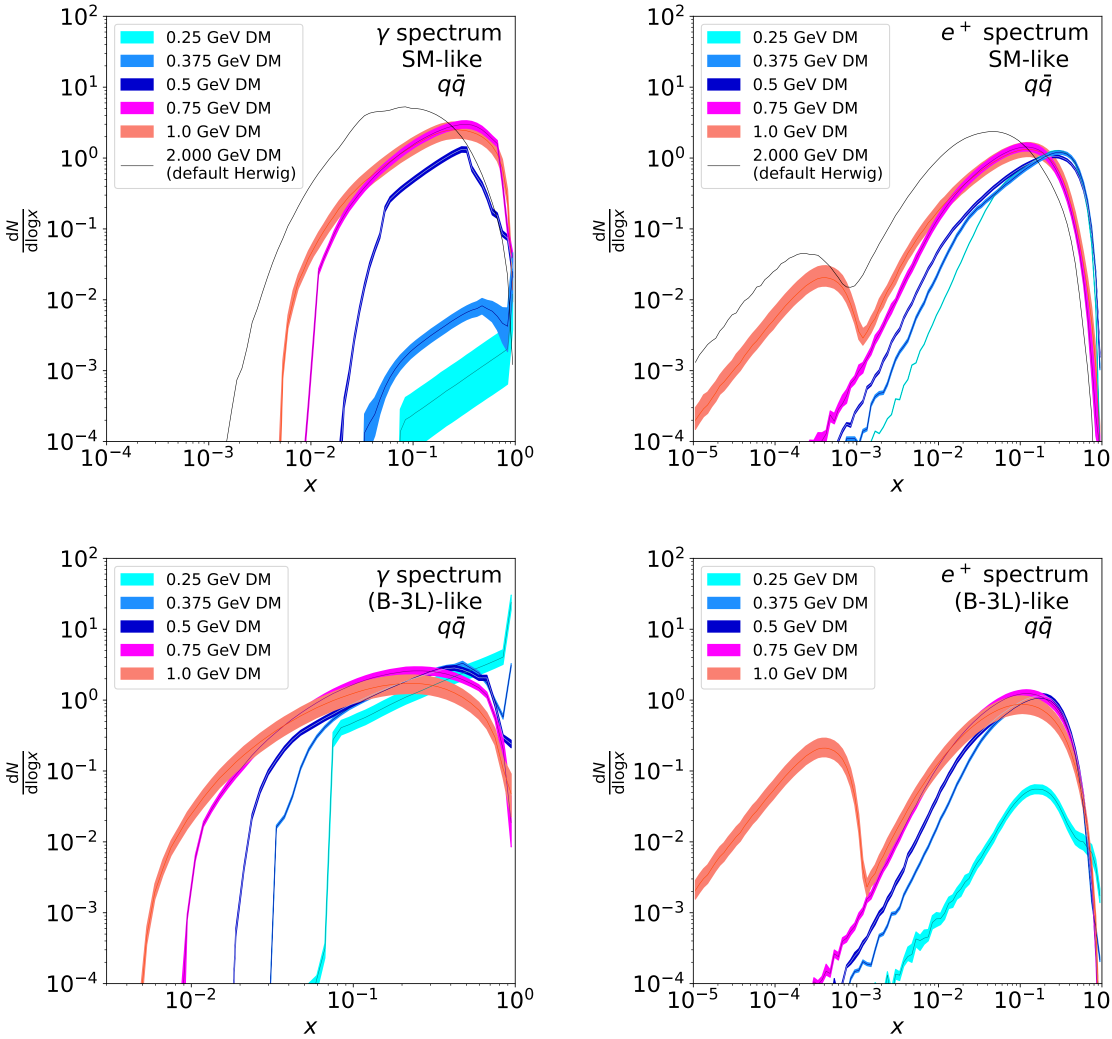

Figure 4.6: Photon and positron spectra $dN/d\log x$ with $x = E_{\text{kin}}/m_\chi$ for $m_\chi = 0.25 \ldots 2$ GeV from u, d, s, c quarks with SM-like and $(B - 3L)$-like couplings with very conservative uncertainty bands. The 2 GeV curve and the central values correspond to Fig. 4.4.

4.3 Conclusion & Outlook

We have studied the positron and photon spectra from non-relativistic DM annihilation in a DM mass range from 250 MeV to 5 GeV (with the exception of the poorly understood region near the charm threshold). With the method we have used we are even able to study DM annihilations down to the production threshold of the $\pi^0\gamma$ channel which is just above the pion mass. We consider a vector mediator with general couplings to SM fermions. For the photon spectra we see a smooth interpolation from typical hadron decay chains with their round spectra down to the pion continuum with a triangular shape. For positrons the main feature is the secondary neutron decay above threshold.

Since we are relying on an updated fit to electron-position input data to Herwig we can also propagate the uncertainties from poorly measured channels into the photon and positron spectra. Already for relatively heavy DM the positron spectrum shows sizable error bars. In the case of photons, smaller DM masses with fewer and less well measured annihilation channels are also plagued by significant error bars, eventually covering an order of magnitude for $m_\chi = 250$ MeV.

Our new implementation closes the “MeV gap” between standard Pythia-based tools such as Pppc4dmid, MicrOMEGAS, MadDM, or DarkSUSY and the comparably simple small-mass continuum regime for vector mediator DM models and should allow for a reliable study of GeV-scale DM even if it dominantly interacts with SM quarks. The code we have used to produce these results will be available in a future version Herwig7. The energy spectra for photons, positrons, neutrinos, and anti-protons will also be available in a future version of DarkSUSY.

DM annihilations to hadronic final states in the sub-GeV range, extend the current possibilities of indirect searches for DM. Vector mediator DM models with couplings to quarks complement searches that have only been considered for leptonic final states so far. With data from current sub-GeV indirect detection programs like eAstrogam and INTEGRAL, there has been the urgent need for a proper theoretical description of DM annihilation to hadrons. Based on our study, s-wave as well as p-wave processes of DM models can be constrained more detailed and more robustly in future indirect detection searches.

5 | Light Dark Matter Annihilation and Scattering in LHC Detectors

In the following, we investigate the phenomenological aspects of ULDM. For cold DM with mass m and a non-relativistic velocity of $v/c \sim 10^{-3}$, the de Broglie wavelength is given by $\lambda_{\text{dB}} = 2\pi/(mv)$. With a local number density of $n = (0.04\,\text{eV})^4/m$ the occupation number then scales like

$$n\,\lambda_{\text{dB}}^3 \approx 6.35 \cdot 10^5 \left(\frac{\text{eV}}{m}\right)^4 , \tag{5.1}$$

Below ~ 100 eV, the ULDM candidate has to be bosonic due to the Pauli Exclusion Principle. For $m \lesssim 1$ eV the occupation number is so huge that DM can be treated as a classical field [156].

In order to investigate the possibility of interactions with the SM, we describe the wave DM candidate in terms of a quantum field theory. We systematically study models of light scalar and pseudoscalar DM candidates in Sec. 5.1. The light DM is coupled to the SM either via the SM Higgs mediator or a new weak-scale mediator.

In Section 5.1, we derive bounds on our exemplary models covering cosmological and astrophysical observations, as well as collider searches, direct detection constraints and low-energy experiments. Leading constraints will come from the Helium-abundance produced at the time of BBN as discussed in Chapter 2. The derivations of supernova bounds, constraints from Higgs-to-invisible searches, direct detection bounds, and the impact of low energy experiments are based upon the discussions of Chapter 3.

In Section 5.2, we study two novel processes inspired by indirect and direct detection process topologies. First, ULDM could be produced with a large boost at the LHC and annihilate with the local DM density in ATLAS or CMS detectors. This would lead to the production of pairs of photons or electrons, in analogy to indirect detection signals. Unfortunately, the probability for these processes to happen is almost zero. Second, ULDM can be produced for instance in Higgs decays and then inelastically scatter off the detector material. These inelastic scatterings produce *displaced recoil jets* that can generally appear in the first dense layers of the LHC detectors. For ATLAS this will be the two calorimeters and for CMS it can include the silicon tracker. Unlike in standard direct detection searches, we do not probe the actual DM nature of the candidate particle with these signatures. Nevertheless, we find that this strategy is promising and different from other displaced signatures.

This chapter is based on work in collaboration with Martin Bauer, Patrick Foldenauer and Tilman Plehn [2]. All tables and figures as well as a significant parts of the text are taken from the corresponding publication.

5.1 Light Dark Matter Models and Current Constraints

A particular attractive aspect of wave DM is that the macroscopic de Broglie wave length can suppress the formation of small structures and lead to less cuspy halo profiles as opposed to cold DM [157–161]. If DM only interacts gravitationally, there is a narrow, preferred mass scale of 10^{-22} eV which suppresses kpc-sized cusps and substructures [158, 162]. For wave DM with additional *repulsive* interactions [163–165], these problems can be solved for a range of masses over many orders of magnitude [166–168].

In contrast, DM with attractive self-interactions, has a destabilizing effect and causes collapses of structures such as boson stars [169, 170].

Without specifying a particular model, we can already deduce a few characteristics of sub-eV mass DM. First of all, it has to be bosonic. Additionally, as already discussed in Section 2.2, the DM abundance can clearly not be produced thermally. Instead, the correct relic density can be explained by the misalignment mechanism [171, 172] or by the Affleck-Dine mechanism if the scalar sector has an explicitly broken global symmetry [173]. Furthermore, we can assume that DM is stable. Such light DM can only decay into photons which is largely suppressed by the DM mass. Similar to the example of decaying DM in Section 3.1, we can argue with simple dimensional arguments why this is the case. A DM scalar can couple to two powers of the QED field strength $F_{\mu\nu}$ such that its life time scales like m^3/Λ^2. Similarly, a light vector couples to three powers of the field strength, leading to a life time proportional to m^9/Λ^8. This implies that as long as the suppression scale is $\Lambda \gtrsim 10^4\,\text{GeV}(m/\text{eV})^{3/2}$ and $\Lambda \gtrsim 2.25\,\text{keV}(m/\text{eV})^{9/8}$, respectively [174], light DM does not require an additional symmetry to make it stable. This is particularly true for the QCD axion for which the mass is related to the suppression scale $m \approx 5.7 \cdot 10^{-6}\,\text{eV}(10^{12}\,\text{GeV}/\Lambda)$ [175]. Nevertheless, as soon as the DM mass is above the electron-positron threshold $m > 2m_e$, stability becomes a bad assumption.

In the following, we discuss models with a Z_2-symmetry with repulsive self-interactions and point out interesting consequences for low-energy and cosmological constraints in a class of models. This symmetry guarantees DM stability for the whole mass range and self-interactions can be repulsive. In our overview we distinguish two different classes: scalar and Goldstone-boson (axion-like) DM coupled through the Higgs portal as well as through a scalar portal with a new mediator.

5.1.1 Scalar Dark Matter

A scalar singlet s protected by a Z_2-symmetry provides a UV-complete model for light DM

$$\mathcal{L} \supset \frac{1}{2}\partial_\mu s \partial^\mu s - \frac{1}{2}m_s^2 s^2 - \frac{1}{4!}\lambda_s s^4 \,. \tag{5.2}$$

Vacuum stability requires $\lambda_s \geq 0$, which implies repulsive self-interactions. Renormalizable couplings to the SM can be established through the Higgs portal

$$\mathcal{L} \supset -\frac{1}{2}\lambda_{hs}\, s^2\, H^\dagger H \,. \tag{5.3}$$

Effective SM Higgs boson couplings to gluons and photons can be obtained from the low-energy Lagrangian

$$\mathcal{L} \supset \frac{g_{h\gamma\gamma}}{v}\; hF_{\mu\nu}F^{\mu\nu} + \frac{g_{hgg}}{v}\; h\,\text{Tr}\, G_{\mu\nu}G^{\mu\nu} \;, \tag{5.4}$$

with $g_{hgg} = \alpha_s/(12\pi)$ and $g_{h\gamma\gamma} = 47\alpha/(72\pi)$ in the consistent heavy top limit and by integrating out the W-boson at one loop [176]. Higgs-induced DM self-interactions can be large for sizable λ_{hs}, but any contribution can be absorbed by choosing appropriate values of λ_s. Scalar DM with a Higgs portal is effectively a two parameter model, and both λ_{hs} and m_s need to be independently very small to have a viable ULDM candidate.

The second representative scalar model case is the Lagrangian of Eq.(5.2) without a Higgs portal, but with a new scalar mediator ϕ and an effective coupling to gluons

$$\mathcal{L} \supset -\frac{1}{2}m_\phi^2\phi^2 - \frac{\mu_{\phi s}}{2}\phi s^2 - \frac{\alpha_s}{\Lambda_\phi}\;\phi\;\,\text{Tr}\, G_{\mu\nu}G^{\mu\nu} \,. \tag{5.5}$$

In contrast to the Higgs portal model, the mediator model introduces three additional parameters, the mediator mass m_ϕ, the dimensionful coupling strength to DM $\mu_{\phi s}$ and a coupling to gluons suppressed by the scale Λ_ϕ. In the following, we assume a weak-scale mediator with m_ϕ = 100 GeV. For both scalar models we will consider a set of low-energy and cosmological constraints.

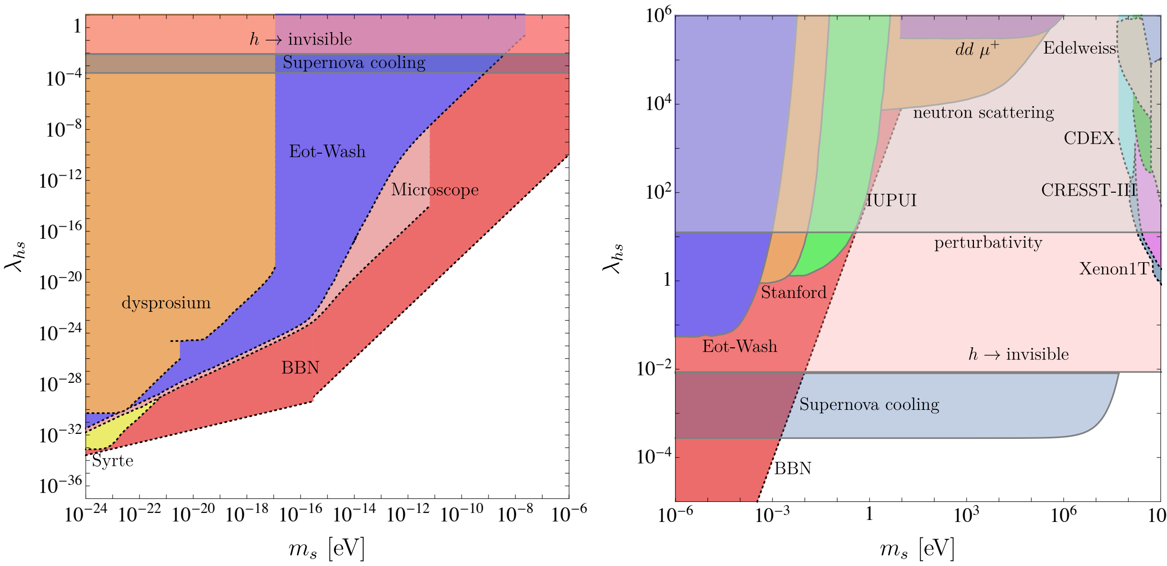

Figure 5.1: Constraints from precision experiments, cosmology, and direct detection on scalar ULDM with a Higgs portal [2]. The DM mass m_s and the portal coupling λ_{hs} are the only free parameters. Constraints which require the DM nature are shown with dotted contours.

Effective DM-nucleon interactions In eq. 3.36, we introduced a universal way of parameterizing the DM-nucleon interactions. Now that we work with fundamental models, we can resolve the structure hidden in the effective suppression scales Λ. By relating the parameters of our model to these scales, we can adapt constraints from neutron scattering, fifth-force searches, Eot-Wash experiments and molecular spectroscopy measurements in Ref [34] to our models. In our case, the mediator coupling to the gluon coupling induces an effective mediator-nucleon interaction the same way it does for the Higgs [177],

$$\mathcal{L} \supset g_{\phi NN}\ \bar{N}N\,\phi\,, \tag{5.6}$$

where the effective coupling in terms of the QCD partons is

$$g_{\phi NN} = \frac{8\pi}{11 - \frac{2}{3}n_L}\,\frac{m_N}{\Lambda_\phi}\ , \tag{5.7}$$

and n_L denotes the number of light quarks. Combined with $\mu_{\phi s}$ this coupling induces a contact interaction of two DM scalars s with two nucleons N. We can integrate out the Higgs as well as the scalar mediator by using the matching condition

$$\frac{g_{\phi NN}\,\mu_{\phi s}}{m_\phi^2}\ \bar{N}N\ \frac{s^2}{2} = \frac{1}{\Lambda}\ \bar{N}N\ \frac{s^2}{2}\,. \tag{5.8}$$

and formulate limits in both scalar DM models in terms of

$$\mathcal{L} \supset c_{sNN} s^2 \bar{N}N \tag{5.9}$$

with the dimensionful coefficients

$$\begin{aligned} c_{sNN} &= \lambda_{hs}\frac{m_N}{m_h^2}\,\frac{2n_H}{3(11-\frac{2}{3}n_L)} \qquad &&\text{(Higgs portal)}\\ c_{sNN} &= \frac{\mu_{\phi s}}{\Lambda_\phi}\,\frac{m_N}{m_\phi^2}\,\frac{8\pi}{11-\frac{2}{3}n_L} \qquad &&\text{(scalar mediator)}\ . \end{aligned} \tag{5.10}$$

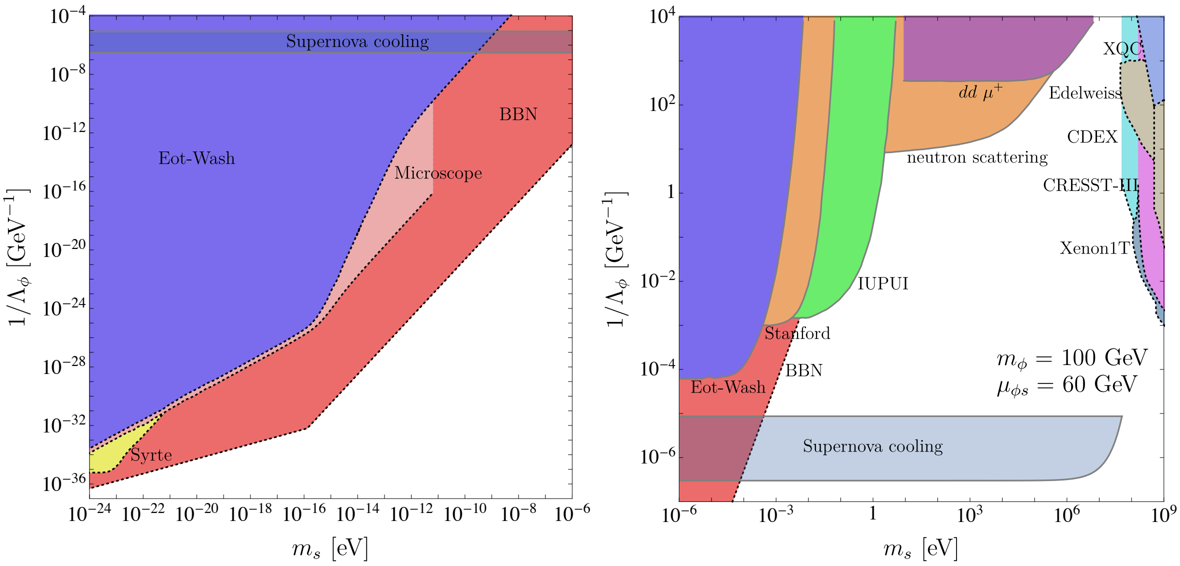

Figure 5.2: Constraints from precision experiments, cosmology, and direct detection on scalar ULDM with a scalar mediator [2]. In addition to the DM mass m_s and mediator-gluon coupling $1/\Lambda_\phi$ we fix the mediator mass to $m_\phi = 100$ GeV its coupling to the DM agent to $\mu_{\phi s} = 60$ GeV. Constraints which require the DM nature are shown with dotted contours.

Low-energy constraints These effective operators lead to a new, fifth force, mediated by the light scalar s that is independent of its DM character. The low-energy limits are shown in Fig. 5.1 as a function of the DM mass and the Higgs portal coupling. Eot-Wash limits on fifth forces based on data from torsion balance experiments [112–114] are shown in blue. For relatively high masses, shown in the right panel of Fig. 5.1, they lose sensitivity for masses $m_s \gtrsim 10^{-4}$ eV, corresponding to around 10^{-4} m, the length scale tested by the experiment. Searches for fifth forces with planar geometry are less sensitive, but can probe distances down to a few μm. The limits from experiments by the Stanford group [115] and at Indiana-Purdue (IUPUI) [116] are shown in the right panel of Fig. 5.1 in orange and green, respectively. Below the μm scale, constraints can be set by neutron-nucleon scattering [111]. The corresponding limit is shown in orange in the right panel of Fig. 5.1. Finally, molecular spectroscopy experiments are sensitive to forces below the keV scale or 10^{-10} m [34]. The strongest limit is provided by measurements with muonic molecular deuterium ions [117] shown in purple in the right panel of Fig. 5.1.

The DM halo acts like a classical background field inducing oscillating variations in fundamental constants as discussed in Section 3.4. The strongest constraint comes from measurements with rubidium and cesium at LNE-SYRTE [37, 120]. In particular, the combination of quadratic couplings to quarks and gluons effect the quark masses and QCD mass scale Λ_3 [37]. A description of how to translate these coupling to the suppression scale Λ is given in [37]. The constraints are shown in yellow in the left panel of Fig. 5.1. The MICROSCOPE satellite [118] tests this interaction in the presence of the same DM-background and probes deviations in the orbits of test masses. These limits, shown in light red in Fig. 5.1, are strong up to $m_s \approx 10^{-12}$ eV or length scales around $2 \cdot 10^5$ m, roughly corresponding to the orbit of the satellite [37]. Considering the DM-background also for Eot-Wash limits leads to stronger limits in the same mass range [37].

BBN constraints Another example for constraints coming from time-dependent DM oscillations are coming from BBN. In the same way as before the oscillations induce variations in fundamental constants such as the fine-structure constant and masses of fermions and vector bosons. From Section 2.2.1, we know that the value of the ^{4}He yield $X_{4,\text{th}} = 0.24709 \pm 0.00025$ [178] can be predicted from BBN and agrees very well with the measured value $X_{4,\text{exp}} = 0.245 \pm 0.003$ [179]. Herefrom, we follow that any variation of the standard prediction should be within the range

$$\frac{\Delta X_4}{X_4} = -0.008458 \pm 0.012183\,. \tag{5.11}$$

This is the variation that is allowed for all fundamental constants in eq. 2.51 or more specifically eq. 2.50. Just like in eq. 3.41, the variation of the fundamental constants depends on the classical field value squared. Following the effective operator analysis of Section 2.2 with the variation of fundamental constants as in Section 3.4, we get

$$\langle s^2\rangle_W \left[-\frac{0.25}{\Lambda^2_{s,\gamma}} + \frac{0.32}{\Lambda^2_{s,e}} - \frac{4.9}{(m_d - m_u)}\left(\frac{m_d}{\Lambda^2_{s,d}} - \frac{m_u}{\Lambda^2_{s,u}}\right) + \frac{3.9}{\Lambda^2_{s,W}} - \frac{5.4}{\Lambda^2_{s,Z}}\right] \simeq -0.008458 \pm 0.012183 \tag{5.12}$$

By integrating out the Higgs, we get effective couplings of the DM scalar to SM particles. This yields effective operators that we can match to the operators given in eq. 3.38 in order to obtain explicit expressions for the scales $\Lambda_{s,i}$. With the energy density relations as in Section 3.4, we derive the constraint for the Higgs portal

$$\frac{1}{m_s^2}\frac{\lambda_{\phi s}}{m_h^2}\left[-0.25(2g_{h\gamma\gamma}) - 3.79\right] \simeq (-2.6 \pm 3.7)\cdot 10^{-20}\ \text{eV}^{-4}\,, \tag{5.13}$$

for $m_s \gg 10^{-16}$ eV and

$$\frac{1}{m_s^2}\left(\frac{m_s}{3\cdot 10^{-16}\ \text{eV}}\right)^{3/2}\frac{\lambda_{hs}}{m_h^2}\left[-0.25(2g_{h\gamma\gamma}) - 3.79\right] \simeq (-1.3 \pm 1.8)\cdot 10^{-20}\ \text{eV}^{-4}\,, \tag{5.14}$$

for $m_s \ll 10^{-16}$ eV.

For the scalar mediator the operators in Eq.(5.5) lead to a universal correction to the nucleon masses induced by the coupling to gluons, whereas corrections to other fundamental constants are strongly suppressed. With the variation as in eq. 2.52, the constraint can therefore be expressed as

$$\frac{1}{m_s^2}\frac{4\pi}{9}\frac{\mu_{\phi s}}{\Lambda_\phi}\frac{1}{m_\phi^2} \simeq (4.2 \pm 6.2)\cdot 10^{-21}\,\text{eV}^{-4}\,, \tag{5.15}$$

for $m_s \gg 10^{-16}$ eV and

$$\frac{1}{m_s^2}\left(\frac{m_s}{3\cdot 10^{-16}\ \text{eV}}\right)^{3/2}\frac{4\pi}{9}\frac{\mu_{\phi s}}{\Lambda_\phi}\frac{1}{m_\phi^2} \simeq (2.1 \pm 3.1)\cdot 10^{-21}\,\text{eV}^{-4}\,, \tag{5.16}$$

for $m_s \ll 10^{-16}$ eV. In Fig. 5.1 we see that for $m_s \lesssim 10^{-3}$ eV the observed ^{4}He abundance set during BBN is indeed the most stringent constraint. The results for a scalar mediator displayed in Fig. 5.2 show a similar situation for a fixed mediator mass $m_\phi = 100$ GeV and coupling $\mu_{\phi s} = 60$ GeV.

Supernova constraints For masses below the supernova core temperature of $2m_s < T_{\text{SN}} \approx 30$ MeV, scalar DM pairs can be radiated off in nuclei interactions inside the supernova core. In the so called free streaming limit they are assumed to leave the star freely and provide a new source of cooling in addition to neutrinos [121]. With the SN limit of the observation of SN1987A introduced in eq. 3.47 and the estimate in eq. 3.49, we can put a limit on the total energy-loss rate per unit mass, volume and time. The dominant process for scalar DM production in the core is nucleon bremsstrahlung $NN \to NN + ss$ [122]. With the prescription of relating the effective scale Λ of the DM-nucleon interaction to our model parameters in eq. 5.10, this translates into

$$\begin{aligned} &\lambda_{hs} < 2.75\cdot 10^{-4} && \text{(Higgs portal)}\,,\\ &\frac{\mu_{\phi s}}{\Lambda_\phi} < 1.8\cdot 10^{-5}\left(\frac{m_\phi}{100\,\text{GeV}}\right)^2 && \text{(scalar mediator)} \end{aligned} \tag{5.17}$$

for the Higgs portal and the scalar mediator.

For large couplings, the free-streaming limit breaks down as soon as the mean free path becomes smaller than the supernova radius $\lambda \leq R_{\text{SN}}$. The light scalar particle thermalizes and is trapped in the supernova. Building up a scalarsphere it radiates energy through black-body radiation. As elaborated in Section 3.5, the only model input to the trapping limit is the elastic DM-nucleon scattering cross section. It is approximately given by

$$\sigma_{sN\to sN} \simeq \frac{1}{4\pi} c_{sNN}^2 \,, \qquad \text{assuming} \quad m_s, E_s \ll m_N \,, \tag{5.18}$$

with c_{sNN} as in eq. 5.10. We obtain the constraints

$$\begin{aligned} \lambda_{hs} &< 8.1 \cdot 10^{-3} && \text{(Higgs portal)} \,, \\ \frac{\mu_{\phi s}}{\Lambda_\phi} &< 5.2 \cdot 10^{-4} \left(\frac{m_\phi}{100\,\text{GeV}} \right)^2 && \text{(scalar mediator)} \,. \end{aligned} \tag{5.19}$$

The effect of these constraints on our model parameters is shown in Figs. 5.1 and 5.2. We note that for DM masses close to the core temperature, $m_s \lesssim T_{\text{SN}}$, we have to include a Boltzmann factor $\exp(-2\,m_s/T_{\text{SN}})$ into the energy loss rate to model the temperature dependence [6]. For masses above $m_s > 10^{-3}$ eV the BBN constraints vanish and supernova cooling yields the leading constraints, independent of the couplings and for DM masses up to $m_s \sim 50$ MeV.

Invisible Higgs decays Among all possible ways to search for DM at colliders discussed in Section 3.2, the only constraining one is the largely model-independent bound coming from searches for invisible Higgs decays. For setting limits on DM masses, we take the ATLAS value of eq. 3.20. A future high-luminosity run of the LHC (HL-LHC) could improve this limit by an order of magnitude $\text{BR}(h \to \text{inv}) \lesssim 2\%$ [103]. For the Higgs portal the partial decay rate of the Higgs to two scalars is given by

$$\Gamma(h \to ss) = \frac{\lambda_{hs}^2}{8\pi} \frac{v^2}{m_h} \sqrt{1 - \frac{4m_s^2}{m_h^2}} \,. \tag{5.20}$$

With $m_s \ll m_h/2$, this provides an essentially m_s-independent limit on the portal coupling of light DM of

$$\begin{aligned} \lambda_{hs} &< 8.7 \cdot 10^{-3} && \text{(current)} \,, \\ \lambda_{hs} &< 2.1 \cdot 10^{-3} && \text{(HL-LHC)} \,. \end{aligned} \tag{5.21}$$

This constraint is absent in the case of the scalar mediator portal. In Fig. 5.1 we see this limit right above the supernova limit.

Direct detection Finally, direct detection experiments based on heavy noble gases have a recoil threshold of ~ 1 keV, which translates, according to eq. 3.23, into a sensitivity to DM masses of $m \gtrsim 1...10$ GeV. Cryogenic calorimeter experiments can lower the nuclear threshold to ~ 100 eV, providing sensitivity down to DM masses of $m \gtrsim 100$ MeV. A similar threshold has been obtained by the space based X-ray Quantum Calorimetry Experiment (XQC) which is sensitive to strongly interacting DM in this mass range [180]. The form of the cross section for the scalar models can easily be determined based on the preparatory work of Section 3.3. With effective quark and gluon operators of the form

$$\begin{aligned} \mathcal{L} &\supset \frac{\lambda_{hs}\, m_q}{2\, m_h^2}\, s^2\, \bar{q} q && \text{(Higgs portal)} \\ \mathcal{L} &\supset \frac{\alpha_s\, \mu_{\phi s}}{2\Lambda_\phi\, m_\phi^2}\, s^2 \;\, \text{Tr}\, G_{\mu\nu} G^{\mu\nu} && \text{(scalar mediator)} \,. \end{aligned} \tag{5.22}$$

we get the DM-nucleon elastic scattering cross sections

$$\begin{aligned}\sigma_{sN\to sN} &= \frac{1}{\pi}\left(\frac{\mu_{sN}\,\lambda_{hs}\,m_N}{2\,m_s\,m_h^2}\right)^2\left(f^n_{T,u}+f^n_{T,d}+f^n_{T,s}+\frac{2}{9}\,f^n_{T,g}\right)^2 && \text{(Higgs portal)}\\ \sigma_{sN\to sN} &= \frac{16\pi}{81}\left(\frac{\mu_{sN}\,m_N\,\mu_{\phi s}}{\Lambda_\phi\,m_s\,m_\phi^2}\right)^2(f^n_{T,g})^2 && \text{(scalar mediator)}\,. \end{aligned} \tag{5.23}$$

We use the results from [35, 181] to set constraints on the parameters of the Higgs portal as shown in Fig. 5.1. For DM masses of $m_s \gtrsim 100$ MeV we see the leading constraints from Xenon1T [182] (dark grey), CRESST-III [183] (pink), CDEX [184] (cyan), Edelweiss [185] (pale brown) and XQC [180] (pale blue). In Fig. 5.2 we show the corresponding limits for a scalar mediator.

5.1.2 Pseudoscalar Dark Matter

Unlike scalar DM, pseudoscalar or axion-like (ALP) DM [186] is described by a non-renormalizable Lagrangian

$$\begin{aligned}\mathcal{L}\supset&\frac{1}{2}\partial_\mu a\partial^\mu a-\frac{m_a^2}{2}a^2+\frac{\partial_\mu a}{f}\sum_i\frac{c_i}{2}\,\bar\psi_i\gamma_\mu\gamma_5\psi_i\\ &+c_G\frac{g_s^2}{16\pi^2}\frac{a}{f}\,\mathrm{Tr}[G_{\mu\nu}\widetilde{G}^{\mu\nu}]+c_W\frac{g^2}{16\pi^2}\frac{a}{f}\,\mathrm{Tr}[W_{\mu\nu}\widetilde{W}^{\mu\nu}]+c_B\frac{g'^2}{16\pi^2}\frac{a}{f}\,B_{\mu\nu}\widetilde{B}^{\mu\nu}\,.\end{aligned} \tag{5.24}$$

All pseudoscalar couplings are suppressed by at least one power of the mass scale f. To understand the role of f and compute the couplings to the Higgs sector we consider the UV-complete theory with a complex scalar breaking a global symmetry

$$S=\frac{s+f}{\sqrt{2}}\,e^{ia/f}\,. \tag{5.25}$$

In this section the scalar mode s is heavy. Its mass is set by f, while the mass of the pseudoscalar a is proportional to some explicit breaking of the shift symmetry parameterized by μ, such that $m_a=\mu^2/f$. A conserved Z_2-symmetry $S\to -S$ forbids all dimension-5 operators. Dimension-6 operators are introduced by the renormalizable Higgs portal and the kinetic term of the full theory

$$\mathcal{L}\supset\frac{1}{2}\partial_\mu S\partial^\mu S^\dagger+\mu_s^2S^\dagger S-\lambda_s(S^\dagger S)^2-\frac{1}{2}\lambda_{hs}\,S^\dagger S\,H^\dagger H\,. \tag{5.26}$$

They give a scalar mass $m_s=\sqrt{2\lambda_s}f$ and lead to an effective, derivative Higgs portal suppressed by $1/f^2$ [187],

$$\mathcal{L}\supset\frac{2\lambda_{hs}}{m_s^2}\,\partial_\mu a\partial^\mu a\,H^\dagger H\,. \tag{5.27}$$

The derivative Higgs-portal can also be induced by a coupling between the complex scalar and the SM through the effective operator

$$\mathcal{L}\supset\frac{(\partial_\mu S)(\partial^\mu S)^\dagger}{\Lambda_{ha}^2}H^\dagger H=\frac{\partial_\mu a\,\partial^\mu a}{2\Lambda_{ha}^2}H^\dagger H=\frac{\partial_\mu a\,\partial^\mu a}{4\Lambda_{ha}^2}(v^2+2v\,h+h^2)\,, \tag{5.28}$$

where we introduce a specific suppression $1/\Lambda_{ha}$ and, in the last step, insert the Higgs field. In principle, there can be a hierarchy of scales $f\gg\Lambda_{ha}$ and we parameterize effects through the derivative Higgs portal by Λ_{ha} from now on. We also note that this operator will be generated from the Higgs portal. Alternatively, we can write it as

$$\frac{\partial_\mu a\,\partial^\mu a}{2\Lambda_{ha}^2}H^\dagger H=-\frac{m_a^2a^2}{4\Lambda_{ha}^2}(v+h)^2-\frac{a\partial_\mu a}{2\Lambda_{ha}^2}(v\,\partial^\mu h+h\partial^\mu h)\,, \tag{5.29}$$

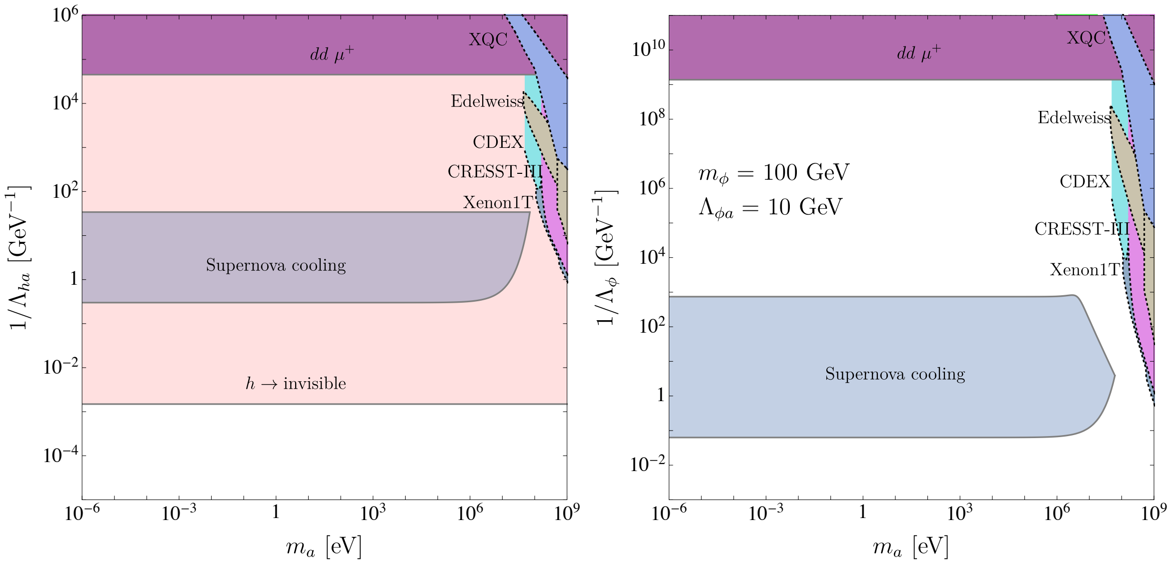

Figure 5.3: Constraints from precision experiments, cosmology, and direct detector on pseudoscalar or axion-like ULDM with a Higgs mediator (left) and a scalar mediator (right) [2]. For the latter we again fix the mediator mass to $m_\phi = 100$ GeV its coupling to the DM agent to $\Lambda_{\phi a} = 10$ GeV. Constraints which require the DM nature are shown with dotted contours.

where the second term gives rise to a momentum-dependent scalar coupling to ALP pairs.

As a simple generalization of the Higgs mediator model we again consider a model with a new scalar mediator ϕ. It is defined by the operators

$$\mathcal{L} \supset -\frac{1}{2} m_\phi^2 \phi^2 - \frac{\partial_\mu a\, \partial^\mu a}{2\Lambda_{\phi a}} \phi - \frac{\alpha_s}{\Lambda_\phi}\ \phi\ \operatorname{Tr} G_{\mu\nu} G^{\mu\nu}\ . \tag{5.30}$$

The coupling to gluons is described by the same parameter Λ_ϕ as in the scalar case of Eq.(5.5). However, unlike in the scalar case this new scale is supplemented with the new physics scale of the pseudoscalar $\Lambda_{\phi a}$. Such a scalar portal operator in a Z_2-protected symmetry is not very exotic. It has for example been considered to generate a fractional contribution to the effective number of degrees of freedom [187]. More recently, the derivative Higgs portal has been considered in the context of missing energy signals at the LHC in [188].

Effective DM-nucleon interactions In the same way as for the scalar case, we can derive effective DM-nucleon interactions. The operators given in Eq.(5.28) and (5.30) induce couplings between ALPs and nuclei,

$$\mathcal{L} \supset c_{aNN}\ \partial_\mu a\, \partial^\mu a\ \bar{N} N\ . \tag{5.31}$$

with the dimensionful coefficients

$$\begin{aligned} c_{aNN} &= \frac{1}{\Lambda_{ha}^2} \frac{m_N}{m_h^2} \frac{2 n_H}{3(11 - \frac{2}{3} n_L)} \qquad \text{(Higgs portal)} \\ c_{aNN} &= \frac{m_N}{\Lambda_{\phi a} \Lambda_\phi m_\phi^2} \frac{8\pi}{11 - \frac{2}{3} n_L} \qquad \text{(scalar mediator)}\ . \end{aligned} \tag{5.32}$$

Low-energy constraints Constraints from low-energy precision experiments can therefore be discussed in analogy with the bounds on the couplings in Eq.(5.10). In contrast to the case of the operators in Eq.(5.24), all ALP interactions mediated by Eq.(5.27) are momentum suppressed due to its derivative nature. This generalizes to theories with more than one derivative. The sensitivity of low-energy observables is therefore strongly suppressed with respect to the case of an ALP with linear interactions *and* in contrast to the scalar without a shift symmetry discussed in Sec. 5.1.1. For a more detailed discussion of this we refer to Appendix A.2.1. The potential for the long-range force induced by the exchange of at least two ALPs with shift-symmetry, Eq.(5.31), is suppressed by $1/r^7$ [34], which suppresses the sensitivity from experiments sensitive to effects at large scales. In Fig. 5.3 we show the constraints adapted from Ref. [34] both for the Higgs mediator and a new scalar mediator. The bounds from Eot-wash experiments and MICROSCOPE are not relevant for the parameter space shown in Fig. 5.3 and constraints from neutron scattering and molecular spectroscopy provide the dominant low-energy constraints.

BBN constraints Constraints on pseudoscalar DM from BBN are further suppressed by the derivative coupling. As shown in Section 3.4, an additional factor of m_a^2 enters the effective Lagrangians that vary the fundamental constants through the time derivative of the classical field with $a(t) = a_0 \cos(m_a t)$. As a result the DM mass dependence in Eq.(5.15) is canceling for the derivative model. The constraints now read

$$\begin{aligned} \frac{1}{2\Lambda_{ha}^2 m_h^2}\left(\frac{0.25 c_{h\gamma\gamma}}{4\pi} + 3.79\right) &\simeq (2.6 \pm 3.7)\cdot 10^{-20}\ \text{eV}^{-4} \quad \text{(Higgs portal)} \\ \frac{4\pi}{9\Lambda_\phi \Lambda_{\phi a} m_\phi^2} &\simeq (4.2 \pm 6.2)\cdot 10^{-19}\ \text{eV}^{-4} \quad \text{(scalar mediator)} \end{aligned} \tag{5.33}$$

for $m_s \gg 10^{-16}$ eV. For masses below $m_a \ll 10^{-16}$ eV, we get

$$\frac{1}{\Lambda_{ha}^2 m_h^2}\left(\frac{m_a}{3\times 10^{-16}\ \text{eV}}\right)^{3/2}\left[\frac{0.25 g_{h\gamma\gamma}}{4\pi} + 3.79\right] \simeq (1.3 \pm 1.8)\times 10^{-20}\ \text{eV}^{-4} \tag{5.34}$$

In any case, we see in Fig. 5.3 that the derivative interaction weakens the BBN bounds to the point that they do not even appear in the plot.

Supernova constraints Similarly, constraints from supernova cooling are strongly suppressed, because the derivatives induce additional temperature suppression in the nuclear bremsstrahlung rate. For derivative models the energy loss rate is given by eq. 3.50. For setting the free-streaming limit, we just have to make the replacement

$$\frac{1}{2\Lambda^3} \to c_{aNN}\ . \tag{5.35}$$

in order to find that couplings in the range

$$\begin{aligned} &\frac{34.1}{\text{GeV}} > \frac{1}{\Lambda_{ha}} > \frac{0.3}{\text{GeV}} && \text{(Higgs portal)}\,, \\ &\frac{740}{\text{GeV}} > \frac{1}{\Lambda_\phi}\frac{10\,\text{GeV}}{\Lambda_{\phi a}}\left(\frac{100\,\text{GeV}}{m_\phi}\right)^2 > \frac{0.063}{\text{GeV}} && \text{(scalar mediator)}\,, \end{aligned} \tag{5.36}$$

are excluded by supernova cooling constraints.

Invisible Higgs decays These relatively model-independent constraints work the same way as for the scalar case. With the partial width

$$\Gamma(h \to aa) = \frac{v^2 m_h^3}{128\pi\Lambda_{ha}^4}\left(1 - \frac{2m_a^2}{m_h^2}\right)^2 \sqrt{1 - \frac{4m_a^2}{m_h^2}} \approx \frac{v^2 m_h^3}{128\pi\Lambda_{ha}^4}\,, \tag{5.37}$$

the limits on invisible Higgs decays translate into

$$\Lambda_{ha} \gtrsim 672\ \text{GeV}\,, \tag{5.38}$$

for the current ATLAS bound and $\Lambda_{ha} \gtrsim 1.37$ TeV for the projected bound from the HL-LHC. This reach is clearly limited and an observation would not yield any information on the DM character of a new light particle. Nevertheless, in the left panel of Fig. 5.3 we see that the invisible Higgs decays give the leading constraint on the model.

Direct detection Finally, we again contrast the pseudoscalar model predictions with the limits set by different direct detection experiments. Analogous to the scalar case, we derive effective interactions term of the form

$$\begin{aligned} \mathcal{L} &\supset \frac{p \cdot p'}{2\, m_h^2\, \Lambda_{ha}^2}\, m_q \bar{q} q\, a^2 && \text{(Higgs portal)} \\ \mathcal{L} &\supset -\frac{\alpha_S\ p \cdot p'}{2\Lambda_{\phi a}\, \Lambda_\phi\, m_\phi^2}\ a^2\ \mathrm{Tr}[G_{\mu\nu} G^{\mu\nu}] && \text{(scalar mediator)} \end{aligned} \tag{5.39}$$

to obtain the elastic scattering cross sections via eq. 3.26

$$\begin{aligned} \sigma_{aN \to aN} &\approx \frac{\mu_{aN}^2\, m_a^2\, m_N^2}{4\pi\, \Lambda_{ah}^4\, m_h^4} \left(f_{T,u}^n + f_{T,d}^n + f_{T,s}^n + \frac{2}{9}\, f_{T,g}^n \right)^2 && \text{(Higgs portal)} \\ \sigma_{aN \to aN} &\approx \frac{16\pi}{81}\, \frac{\mu_{aN}^2\, m_a^2\, m_N^2}{\Lambda_{ah}^2\, \Lambda_\phi^2\, m_h^4}\ \left(f_{T,g}^n \right)^2 && \text{(scalar mediator)}\ . \end{aligned} \tag{5.40}$$

For the Higgs and scalar mediators we see in Fig. 5.3 that the different experiments systematically probe their respective model parameter space for DM masses exceeding $m_a \sim 50$ MeV. Because of the momentum dependence of (5.31), scattering from the nuclei is suppressed by the DM velocity and bounds from direct detection are considerably weaker compared to scalar DM. The limits from CRESST [189], XQC [180], Xenon1T [182], CRESST-III [183], CDEX [184] Edelweiss [185] and XQC [180] are shown with the same color coding as in Fig. 5.2. The constraints seem more important in comparison to the supernova bounds, because the temperature suppression in the latter is more effective than the velocity suppression in ALP-nucleus scattering.

5.2 LHC Signatures of Light Dark Matter

The strongest constraint on light new particles that can be set by the LHC relies on invisible Higgs decays. However, this signature is largely model-independent and would not link the new particle to DM. To test the nature of DM at the LHC one could for instance search for interactions of two light scalar particles where one is produced in LHC processes and the other scalar comes from the local DM background of our galaxy. Alternatively, a light scalar produced in Higgs decays can scatter with the detector, a DIS-like process which corresponds to direct detection. In the following we will look at both scenarios.

5.2.1 Dark Matter Annihilation

If the observed relic density is given by very light scalars with a Z_2-symmetry, its number density in the local halo is expected to be huge. For that reason, we could study the case of a particle which we produce at the LHC and annihilates with the DM background $\langle s \rangle$ like

$$\langle s \rangle s \to \gamma\gamma\ , \tag{5.41}$$

as shown in Fig. 5.4. For example we can assume that pairs of scalars s are produced at high momentum in Higgs decays and then traverse the dense DM background. In analogy to fixed target experiments, we can estimate the number of photon pairs produced from a beam of N_s scalars s with initial energy E_s at a distance l from the production point as [190–192]

$$\frac{d^2 N_{\gamma\gamma}}{dE_s\, dl} = N_s\, I_s(E_0, E_s, l)\ \frac{dP_{\text{conv}}}{dl}\ , \tag{5.42}$$

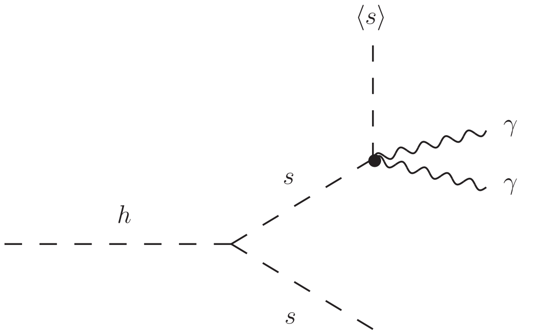

Figure 5.4: Appearing pair of boosted photons from DM-background scattering. The produced DM scalars originate from a Higgs decay and share the Higgs rest mass between them.

where I_s denotes the energy distribution function of the scalars s. In our case, the number of produced scalars can be calculated as $N_s = N_h\ \mathrm{BR}(h \to ss)$. We assume that the scalar annihilates once it hits the DM background and does not interact in any other way. Therefore, we can set $I_s(E_s, E_0, l) = \delta(E_s - E_0)$. This assumption is justified since we do not expect, for example, scalar self-interactions for a DM candidate because of structure formation arguments.

Finally, we are interested in the number of DM-to-photon conversions taking place in the fiducial detector volume. As the scalars move through the DM gas, the differential probability of a single scalar to annihilate with a DM background particle into two photons within a spatial slice dl is given by

$$\frac{dP_{\mathrm{conv}}(l)}{dl} = \frac{e^{-l/\lambda}}{\lambda}\,, \tag{5.43}$$

with the mean free path

$$\lambda = \frac{1}{n_{\mathrm{DM}}\ \sigma_{\langle s\rangle s\to\gamma\gamma}}\,, \tag{5.44}$$

and the local DM number density

$$n_{\mathrm{DM}} = \frac{\rho_{\mathrm{DM}}}{m_s} \approx \frac{10^{-41}}{m_s}\ \mathrm{GeV}^4\,. \tag{5.45}$$

Integrating Eq.(5.42) along a detector with size L_{det} at a distance L_0 away from the interaction point gives us

$$\begin{aligned} N_{\gamma\gamma} &= N_s \int_0^{m_h/2} dE_s\ \delta(E_s - m_h/2) \int_{L_0}^{L_0+L_{\mathrm{det}}} dl' \frac{e^{-l/\lambda}}{\lambda} \\ &= N_h\ \mathrm{BR}(h \to ss)\ e^{-L_0/\lambda}\left(1 - e^{-L_{\mathrm{det}}/\lambda}\right), \end{aligned} \tag{5.46}$$

With the effective Higgs couplings defined in Eq.(5.4), the corresponding differential cross section is

$$\frac{d\sigma_{\langle s\rangle s\to\gamma\gamma}}{dt} = \frac{1}{2\pi}\,\frac{\lambda_{hs}^2\, g_{h\gamma\gamma}^2}{(s - m_h^2)^2}\,. \tag{5.47}$$

As for all fixed target experiments, the center-of-mass energy is much lower than the momentum of the incoming DM particle hitting the DM target, in our case $s = m_s m_h$. With the integration bounds of Ref. [178] this leads to the typical scaling of the total rate

$$\sigma_{\langle s\rangle s\to\gamma\gamma} \approx \frac{\lambda_{hs}^2 g_{h\gamma\gamma}^2}{4\pi}\,\frac{m_s}{m_h^3}\,. \tag{5.48}$$

Inserting the maximum allowed value from Higgs to invisible searches for the Higgs portal coupling, $\lambda_{hs} = 8.7 \cdot 10^{-3}$, we arrive at a mean free path of

$$\lambda = \frac{4\pi}{\lambda_{hs}^2 g_{h\gamma\gamma}^2} \frac{m_h^3}{\rho_{\text{DM}}} \gtrsim 10^{43} \text{ m} \,. \tag{5.49}$$

The crucial observation is that a light DM mass cancels between the cross section and the particle density. Hence, the mean free path for light DM particle ($m_s \ll m_h$) due to scattering at the DM background is universally bigger than the size of the observable Universe, $l_{\text{univ}} \approx 30\,\text{Gpc} \approx 10^{27}$ m, by a factor of 10^{16}. Hence, the process is unobservable in our Universe.

For slightly larger DM masses we can briefly look at the competing annihilation channel

$$\langle s \rangle s \to \bar{f} f \,. \tag{5.50}$$

The threshold condition

$$\hat{s} \approx m_h m_s = 4 m_f^2 \quad \Leftrightarrow \quad m_s = \frac{4 m_f}{m_h} \,, \tag{5.51}$$

gives us the numerical values

channel $\bar{f}f$	e^+e^-	$\mu^+\mu^-$	$\bar{b}b$
m_s	8.4 eV	360 keV	0.56 GeV

,

and the cross section is given by

$$\sigma_{\langle s \rangle s \to \bar{f} f} = \frac{\lambda_{hs}^2}{8\pi} \frac{m_f^2}{m_h^4} \left(1 - \frac{4 m_f^2}{m_s m_h} \right) \,, \tag{5.52}$$

where we again use $s = m_s m_h$ and assume $m_s \ll m_h$. For electrons and $m_s \sim 10$ eV the relic number density will become very small and the mean free path will still be $\lambda \approx 10^{39}$ m, and the process hence unobservable.

To summarize, the mean free path of a DM particle in the DM background field with our local DM density can be written as

$$\lambda = 8.5\,\text{m} \left(\frac{m_s}{10^{-22}\text{eV}} \right) \left(\frac{10^{-6} \text{ GeV}^{-2}}{\sigma_{\langle s \rangle s \to \text{sth.}}} \right) \,. \tag{5.53}$$

The first term implies that the DM abundance increases with decreasing DM mass, and the mean free path decreases. The second term says that higher cross sections also shorten the mean free path. Applied to fuzzy DM with $m_s \sim 10^{-22}$ eV annihilating to $\gamma\gamma$, the first term becomes $\mathcal{O}(1)$ but due to the m_s/m_h^3 suppression in the cross section, we cannot even come close to the 10^{-6} GeV^{-2} $\sim \mathcal{O}(1)$ nb of the numerator. For annihilations into e^+e^- the cross section is larger but still suppressed by m_e^2/m_h^4, i.e. nowhere close to 10^{-6} GeV^{-2}. In either case, we face a large Higgs mass suppression coming from the Higgs propagator in the annihilation process. The only way out of this is to introduce a new scale that compensates or replaces at least some suppression factors. Replacing the light scalar with a pseudoscalar does not help, either. Instead, it adds a momentum suppression relative to the Higgs mass which further reduces the rate.

5.2.2 Dark Matter Scattering

The second LHC process we explore is the production of a light scalar that scatters with the detector material as depicted in Fig. 5.5. If the scalar is sufficiently light it will be highly energetic and can break up the nucleus in deep inelastic scattering. This time, the scalar does not scatter with the DM background. In this case, the characteristic signature of a spontaneously appearing hadronic jet in the

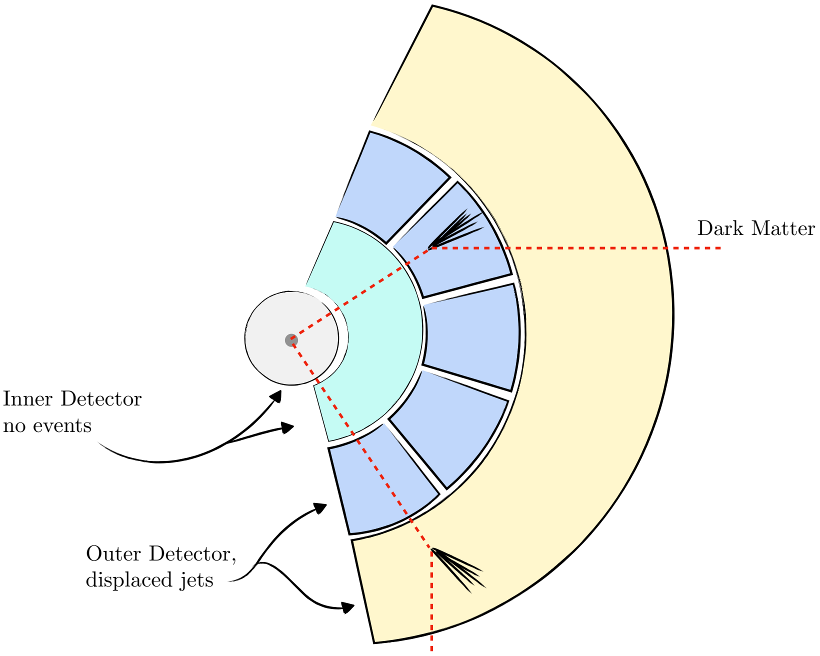

Figure 5.5: Illustration of the displaced recoil jet signature [2].

dense calorimeter material would not confirm the DM nature of the light new scalar. As before, we consider the mean free path,

$$\lambda = \frac{1}{n_{\text{det}}\ \sigma_{\text{DIS}}} , \tag{5.54}$$

of a light scalar s, this time moving through the detector material with the number density n_{det}. σ_{DIS} is the deep inelastic scattering cross section of the process. As an example we consider the electromagnetic (ECAL) and hadronic calorimeter (HCAL) of ATLAS. Both are sampling detectors using lead and iron as absorber materials [193]. As DIS takes place at the level of nucleons rather than the full nuclei we are interested in the nucleon density per unit target material. The effective nucleon density for a material X can be computed as,

$$n_X = N_A\ \rho_X\ \frac{A_X}{m_X^{\text{mol}}} , \tag{5.55}$$

where N_A denotes Avogadro's number, A_X the mass number, ρ_X the density, and m_X^{mol} the molar mass of the material X. In the central region of the detector the ECAL has a radial extension of $L_{\text{E}} = 0.6$ m and the HCAL of $L_{\text{H}} = 2$ m. The inner tracking detector is a gas detector and hence can be neglected due to its low number density.

For each of the two detector materials we can compute the partonic cross section for the process

$$sN \to sg + X , \tag{5.56}$$

as shown in Fig. 5.6. We start with the kinematics of our process before we compute the hard matrix element. The Feynman diagram for the process is shown in Fig. 5.6. We first define the incoming and outgoing scalar momenta as

$$\begin{aligned} p_{s,i} &= (E_{s,i}, \mathbf{p}_{s,i}) \quad \text{(incoming)} \\ p_{s,i} &= (E_{s,i}, \mathbf{p}_{s,i}) \quad \text{(outgoing)} . \end{aligned} \tag{5.57}$$

The nucleon momentum at rest is given by

$$P = (M, 0, 0, 0) \tag{5.58}$$

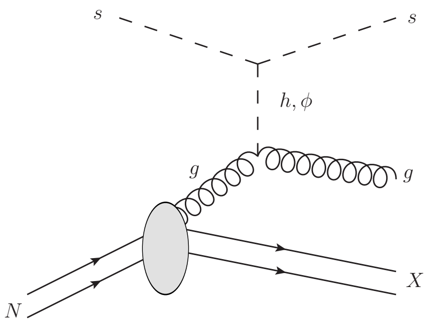

Figure 5.6: Deep inelastic scattering of a light scalar s off a nucleon [2].

with the nucleon mass M. Therewith, we can define the momentum transfer of the scalar to the nucleon system as $q = (p_{s,f} - p_{s,i}) = (\nu, \mathbf{p}_{s,f} - \mathbf{p}_{s,f})$ where we defined the energy loss of the scalar as $\nu = E_{s,f} - E_{s,i}$. Furthermore, we introduce the scaling variables

$$x = -\frac{q^2}{2P\cdot q} = \frac{Q^2}{2M\nu} \qquad \text{and} \qquad y = \frac{P\cdot q}{P\cdot p_{s,i}} = \frac{\nu}{E_{s,i}}\,, \tag{5.59}$$

where $Q^2 = -q^2$.

The nucleon scattering cross section can now be expressed as the incoherent sum of partonic cross sections weighted by their respective parton distribution function,

$$\frac{d\sigma_{\text{DIS}}}{dx\,dy} = \sum_j \frac{d\hat{\sigma}_{\text{DIS}}}{dx\,dy}\; f_j(x, Q^2)\,. \tag{5.60}$$

As long as we only consider DM particles dominantly coupling to gluons, the incoherent sum in Eq.(5.60) reduces to a weighting of the partonic cross section with the gluon PDF. To study DIS in the material of the LHC detectors we need to take into account nuclear effects by using the nuclear rather than proton PDF sets. Therefore, we perform all our calculations with the `nCTEQ15` nuclear PDF set [194] via the `ManeParse` package [195]. As a cross check we compare the results with those using the MMHT proton densities [196]. For instance in case of a scalar mediator we find about 40% more events predicted by the appropriate proton PDF sets. With the numerically calculated interaction rate σ_{DIS}, we can compute the probability that a single particle s scatters in a detector of length L_{det} as

$$P_{\text{DIS}} = 1 - e^{-\sum L/\lambda}\,. \tag{5.61}$$

Scalar Higgs portal For all models, we assume that the produced light particle carries half of the on-shell produced mediator energy. In case of the scalar Higgs portal we approximately get $E_s \approx m_h/2$. Instead of a usual DIS process in high energy physics, the nucleus N in our case it at rest. Therefore, the center-of-mass energy of the scalar–nucleus scattering is given by $s = 2E_s\,M \approx m_h M$. This yields the differential cross section for the hard scattering process in the Higgs portal model

$$\frac{d^2\hat{\sigma}_{\text{DIS}}}{dx\,dy} = \frac{\lambda_{hs}^2 g_{hgg}^2}{4\pi\,\hat{s}}\;\frac{Q^4}{(Q^2 + m_h^2)^2}\,, \tag{5.62}$$

where $\hat{s} = xs = 2ME_s\,x$. The partonic cross section has to be convoluted with the gluon density in the heavy nucleus as in eq. 5.60 and integrated over the full phase space. In the case of the scalar Higgs portal the full DM DIS cross section on lead and iron evaluate numerically to

$$\sigma_{\text{Fe}} = 5.3\cdot 10^{-9}\,\text{fb} \qquad \text{and} \qquad \sigma_{\text{Pb}} = 5.5\cdot 10^{-9}\,\text{fb}\,. \tag{5.63}$$

The total scattering probability of a particle moving radially outwards is then given by

$$P_{\text{DIS}} = 1 - e^{-L_{\text{E}}\, n_{\text{Pb}}\, \sigma_{\text{Pb}}} e^{-L_{\text{H}}\, n_{\text{Fe}}\, \sigma_{\text{Fe}}} \approx 7.5 \cdot 10^{-21} \,. \tag{5.64}$$

Next, we can combine this scattering probability with the Higgs production rate at the LHC. The expected number of DM DIS events for the maximum allowed branching ratio by supernova cooling constraints, $\lambda_{hs} \approx 2.75 \cdot 10^{-4}$ of eq. 5.17, and invisible Higgs decay in eq. 5.21 is then given by

$$N_{\text{DIS}} = \mathcal{L}_{\text{HL}}\, \sigma_h\, \text{BR}_{h\to ss}\, P_{\text{DIS}} \approx 4.1 \cdot 10^{-16} \,. \tag{5.65}$$

Inserting the Higgs production rate at $\sqrt{s} = 14$ TeV of around $\sigma_h \approx 60$ pb [197] and the total integrated luminosity expected in the high-luminosity run of the LHC (HL-LHC) of $\mathcal{L}_{\text{HL}} \approx 3\ \text{ab}^{-1}$, we find that this process is hopeless to observe in the renormalizable Higgs portal model.

Scalar with new mediator A more flexible alternative to the renormalizable Higgs portal is a new scalar mediator ϕ with an effective coupling to gluons. Before we study the DIS signature at the LHC we note that such a mediator can decay back into a pair of gluons or produce a pair of DM particles,

$$\begin{aligned} \Gamma_{\phi\to gg} &= \frac{2\,\alpha_s^2}{\pi}\frac{m_\phi^3}{\Lambda_\phi^2} \,, \\ \Gamma_{\phi\to ss} &= \frac{1}{32\pi}\frac{\mu_{\phi s}^2}{m_\phi}\sqrt{1 - 4\frac{m_s^2}{m_\phi^2}} \,. \end{aligned} \tag{5.66}$$

This means that the coupling to gluons will always lead to a di-jet resonance $\phi \to gg$. As discussed in Section 3.2, mediator searches are one way to study these interactions.

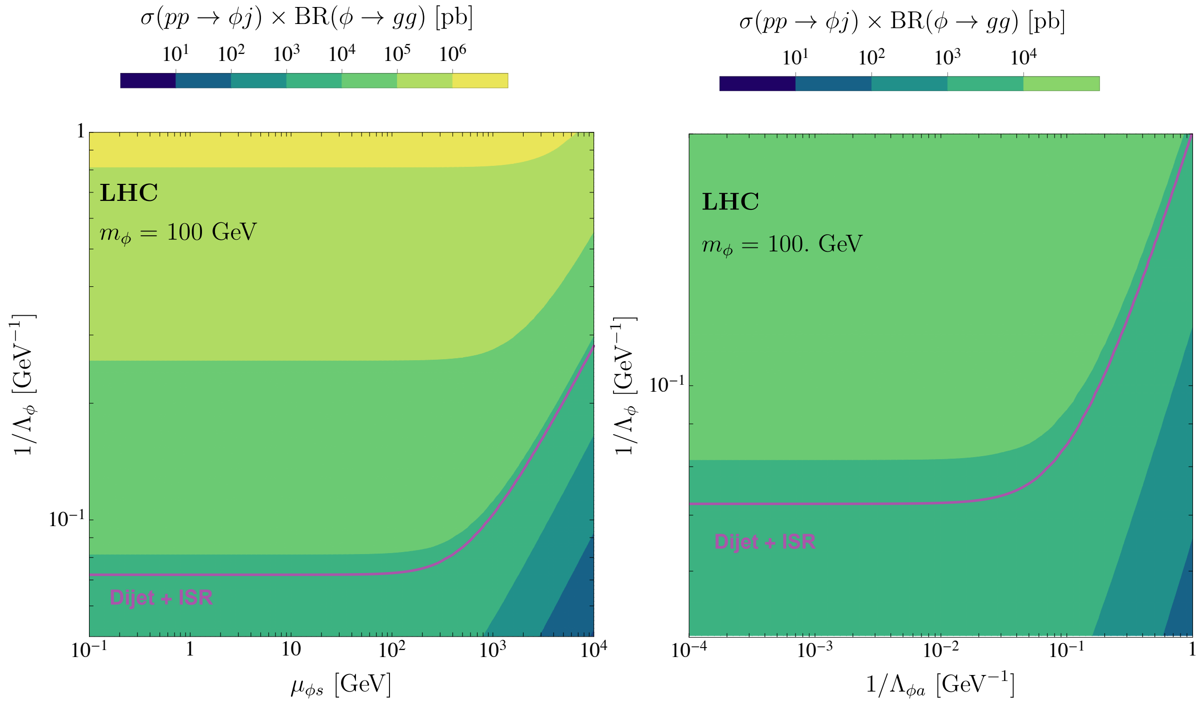

Figure 5.7: Cross section times branching ratio for the process $pp \to (\phi \to gg) + j$ for $m_\phi = 100$ GeV for the scalar (left) and pseudoscalar (right) model with a scalar mediator [2]. The purple contour shows the CMS cross section limit of Ref. [198].

We briefly report on the rough order of existing constraints although the limits from narrow resonance searches cannot be simply translated to our model with a potentially wide mediator. Among all collider constraints discussed in Section 3.2, mediator searches are expected to be the most relevant study for our model. In the low-mass regime of $50 - 300$ GeV, vector resonance searches $Z' \to \bar{q}q$ in di-jet events with an additional jet from ISR have been considered by CMS [198, 199]. In this search, the highly boosted di-jet system is reconstructed as a single large jet. This jet has to recoil back to back against a hard ISR jet, with one of the jets satisfying $p_T > 500$ GeV. We reinterpret this analysis for our mediator model by simply generating the $(\phi \to gg) + j$ signal and cutting with $p_T > 500$ GeV on the scalar. The relevant signal events $pp \to \phi + j$ are generated with `MadGraph5_aMC@NLO` [200]. The corresponding cross section times branching ratio is shown in Fig. 5.7. The purple contour represents the CMS cross section limit for a 100 GeV. Such a boosted jet analysis should be more stable for a broadening resonance than for instance a trigger-level resonance search. We quote the CMS limits as the most optimistic estimate accepting that an actual analysis for our model will not be as good as the narrow-width Z' search.

Just as in the Higgs portal case, the DM scalars s can undergo DIS in the detector material. We can again calculate the partonic DIS cross section

$$\frac{d^2\hat{\sigma}_{\text{DIS}}}{dx\,dy} = \frac{\alpha_s^2}{4\pi\,\hat{s}} \left(\frac{\mu_{\phi s}}{\Lambda_\phi}\right)^2 \frac{Q^4}{(Q^2+m_\phi^2)^2} \, . \tag{5.67}$$

To compute the total number of expected DIS events we simulate DM production, $pp \to \phi \to ss$ for a large range of mediator couplings to gluons $(1/\Lambda_\phi)$ and couplings to the DM scalar $(\mu_{\phi s})$ as shown in the left panel of Fig. 5.8. In our Monte Carlo study we analyze the p_T- spectra of the produced DM particles s and confirm that in the regime of a narrow mediator, $\Gamma_\phi/m_\phi \lesssim 10\%$, the averaged DM energy is $\langle E_s\rangle \approx 39$ GeV, with the bulk of the particles having $E_s = m_\phi/2 = 50$ GeV. For simplicity,

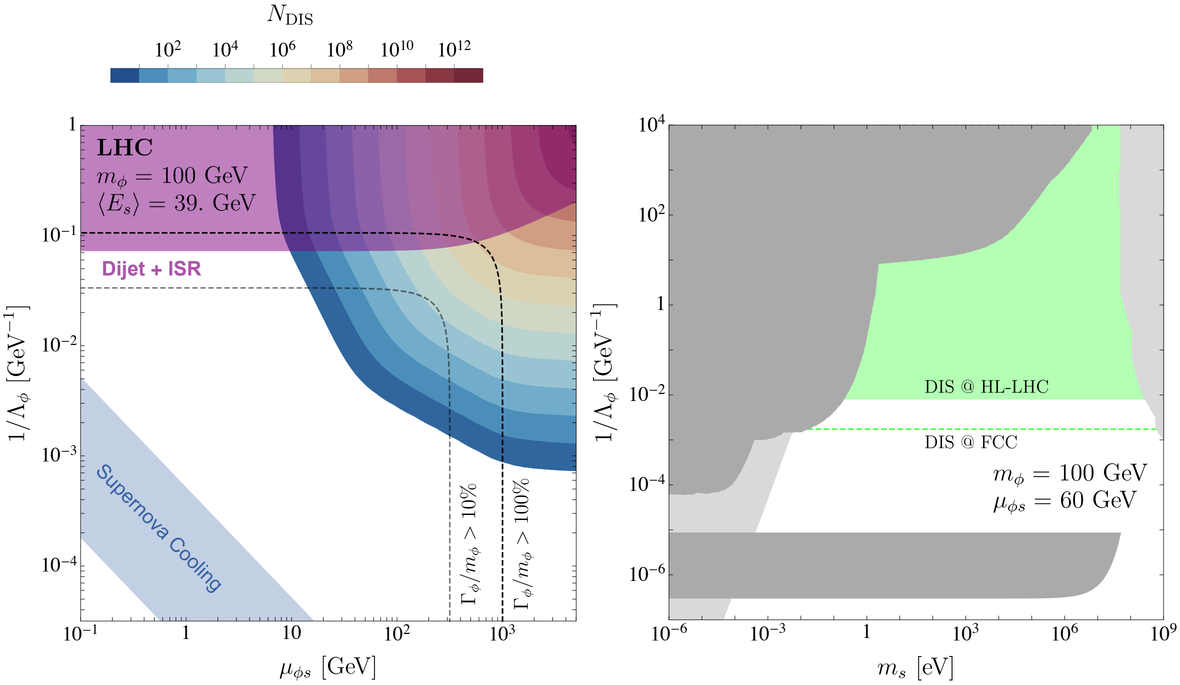

Figure 5.8: Left: number of expected DIS events in the plane of DM-mediator coupling $\mu_{\phi S}$ versus mediator-gluon coupling Λ_ϕ for $m_\phi = 100$ GeV [2]. The blue band represents the constraint from Supernova cooling, the purple area is the bound on low-mass di-jet resonances [198], and the dashed lines indicate fixed ratios $\mu_{\phi S}/\Lambda_\phi$. Right: comparison of the projected DIS reach with the low-energy constraints in terms of Λ_ϕ for fixed $\mu_{\phi s}$ [2]. Constraints which require the DM nature are shown in light grey.

we assume this average energy over all displayed parameter space in order to compute the number of DIS events. This can be considered a conservative estimate since in the case of a broader resonance the produced DM particles become more energetic on average. Thus that would enhance the DIS cross section. In a more comprehensive study the scattering cross section should be convoluted with the DM energy spectrum. However, this is beyond the scope of this sensitivity study. Similarly, we assume that the displaced recoil jet signature is essentially background-free. At the LHC this statement is never strictly true, because for instance detector failures or support structures can of course generate displaced objects. Moreover, if a highly energetic jet were to consist only of long-lived neutral hadrons it could generate such a recoil, but such a strong suppression of all charged hadronic activity is rather unlikely.

To sum up, in order to pass the LHC triggers we can rely on the standard mono-jets trigger requiring missing transverse momentum around 100 GeV. The SM-background can be reduced by using displaced recoil jets. Nevertheless, there might be additional handles on the trigger, so we will quote projected limits without the trigger requirements. We have checked that a for a momentum-independent scalar coupling the trigger catches at least 10% of the signal rate and weakens the projected limits in the coupling $1/\Lambda_\phi$ by at most a factor three.

In the right panel of Fig. 5.8 we contrast the projected reach of the DIS process with the low-energy and other limits from Fig. 5.2. We see that the DIS probe is complementary to all other constraints and fills the gap for DM masses between 1 eV and 100 MeV over two orders of magnitude in the gluon coupling $1/\Lambda_\phi$. The projected FCC sensitivity corresponds to a collider energy of 100 TeV and a luminosity of $\mathcal{L} = 30\ \text{ab}^{-1}$ [201]. More details on the FCC estimate can be found in App. A.2.2. In terms of parameter reach the FCC projections exceed the HL-LHC projections by another order of magnitude in the coupling.

Pseudoscalar with Higgs mediator Furthermore, we study the DIS signature with the derivative coupling models as well. The process is analogous to the scalar s replaced by the shift-symmetric scalar a

$$aN \to ag + X\,, \tag{5.68}$$

and yields the differential DIS cross section

$$\frac{d^2\hat{\sigma}_{\text{DIS}}}{dx\,dy} = \frac{g_{hgg}^2}{16\pi\,\hat{s}}\,\frac{Q^4}{\Lambda_{ha}^4}\left(\frac{Q^2+2m_a^2}{Q^2+m_h^2}\right)^2\,, \tag{5.69}$$

where $\hat{s} = xs = 2ME_a\,x$ and $Q^2 = 2ME_a\,x\,y$. We always assume the minimum suppression scale from the Higgs to invisible limit of $\Lambda_{ah} \approx 672$ GeV. In the limit $m_a \ll m_h$, the full DM DIS cross section on lead and iron give us

$$\sigma_{\text{Pb}} = 1.3 \cdot 10^{-11}\,\text{fb} \qquad \text{and} \qquad \sigma_{\text{Fe}} = 1.5 \cdot 10^{-11}\,\text{fb}\,. \tag{5.70}$$

This means that a single produced pseudoscalar a undergoes DIS in the detector with a probability of

$$P_{\text{DIS}} \approx 2.1 \cdot 10^{-23}\,. \tag{5.71}$$

Just as for the ULDM scalar Higgs portal model, The total number of expected DIS events is given by

$$N_{\text{DIS}} \approx 1.0 \cdot 10^{-15}\,. \tag{5.72}$$

is too low to be observable at the HL-LHC.

Pseudoscalar with new mediator For the pseudoscalar model with a new mediator, the light particle a is produced from the decaying mediator ϕ, which again is produced in gluon fusion. We follow the analysis of the scalar case to produce the signal, $pp \to \phi \to aa$. Our Monte Carlo study shows that as long as the mediator has a comparatively narrow width, $\Gamma_\phi/m_\phi \lesssim 10\%$, the produced DM particle a carries roughly half the mediator mass in momentum. For a weak-scale mediator mass

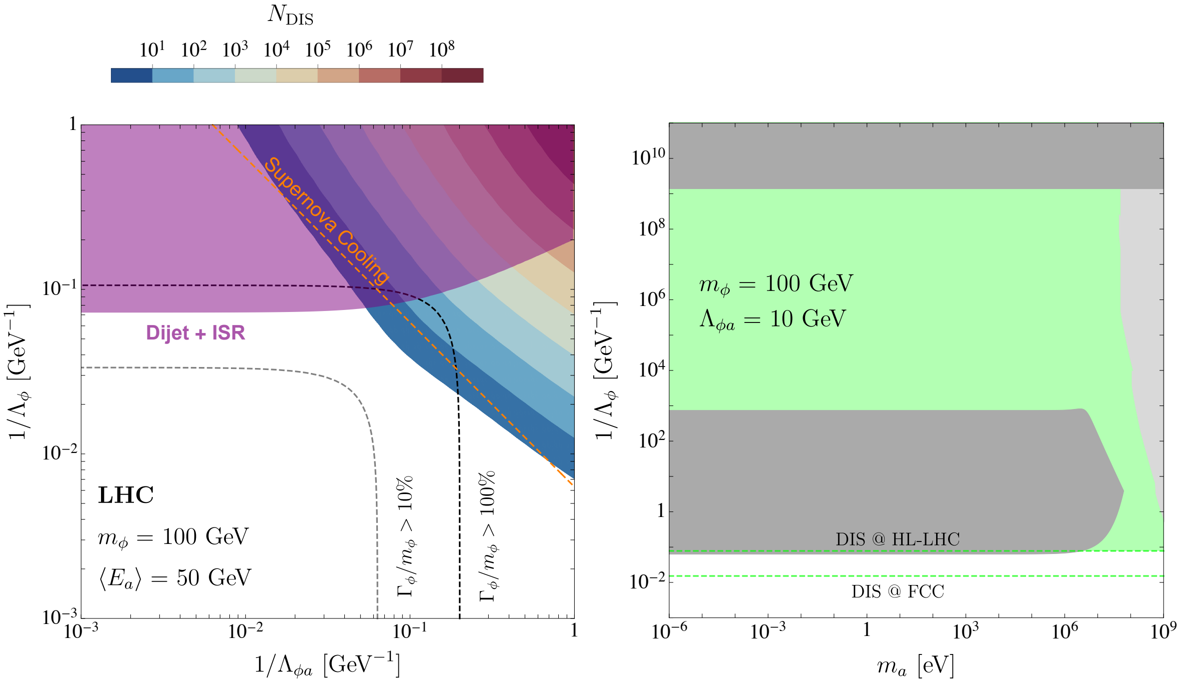

Figure 5.9: Left: number of expected DIS events in the plane of DM-mediator coupling $\Lambda_{\phi a}$ versus mediator-gluon coupling Λ_ϕ for $m_\phi = 100$ GeV [2]. Right: comparison of the projected DIS reach with the low energy constraints in terms of Λ_ϕ for fixed $\Lambda_{\phi a} = 10$ GeV [2]. Constraints which require the DM nature are shown in light grey.

$m_\phi \sim 100$ GeV this is typically enough such that a can undergo deep inelastic scattering with the nuclei in the detector material. The relevant cross section of the hard scattering process $aN \to ag + X$, reads

$$\frac{d^2\hat{\sigma}_{\text{DIS}}}{dx\,dy} = \frac{\alpha_s^2}{16\pi\,\hat{s}}\,\frac{Q^4}{\Lambda_{\phi a}^2\Lambda_\phi^2}\left(\frac{Q^2+2m_a^2}{Q^2+m_\phi^2}\right)^2 . \tag{5.73}$$

The left panel of Fig. 5.9 displays the expected number of DIS events at an ATLAS-like detector for the high luminosity run of the LHC. The grey and black dashed lines show the contours of $\Gamma_\phi/m_\phi \lesssim 10\%$ and $\lesssim 100\%$. Because of its momentum dependence in the DM-coupling, the effect of the mono-jets trigger is significantly smaller than for the scalar case. We estimate the trigger survival rate of the pseudoscalar signal to be above 70%, translating into a negligible 15% shift in the coupling reach.

Again, the right panel of Fig. 5.9 shows the corresponding HL-LHC and FCC projections in model space, compared to all other limits from Fig. 5.3. The DIS signature closes the wide gap from all other limits over 13 orders of magnitude in m_a and covers the supernova constraints, providing an independent collider probe of the cosmological observations. The FCC projections again exceed the HL-LHC projections by an order of magnitude in the coupling and provides the leading signatures for pseudoscalar DM with a weak-scale mediator.

5.3 Conclusions

Light DM is a relatively new avenue of DM model building and phenomenology. The ULDM candidate can be described by a semi-classical wave and can be embedded into a quantum field theory Lagrangian. This enables us to consider a wealth of measurements based on astrophysical observations, fifth force experiments, measurements that are sensitive to variations of fundamental constants as well as well established search strategies at the LHC and in direct detection experiments.

In particular, we have studied ULDM models with a light scalar or pseudoscalar DM particle in a mass range from well below the eV scale to the GeV scale. In both model cases the DM candidate couples to the SM via the SM-like Higgs or a new, weak-scale scalar mediator. We have studied a large number of constraints including low-energy precision measurements, BBN, supernova cooling, invisible Higgs decays, and direct DM detection. The relative impact of these constraints depends strongly on the quantum numbers of the DM and on the nature of the mediator. In pseudoscalar models with momentum-dependent couplings to the mediator, experimental searches at low energies have a negligible impact on constraining the parameter space. For scalar DM instead BBN for instance strongly constrains very light DM masses. Whereas invisible Higgs decays obviously only apply to models with a SM-like Higgs mediator, supernova constraints are very model independent. Current direct detection experiments, like Xenon1T, start cutting into the parameter space at relatively large DM masses.

Apart from existing constraints, we have studied two novel LHC signatures. On the one hand, light DM particles produced for instance in Higgs decay can annihilate with the DM background in the LHC detector. Such processes can produce pairs of photons or electrons that could be detected in LHC detectors. Unfortunately, we find the rate of this signal to be too low. On the other hand, similar to direct detection in nucleon recoils, light DM produced at the LHC can hit the nuclei in the ATLAS and CMS calorimeters and produce a *hard, displaced recoil jet*. This completely new signature of ULDM is a lot more promising and should be observable at the LHC for scalar mediator models. In a first sensitivity study, we have estimated that theses signatures could close a gap in all current constraints from $m_s = 1$ eV to the direct detection thresholds around $m_s = 100$ MeV for scalar ULDM. For pseudoscalar ULDM it covers the whole parameter space between $m_a = 10^{-6} \; ... \; 10^7$ eV, ranging from atomic spectroscopy measurements to supernova cooling all the way to large-scale direct detection experiments. This search strategy can also be immediately generalized to other very light particles, for instance neutrinos, as long as they can be produced at the LHC with sufficient energies and rates.

6 | Conclusions

Exploring the fundamental nature of DM remains one of the biggest questions of fundamental physics nowadays. Gravitational evidence for its existence has been provided by a wealth of astrophysical and cosmological observations. On galactic scales DM is needed in order to explain rotation curves of spiral galaxies. The inclusion of DM in explaining astrophysical observations has been further supported on the scale of galaxy clusters by studying the peculiar motion of cluster and cluster collisions. The CMB power spectrum has confirmed that we live in a flat Universe dominated by DM and dark energy. Moreover, the CMB yields a precise prediction of the DM abundance in the Universe.

Beyond its gravitational interaction, the behavior of DM is unknown. In the context of particle DM, DM searches have only been successful in excluding models rather than providing any signals so far. Especially, WIMPs with s-wave annihilation processes have been largely excluded by indirect detection searches in the multi-GeV region. With weak-scale DM being under pressure, it might be more likely that DM lies in other mass ranges.

In this thesis, we focused on DM candidates in the sub-GeV mass range. In Chapter 2 and 3 we have collected a variety of tests that sub-GeV DM has to pass in order to represent a valid DM candidate. Phenomenologically that mass range is relatively new. So far, experimental studies dedicated to DM have been largely based on searches that have been initially designed for weak-scale DM. Nevertheless, great experimental efforts push indirect and direct detection limits on DM masses down to the sub-GeV range. Collider experiments operate at energies around the TeV and are plagued by QCD backgrounds for low energies. For light DM masses, the major challenge for LHC studies is to find clean signatures distinguishable from QCD activities. If the DM candidate couples to the Higgs, Higgs-to-invisible searches set constraints on these couplings. Extended dark sectors often include particles that behave a lot differently from SM particles. If the lifetime of these produced particles is just as long that they can travel some distance before decaying inside the detector, this could yield exotic signatures like displaced vertices or emerging jets. For ULDM masses, the search strategy seems to be a lot different. If the DM candidate is a scalar and can be described by its wave nature, it could vary fundamental constants of nature. These variations affect the production of helium at the time of BBN, and atomic spectroscopy experiments. Furthermore, fifth force searches and the observation of the SN1987A supernova set constraints that do not require DM nature of a novel particle.

Indirect detection searches in the sub-GeV range have so far only been explored for DM annihilations into leptonic final states. The description of DM annihilations into hadronic final states have not been provided by standard Monte-Carlo tools like PYTHIA. As described in Chapter 4, a major technical problem is the theoretical description of vector meson resonances in the MeV to GeV DM mass range. In order to fully explore the sub-GeV range for indirect detection searches, we developed a Monte-Carlo-based implementation in HERWIG to describe annihilations of DM in vector mediator models. The calculations are based on data for $e^+e^- \to$ hadrons and cover all dominant hadronic final states in the sub-GeV range. We present distinct photon and lepton energy spectra that serve as a direct input to indirect detection rate calculations. The results of Chapter 4 will be available in a future version of HERWIG7 and tabulated energy spectra of exemplary DM models will included in the next DARKSUSY release. This provides the basis of fully exploring thermal DM in the sub-GeV range. Furthermore, the results can be beneficial for any BSM model depending on the description of new light vector mediator decays.

Beyond thermal DM, ULDM is an attractive candidate to describe the DM of the Universe. It can be described as a classical wave and its macroscopic de Broglie wavelength can suppress the formation of small structures. Besides its wave nature, we formulate ULDM as a quantized field in a quantum theoretical particle physics model. In Chapter 5, we systematically go through to exemplary models, a light scalar or pseudoscalar DM candidate coupling, either to the SM Higgs, or a new weak-scale mediator. We find that especially BBN puts strong constraints on scalar ULDM below 10^{-3} eV complemented by fifth force searches. Higgs-to-invisible searches and SN constraints that set largely mass-independent, are the leading bounds on ULDM coupling to the SM Higgs above 10^{-3} eV for both scalar and pseudoscalar DM candidates. Whereas SN constraints are still present for DM coupling to a new mediator, the Higgs-to-invisible constraints are absent. This opens up a large uncovered parameter space between low energy constraints below eV DM masses and direct detection bounds above 10^7 eV. That range can be tackled by a novel LHC signature that we propose. Similar to direct detection in nucleon recoils, we study the case of DM hitting the nuclei of material inside LHC detector. These interactions can produce hard, displaced jets that are fundamentally different from existing BSM searches and expected to be largely SM background free. Besides testing ULDM, the novel LHC signature can be applied to other searches of very light particles that are produced at the LHC with sufficient energy and rates.

In summary, sub-GeV DM candidates have become an attractive target of both experimental and theoretical DM searches. Just below the GeV scale, indirect detection is expected to put strong constraints on annihilating DM. The inclusion of DM processes into hadronic final states is therefore of great importance to fully explore the parameter space. We provide a Monte-Carlo based implementation of DM annihilations to fill the MeV gap for DM vector mediator models. In case of non-thermal DM, experimental searches for ULDM are mostly based on low energy experiments, and astrophysical or cosmological observations. Many of them study the properties of wave DM and its consequences on the fundamental constants of nature. Others set constraints on ULDM in fifth force experiments. Thereby, introducing a new LHC signature extends the opportunities to study very light DM. Overall, the results discussed in this thesis broaden the possibilities to study DM candidates in the sub-GeV range to finally shed a light on the nature of DM!

Acknowledgments

First of all, I am grateful to my advisor Tilman Plehn for taking me as a student in my Bachelor, Master and PhD and for all his advice and support during the past five years. Giving me the opportunity to work on an exciting Bachelor's project, encouraging me to do my Master's thesis abroad in Durham and accepting me as a PhD student did not only have a great impact on my path in physics but also on my life over the last few years.

Moreover, I would like to thank Björn Malte Schäfer for refereeing my thesis and Stephanie Hansmann-Menzemer and Hans-Christian Schultz-Coulon for completing my examination committee.

I acknowledge the Research Training Group "Particle Physics at the LHC" (DFG GRK 1940) for funding my PhD and for the financial support for my travels during my PhD.

It has been a pleasure to collaborate with many inspiring people. Special acknowledgments go to Peter Richardson for numerous inspiring and helpful Skype meetings and his huge contribution to the implementation of dark matter processes in Herwig. A big thank-you also goes to Martin Bauer and Patrick Foldenauer. Discussing exotic novel LHC signatures and working with you has been great fun!

I thank Dominic Chia, Caspar Groiseau, Ramon Winterhalder and especially Anke Biekötter and Sebastian Schenk for proofreading parts of my thesis.

I would like to thank all current and former members of the Heidelberg pheno group for all the fun coffee breaks, Marstall lunches, and moments we shared in Philosophenweg and elsewhere. In particular, I would like to thank the previous generation of PhD students, Anke Biekötter for her hospitality during my research stay in Durham, and the little tricks she played like the common effort to provide magnets and nice posters for the coffee kitchen, Sebastian Schenk for all the fun Skype chat conversations and sharing an endless list of in-jokes with me, and Patrick Foldenauer for making me feel that I am not the only Geordie-Schwoab in the group; Anastasiia Filimonova for enriching the coffee breaks with fancy sweets and fun conversations; Michel Luchmann for standing all the well-meant banter ;-); Marco Bellagente for not only carrying each other over the finish line in the NCT run but also for all the delicious cooking evenings and all the other off-time fun during my PhD; and last but not least my "Prolli<3" Ramon Winterhalder for sharing the PhD journey together, for a great time in the Proll office in Phil16, as well as many evenings together, mostly including a beer, or two ;-) .

Further, I would like to thank my flatmates for their support and letting me occupy the kitchen often enough to work there. Finally, I want to thank my family and friends for their support through all stages of my life! I am so proud to have you!

A | Appendix

The content of the appendix with all tables, plots as well as the text is fully taken from the work done in [1] and [2].

A.1 Fits to e^+e^- Annihilations with Error Envelopes

A list of all studied channels of $e^+e^- \to$ hadrons processes, their parametrizations, their data fits, and their threshold values is given in Tab. A.1. Our modelling of the e^+e^- scattering processes relies on the theory of vector meson dominance [255]. In that case the hadronic current $\langle \text{had}|J^\mu_{\text{em}}|0\rangle$ can be described by a momentum-dependence and a form-factor that includes all resonances allowed under certain isospin symmetry assumptions. The parametrization and fit values for the form-factors for the $\pi\gamma$, $\pi\pi$, 3π, $\omega\pi$, and $\eta\gamma$ final states are taken from Refs. [206, 208, 211], as implemented in the event generator PHOKHARA [256, 257], and the Born cross section formulae from the SND measurements [202, 212, 232]. For all other channels, we provide new fits. Our modelling does not take into account possible final state interactions such as rescattering [258] and Sommerfeld-effects of non-relativistic final states [259]. For example, the K-matrix approach [260] includes such interactions, e.g. the $\pi\pi \leftrightarrow KK$ rescattering above the KK threshold, with an infinite series of rescattering loops. It is used to describe, for example, three-body B-decays [261]. The only exception of using rescattering effects is the Flatté parametrization in the $\omega\pi\pi$ channel that takes into account KK threshold effects as seen below.

Channel	Data	Parametrization	fit	threshold [GeV]
$\pi\gamma$	[202]	[202]	[202]	
$\pi\pi$	[203–205]	[206]	[206]	0.280
$\pi\pi\pi$	[207]	[208]	[208]	0.420
4π	[209, 210]	[211]	own	0.560
$\omega\pi$	[212]	[212]	[212]	0.918
$p\bar{p}/n\bar{n}$	[213–230]	[231]	own	1.877
$\eta\gamma$	[232]	[232]	[232]	0.548
$\eta\pi\pi$	[233, 234]	[235]	own	0.827
$\eta'\pi\pi$	[236]	[235]	own	1.237
$\omega\pi\pi$	[236–238]	own	own	1.062
$\eta\phi$	[239, 240]	own	own	1.568
$\eta\omega$	[241]	own	own	1.331
$\phi\pi$	[239, 242]	own	own	1.160
KK	[215, 243–251]	[206]	own	0.996
$KK\pi$	[239, 242, 252–254]	own	own	1.135

Table A.1: Dominant processes contributing to $e^+e^- \to$ hadrons in the relevant energy range [1].

c_1^{1R}	-0.467(12)	c_1^{1I}	-0.385(15)	c_2^{1R}	-0.177(11)	c_2^{1I}	0.149(12)
c_3^{1R}	0.301(18)	c_3^{1I}	0.264(16)	c_1^{2R}	0.052(13)	c_1^{2I}	-3.040(21)
c_2^{2R}	-0.003(11)	c_2^{2I}	2.380(15)	c_3^{2R}	-0.348(11)	c_3^{2I}	-0.104(12)
c_1^{3R}	-7.88(47)	c_1^{3I}	5.67(29)	c_2^{3R}	10.20(10)	c_2^{3I}	-1.94(31)
c_1^{4R}	-0.8320(11)	c_1^{4I}	0.3080(12)	c_2^{4R}	0.4050(11)	c_2^{4I}	-0.2500(12)

Table A.2: Parameters of the nucleon form factor from our fit using the model describing pp production from Ref. [231].

$p\bar{p}$ (update)

The data and the fit function for this channel are given in Tab. A.1. We updated the data set used for our fit since from the input to the previous fit [231] Ref. [262] is superseded by Ref. [223], Ref. [263] by Ref. [228], and Ref. [264] by Ref. [214]. For asymmetric data uncertainties we symmetrize statistical and systematic uncertainties separately and then add both in quadrature. We refrain from a more sophisticated error analysis for instance including correlations between systematic uncertainties, since in most cases detailed information about the systematic uncertainties is either missing or the statistical uncertainty dominates. For the fit, we get $\chi^2/\text{n.d.f} = 1.069$, and the best-fit values are shown in Tab. A.2.

$\eta\pi\pi, \eta'\pi\pi$ (update)

The fit function for the $\eta\pi\pi$ and $\eta'\pi\pi$ hadronic currents are based on [235]. We re-fit the fit function to more recent data sets [233, 234] compared to those used in [235]. The fit values can be found in Tab. A.3.

KK (update)

We parametrize the hadronic current for the $K^0\bar{K}^0$ and K^+K^- channels in the same way as done in Ref. [206]. Unlike Ref. [206], we do not fix all masses and widths of the ρ, ω and ϕ states to their PDG values but let them float in the fit. Furthermore, we use an updated data set for the fit, as mentioned in Tab. A.1 and included the $\tau^- \to K_S^0\pi^-\nu_\tau$ data from Ref. [265] to better constrain the $I = 1$ component of the current. The fit values are listed in Tab. A.4. The last coupling of each resonance is calculated via Eq.(16) in Ref. [206], and we keep $\eta_\phi = 1.055$, $\gamma_\omega = 0.5$ and $\gamma_\phi = 0.2$ fixed such as in Ref. [206]. For the simultaneous fit to K^0K^0 and K^+K^- data we obtain $\chi^2/\text{n.d.f} = 1.621$.

4π (update)

For the 4π channel, we use the parametrization of Ref. [211] and fit it to more recent rate measurements for $e^+e^- \to 2\pi^0\pi^+\pi^-$ and $e^+e^- \to 2\pi^+2\pi^-$ from BaBar [209, 210]. We obtain a $\chi^2/\text{n.d.f} = 1.28$ and the fit values are listed in Tab. A.5.

Parameter	$\eta\pi\pi$	$\eta'\pi\pi$	Parameter	$\eta\pi\pi$	$\eta'\pi\pi$
m_{ρ_1} [GeV]	1.5400(39)	-	a_1	0.326(10)	0 (fixed)
m_{ρ_2} [GeV]	1.7600(58)	-	a_2	0.0115(31)	0 (fixed)
m_{ρ_3} [GeV]	2.15 (fixed)	2.110(36)	a_3	0 (fixed)	0.0200(81)
Γ_{ρ_1} [GeV]	0.356(17)	-	φ_1	π (fixed)	-
Γ_{ρ_2} [GeV]	0.113(22)	-	φ_2	π (fixed)	-
Γ_{ρ_3} [GeV]	0.32 (fixed)	0.18(11)	φ_3	0 (fixed)	π (fixed)
			χ^2/n.d.f	0.8732	0.9265

Table A.3: Fit values for the $\eta\pi\pi$ and $\eta'\pi\pi$ channels [1].

m_{ρ_0}	0.77549 (PDG)	Γ_{ρ_0}	0.1494 (PDG)	c_{ρ_0}	1.1149(24)	c_{ρ_4}	-0.0383(66)
m_{ρ_1}	1.5207(53)	Γ_{ρ_1}	0.213(14)	c_{ρ_1}	-0.0504(44)	c_{ρ_5}	0.0775 (calc.)
m_{ρ_2}	1.7410(38)	Γ_{ρ_2}	0.084(12)	c_{ρ_2}	-0.0149(32)	β_ρ	2.1968
m_{ρ_3}	1.992(15)	Γ_{ρ_3}	0.290(41)	c_{ρ_3}	-0.0390(45)	-	-
m_{ω_0}	0.78265 (PDG)	Γ_{ω_0}	0.00849 (PDG)	c_{ω_0}	1.365(44)	c_{ω_3}	1.40(27)
m_{ω_1}	1.4144(71)	Γ_{ω_1}	0.0854(71)	c_{ω_1}	-0.0278(83)	c_{ω_4}	2.8046 (calc.)
m_{ω_2}	1.6553(26)	Γ_{ω_2}	0.1603(26)	c_{ω_2}	-0.325(30)	β_ω	2.6936
m_{ϕ_0}	1.0194209(94)	Γ_{ϕ_0}	0.004253(21)	c_{ϕ_0}	0.9658(27)	c_{ϕ_3}	0.1653(50)
m_{ϕ_1}	1.5948(51)	Γ_{ϕ_1}	0.029(18)	c_{ϕ_1}	-0.0024(20)	c_{ϕ_4}	0.1195 (calc.)
m_{ϕ_2}	2.157(57)	Γ_{ϕ_2}	0.67(16)	c_{ϕ_2}	-0.1956(19)	β_ϕ	1.9452

Table A.4: Parameters for the description of KK production from our fit [1] using the model of Ref. [206]. All masses and widths are given in GeV, all other parameters are dimensionless

$\eta\phi, \eta\omega, \phi\pi$ (new)

Our first new fit is to the processes $e^+e^- \to \eta\phi, \eta\omega, \phi\pi$, where the momentum-dependent Born cross sections are

$$\sigma(s) = \frac{4\pi\alpha_{\text{em}}(s)^2}{3\hat{s}^{3/2}}\, P_f(s)\, |F|^2, \tag{A.1}$$

where $\alpha_{\text{em}}(s)$ is the fine structure constant, $P_f(s) = q^3_{\text{cm},X}$ the final-state phase space, $q_{\text{cm},X}$ the final-state particle momentum and F is the respective form factor. The resonant contributions are simply parametrized by

$$\begin{aligned} F_{\eta\omega,\eta\phi} &= \sum_i \frac{a_i e^{i\varphi_i}}{m_i^2 - \hat{s} - i m_i \Gamma_i}, \\ F_{\phi\pi} &= \sum_i \frac{a_i e^{i\varphi_i}}{m_i^2 - \hat{s} - i\sqrt{\hat{s}}\Gamma(\hat{s})}\ , \end{aligned} \tag{A.2}$$

where we take the s-dependent width $\Gamma(s)$ from Ref. [239]. All parameters and fit values for $\eta\phi$, $\eta\omega$, and $\phi\pi$ production are listed in Tab. A.6.

$\omega\pi\pi$ (new)

Next, for the $\omega\pi\pi$ channel, we use

$$\langle \omega\pi\pi | J^\mu_{\text{em}} | 0 \rangle = e g^{\mu\nu} \frac{g_{\omega''} m^2_{\omega''}}{\hat{s} - m^2_{\omega''} + i m_{\omega''}\Gamma_{\omega''}} g_{\nu\sigma} \varepsilon^\sigma_\omega \sum_{i=1,2} \text{BW}_{f_i}(q^2) \tag{A.3}$$

$\bar{m}_{\rho_1}$	1.44 (fixed)	$\bar{m}_{\rho_2}$	1.74 (fixed)	$\bar{m}_{\rho_3}$	2.12 (fixed)
$\bar{\Gamma}_{\rho_1}$	0.678(18)	$\bar{\Gamma}_{\rho_2}$	0.805(29)	$\bar{\Gamma}_{\rho_3}$	0.209(29)
$\beta_1^{a_1}$	-0.0519(56)	$\beta_2^{a_1}$	-0.0416(20)	$\beta_3^{a_1}$	-0.00189(47)
$\beta_1^{f_0}$	$7.39(0.29) \cdot 10^4$	$\beta_2^{f_0}$	$-2.62(0.19) \cdot 10^3$	$\beta_3^{f_0}$	334(87)
β_1^{ω}	-0.367(27)	β_2^{ω}	0.036(11)	β_3^{ω}	-0.00472(77)
c_{a_1}	-202.0(24)	c_{f_0}	124.0(52)	c_ω	-1.580(73)
c_ρ	-2.31(24)	χ^2	291	n.d.f	228

Table A.5: Parameters for the 4π channel for our fit [1] using the model from [211]. All masses and widths are in GeV; couplings β_i^j, ($j = a_1, f_0, \omega$ and $i = 1, 2, 3$) as well as c_ρ are dimensionless; c_{a_1} and c_{f_0} in GeV^{-2} and c_ω in GeV^{-1}.

Process	$\eta\phi$		$\eta\omega$		$\phi\pi$	
i	ϕ'	ϕ''	ω'	ω''	ρ	ρ'
m_i [GeV]	1.67 ± 0.0063	2.14 ± 0.012	1.425 [178]	1.67 ± 0.0087	0.77526 [178]	1.593 [239]
Γ_i [GeV]	0.122 ± 0.0075	0.044 ± 0.033	0.215 [178]	0.113 ± 0.016	0.1491 [178]	0.203 [239]
a_i	0.175 ± 0.0084	0.0041 ± 0.0019	0.0862 ± 0.011	0.0648 ± 0.0078	0.194 ± 0.073	0.0214 ± 0.0035
φ_i	0 (fixed)	2.19 ± 0.046	0 [241]	π [241]	0 (fixed)	121 ± 16.9 deg.
χ^2/n.d.f	0.9388		1.3332		0.9798	

Table A.6: Fit values for the $\eta\phi$, $\eta\omega$, and $\phi\pi$ channels [1].

for the hadronic current. In our energy range we only need to consider one vector meson mediator ω'', namely the $\omega(1650)$ meson. For the f_i mediator we have

$$\mathrm{BW}_{f_1}(m_{\pi\pi}) = \frac{g_{\omega''\omega\sigma} m_\sigma^2}{m_{\pi\pi}^2 - m_\sigma^2 + i m_\sigma \Gamma_\sigma} \tag{A.4}$$

where m_σ and Γ_σ are the mass and width of the σ meson and using the Flatté parametrization [266]

$$\mathrm{BW}_{f_0}(m_{\pi\pi}) = \frac{g_{\omega''\omega f_0(980)} m_{f_0(980)} \sqrt{\Gamma_0 \Gamma_{\pi\pi}}}{m_{\pi\pi}^2 - m_{f_0(980)}^2 + i m_{f_0(980)} (\Gamma_{\pi\pi} + \Gamma_{\bar{K}K}^*)} \tag{A.5}$$

with

$$\begin{aligned}
\Gamma_{\pi\pi} &= g_{\pi\pi} q_\pi(m_{\pi\pi}) \\
\Gamma_{\bar{K}K} &= \begin{cases} g_{\bar{K}K}\sqrt{(1/4)m_{\pi\pi}^2 - m_K^2}, & \text{above threshold} \\ i g_{\bar{K}K}\sqrt{m_K^2 - (1/4)m_{\pi\pi}^2}, & \text{below threshold} \end{cases} \\
\Gamma_{\bar{K}K}^* &= 0.5 \cdot (\Gamma_{\bar{K}^0 K^0} + \Gamma_{K^+K^-}) \\
\Gamma_0 &= g_{\pi\pi} q_\pi(m_f)
\end{aligned} \tag{A.6}$$

for the $f_0(980)$ meson, with parameters from Ref. [267]. If not mentioned otherwise, the parameters are set to their PDG values [178]. The σ meson contribution can be viewed as a phase space contribution to the $\omega\pi\pi$ channel more than resonant contribution. Therefore, the width is chosen to be large, see Tab. A.7.

$KK\pi$ (new)

Below 2 GeV center-of-mass energy the process $e^+e^- \to KK\pi$ is dominated by $e^+e^- \to KK^* \to K(K\pi)$ where KK^* can be either $K^0K^{*0}(890)$ or $K^\pm K^{*\mp}(890)$. We can relate the possible final states through their isospin $I = 0, 1$ and can use the following relations for the

Parameter	Fit value	PDG
$m_{\omega''}$	1.69 ± 0.00919 GeV	1.670 ± 0.03 GeV
$\Gamma_{\omega''}$	0.285 ± 0.0143 GeV	0.315 ± 0.035 GeV
m_σ	0.6 GeV	-
Γ_σ	1.0 GeV	-
$g_{\omega''\omega\sigma}$	1. (fixed)	-
$m_{f_0(980)}$	0.980 GeV	0.990 ± 0.020 GeV
$\Gamma_{f_0(980)}$	0.1 GeV	0.01-0.1 GeV
$g_{\omega''\omega f_0(980)}$	0.883 ± 0.0616	-
$g_{\omega''}$	1.63 ± 0.0598	-
χ^2/n.d.f	2.001	

Table A.7: Fit values for the $\omega\pi\pi$ channel [1].

fit value	I	$i=1$	$i=2$	$i=3$
$A_{I,i}$ in GeV^{-1}	$I=0$	0 (fixed)	0.233 ± 0.020	0.0405 ± 0.0081
	$I=1$	-2.34 ± 0.15	0.594 ± 0.023	-0.018 ± 0.013
$\varphi_{I,i}$	$I=0$	0 (fixed)	1.1E-07 $\pm$ 0.092	5.19 ± 0.34
	$I=1$	0 (fixed)	0.317 ± 0.056	2.57 ± 0.32
$m_{I,i}$ [GeV]	$I=0$	1.019461 (fixed)	1.6334 ± 0.0065	1.957 ± 0.034
	$I=1$	0.77526 (fixed)	1.465 (fixed)	1.720 (fixed)
$\Gamma_{I,i}$ [GeV]	$I=0$	0.004249 (fixed)	0.218 ± 0.013	0.267 ± 0.032
	$I=1$	0.1491 (fixed)	0.400 (fixed)	0.250 (fixed)

Table A.8: Fit values for the $KK\pi$ channel [1].

corresponding amplitudes $A_{0,1}$ [268],

$$\begin{aligned} K^+(K^-\pi^0) + K^-(K^+\pi^0): &\quad \frac{1}{\sqrt{6}}(A_0 - A_1), \\ K^0_S(K^0_L\pi^0) + K^0_L(K^0_S\pi^0): &\quad \frac{1}{\sqrt{6}}(A_0 + A_1), \\ K^0(K^-\pi^+) + \bar{K}^0(K^+\pi^-): &\quad \frac{1}{\sqrt{3}}(A_0 + A_1), \\ K^+(\bar{K}^0\pi^-) + K^-(K^0\pi^+): &\quad \frac{1}{\sqrt{3}}(A_0 - A_1)\ . \end{aligned} \tag{A.7}$$

For the amplitudes with intermediate resonances, $e^+e^- \to V \to KK^*$, we use the standard Breit-Wigner dsitribution

$$A_I = \sum_i A_{I,i} \frac{m_{I,i}^2 e^{\varphi_{I,i}}}{m_{I,i}^2 - \hat{s} - i\sqrt{\hat{s}}\Gamma_{I,i}}\ . \tag{A.8}$$

In the energy range we are dealing with, we expect the resonances to be $\phi(1680)$ and $\phi(2170)$ for $I=0$ and $\rho(1450)$ and $\rho(1700)$ for $I=1$. The lower resonances $\rho(770)$ and $\phi(1020)$ are not considered in the energy range of the fit and we set their couplings to zero. Furthermore, we fix the mass and the width of the intermediate K^* resonance to $m_{K^*} = 0.8956$ GeV and $\Gamma_{K^*} = 0.047$ GeV and use a p-wave Breit-Wigner propagator of the form

$$\mathrm{BW}_{K^*}(s) = \frac{g_{K^*K\pi} m_{K^*}^2}{m_{K^*}^2 - s - i\sqrt{s}\Gamma(s)}, \tag{A.9}$$

with the s-dependent width

$$\Gamma(s) = \Gamma_{K^*} \frac{\sqrt{s}}{m_{K^*}} \left(\frac{\beta(s, m_1, m_2)^2}{\beta(m_{K^*}, m_1, m_2)^2} \right)^{3/2}\ . \tag{A.10}$$

where m_1, m_2 are the decay products of the K^* state and

$$\beta(s, m_1, m_2) = \left(1 - \frac{(m_1+m_2)^2}{s}\right)^{1/2} \left(1 - \frac{(m_1-m_2)^2}{s}\right)^{1/2} \tag{A.11}$$

is their velocity in the rest frame of K^*. The $K^*K\pi$ coupling is given by

$$g_{K^*K\pi} = \sqrt{6\pi m_{K^*}^2/(0.5 m_{K^*} \beta(m_{K^*}^2, m_{K^\pm}, m_{\pi^\pm}))^3 \Gamma_{K^*}} = 5.37392360229\ . \tag{A.12}$$

Furthermore, we include a small $\phi\pi^0$ contribution for final states including neutral pions by adding the $\phi\pi^0$ cross section obtained by the $\phi\pi$ fit and the corresponding branching fractions BR($\phi(1020) \to$

$K_L^0 K_S^0) = 0.342$ and $\mathrm{BR}(\phi(1020) \to K^+K^-) = 0.489$. We perform a simultaneous fit to all possible final states in order to obtain the fit parameters of the amplitudes $A_{0,1}$. The fit values can be found in Tab. A.8.

We show all numerical best-fit solutions as blue lines for all final states in Figs. A.1, A.2, and A.3. The error bars on the data are dominated by statistical uncertainties. All fits describe the most recent data sets over the entire range shown.

Error bands

In addition to the central values of the relevant parameters describing the e^+e^- data we also estimate the error bands for the relevant processes. The reason is that some of the channels are rather poorly measured, and it is important to propagate these uncertainties through the analysis. Because most fit parameters are physical parameters appearing in the analytic description of the e^+e^- cross sections, such as masses or widths or rates, we do not find them suitable for a proper statistical analysis. For instance a total cross section measurement will lead to uncontrolled correlations between widely different phase space regions in the fit, where the different phase space regions are crucial to describe the dark matter spectra for a variable dark matter mass. Examples for the impact of a known form of the energy dependence of the scattering process on poorly measured phase space regions are the $\eta\pi\pi$ channel in Fig. A.1, the $\pi\pi$ channel in Fig. A.2, or the 3π channel in Fig. A.3.

Instead, we define envelopes by varying a sub-set of fit parameters around their mean value within their uncertainty provided our python IMINUIT [269,270] fit or as stated in papers. For poorly resolved peak structures as in the $\eta'\pi\pi$, $\phi\pi$, and $\eta\omega$ case or higher resonances as in $\eta\phi$ and $KK\pi$, we do not vary any widths and only some masses, since they are determined from the peak structure and bias the off-peak spectrum through correlations. The contribution of phases to our envelopes is only considered if no other set of parameters is sufficient to describe the measurement uncertainties. For channels with simple parametrizations with fixed masses and widths and floating peak cross sections and phases as in the case of $\pi\gamma$ [202] and $\eta\gamma$ [232], we vary all peak cross sections and the phases of the ϕ and ω resonance, respectively. In these cases, we see that away from the resonance region the error envelopes increase. For precisely measured phase space regions, we consider the full set of parameters describing these regions. These are usually large peak structures such as the $\phi \to KK$ and $\rho \to \pi\pi$ resonances in Fig. A.2 or the $\omega, \rho \to 3\pi$ peak around 0.78 GeV in Fig A.3. Those resolved regions turn out to be well described and are stable against variations of the parameters, so they give only small envelopes.

It can be challenging or nearly impossible to obtain consistent envelopes for some channels, where one parametrization is used for several sub-channels as in the case of KK and $p\bar{p}/n\bar{n}$. As long as the shape of the data is the same as in the case of 4π, $KK\pi$ and the ϕ resonance region in the KK channel, this does not cause any problems. Here we can assume that a parameter and its variation influence the fit curve in the same way. However, for energies above 1.4 GeV in the KK channel, the trend of the data of K^+K^- and $K^0\bar{K}^0$ is completely different. Therefore, already the fit to the data is challenging and only possible by allowing for more resonance fit parameters in the parametrization [206]. A variation of the parameter might influence both channels differently and it is not clear that an extremal value in the one case is also extremal in the other. This tension of both data sets causes too small error bands for energies above 1.8 GeV. For the $p\bar{p}/n\bar{n}$ channel, we do not have sufficient data for $n\bar{n}$ to describe this channel properly as already described in Ref. [231].

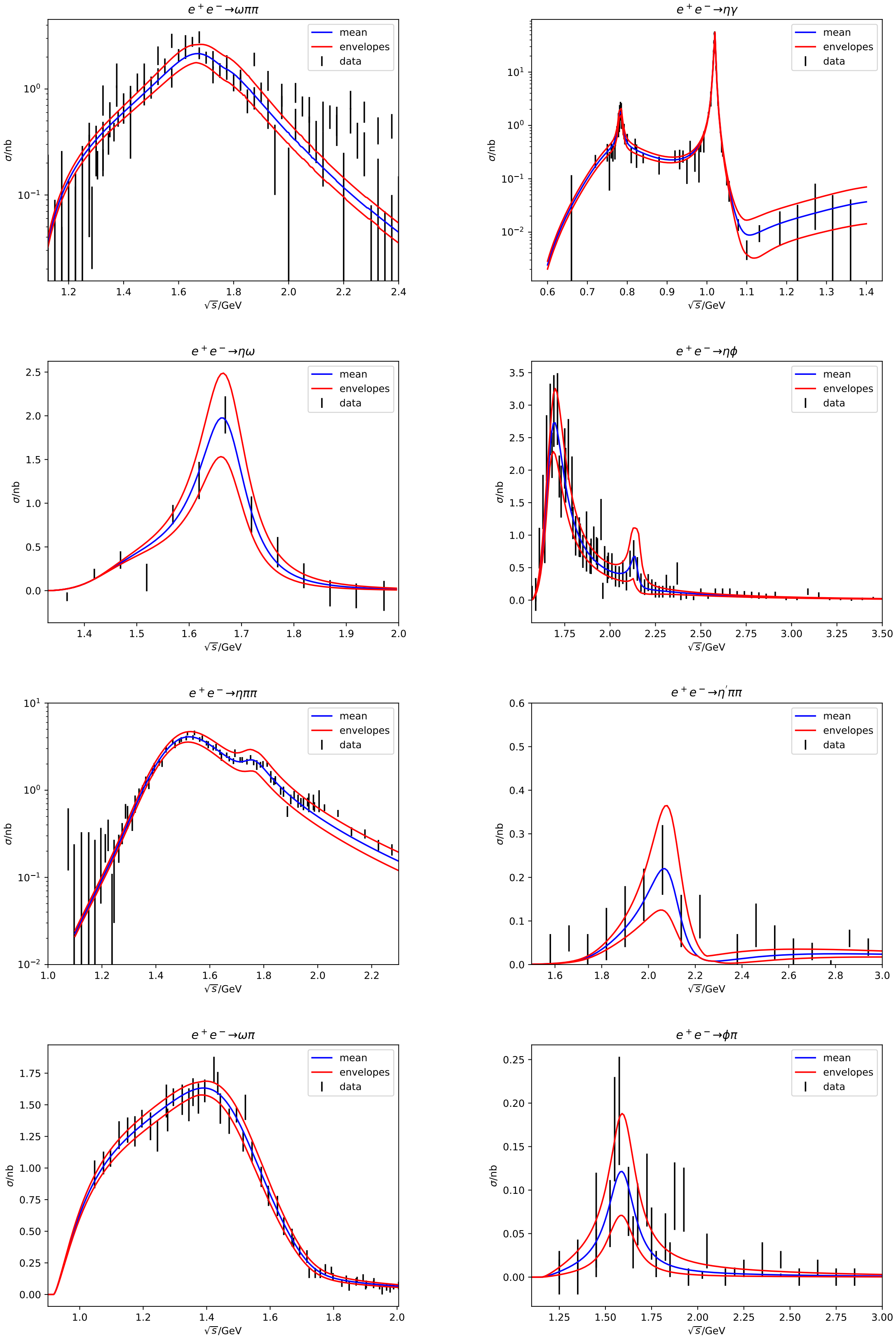

Figure A.1: Cross sections for hadronic final states with error envelopes [1].

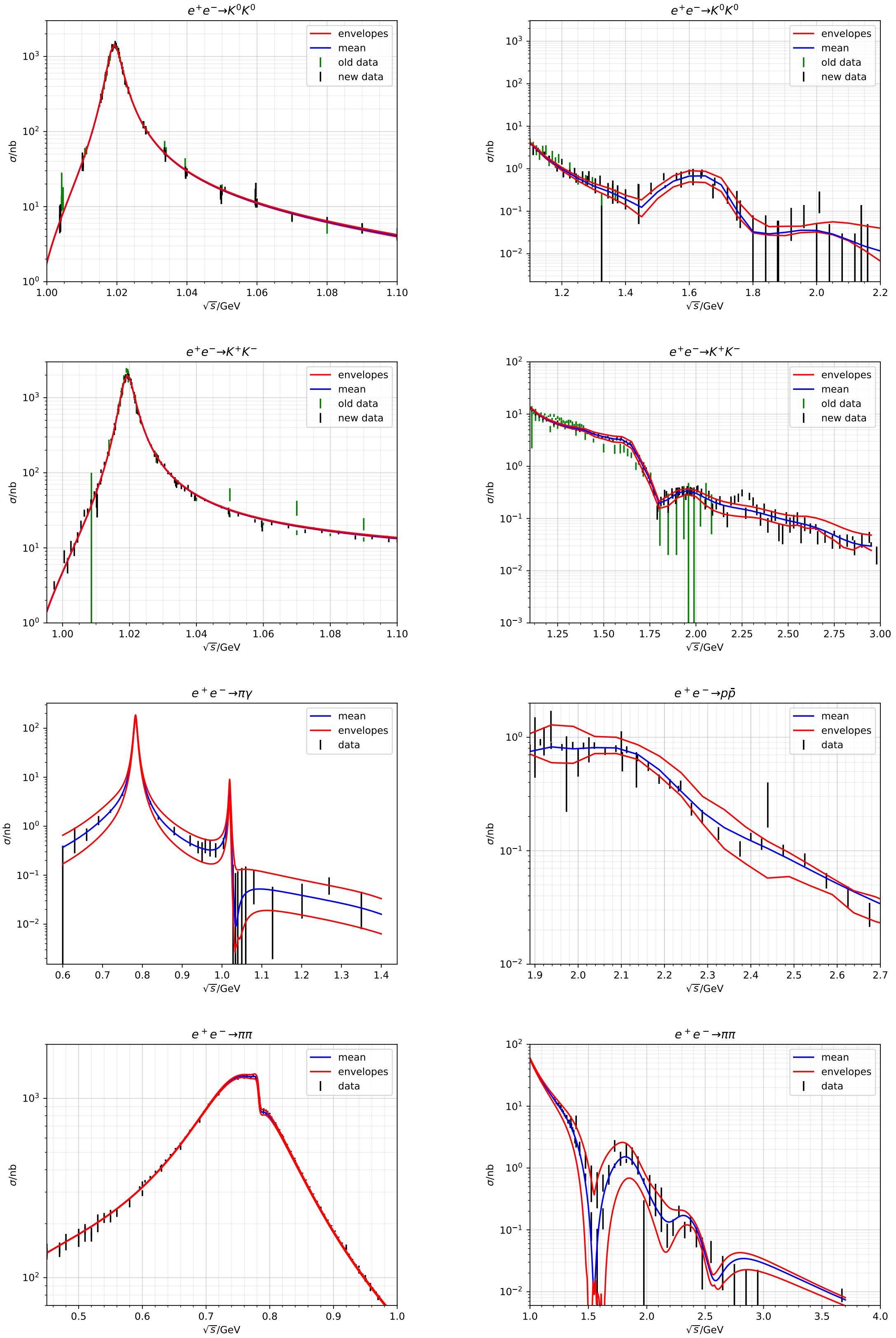

Figure A.2: Cross sections for hadronic final states with error envelopes [1].

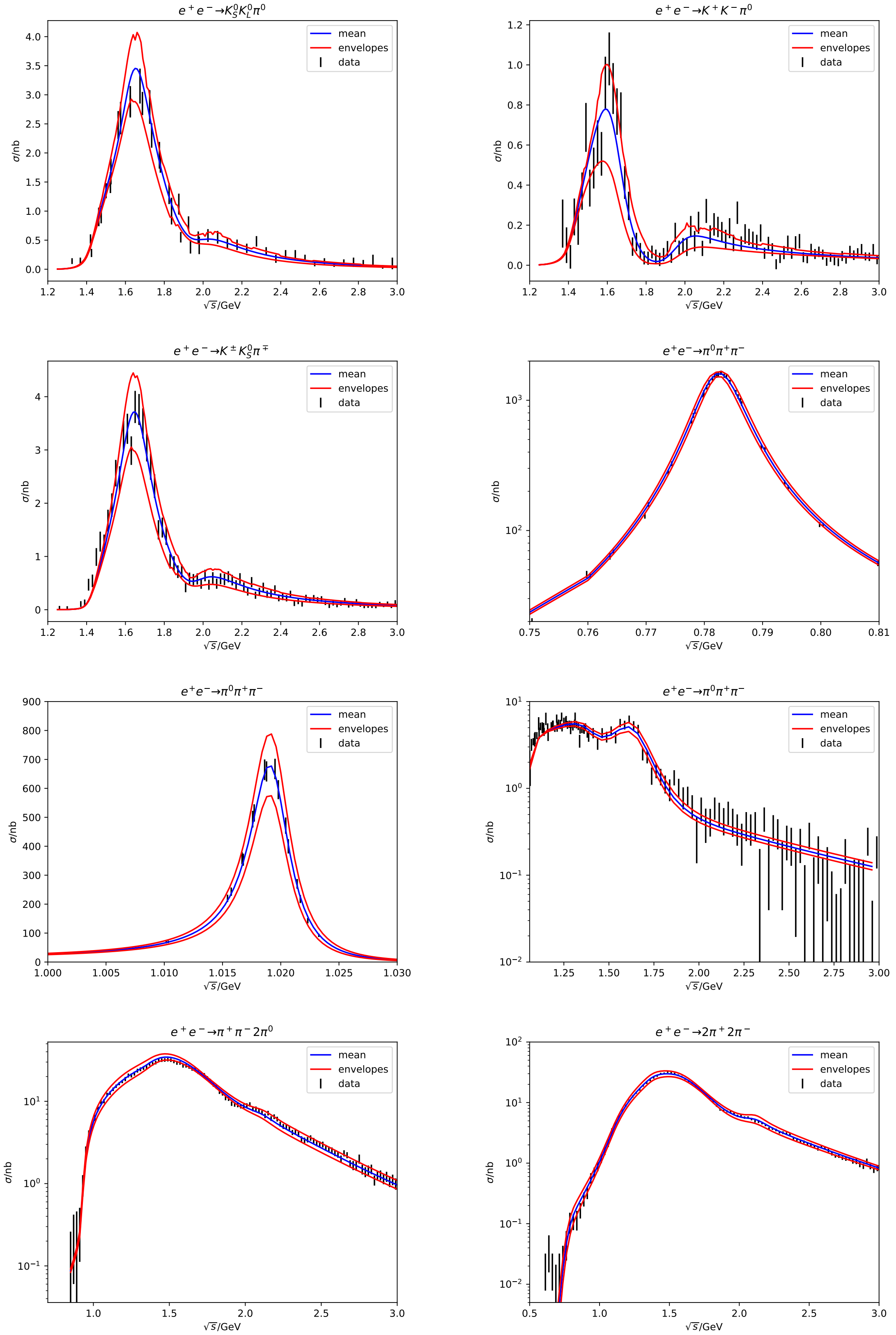

Figure A.3: cross sections for hadronic final states with error envelopes [1].

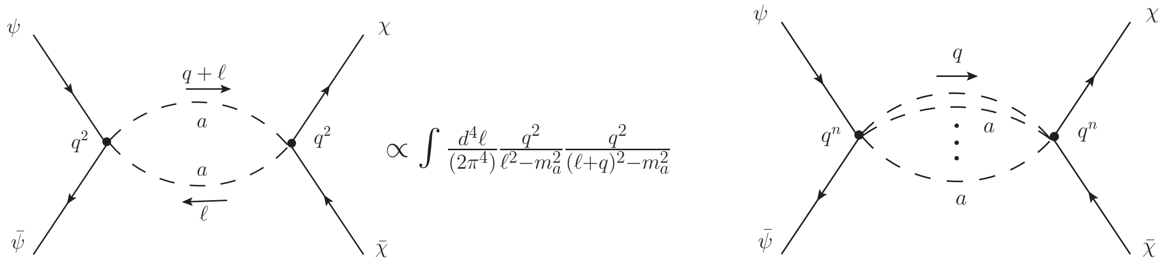

Figure A.4: Left: Two-to-two scattering via two-pseudoscalar exchange. Right: Two-to-two scattering via n-pseudoscalar exchange [2].

A.2 Very Light Dark Matter

A.2.1 Multi-Pseudoscalar Exchange

We mention in the main text that a pseudoscalar field a obeying a shift symmetry can be coupled to SM fields via derivative couplings. For long-range forces mediated by the exchange of a there are important differences between linear couplings of a to the SM and theories in which only operators with multiple a insertions feature. For a linear derivative coupling of a to an axial current,

$$\frac{\partial_\mu a}{2f}\ \bar{\psi}\gamma^\mu\gamma^5\psi + \frac{\partial_\mu a}{2f}\ \bar{\chi}\gamma^\mu\gamma^5\chi\,, \tag{A.13}$$

long-range forces between the fermions ψ and χ can be induced due to s-channel pseudoscalar exchange. The corresponding amplitude reads

$$\begin{aligned}\overline{|\mathcal{M}|^2} &= \frac{1}{64f^4}\frac{1}{(q^2-m_a^2)^2}\ \mathrm{Tr}[(\not{p}_2 - m_\psi)\not{q}\gamma^5(\not{p}_1 + m_\psi)\not{q}\gamma^5]\ \mathrm{Tr}[(\not{p}_3 + m_\chi)\not{q}\gamma^5(\not{p}_4 - m_\chi)\not{q}\gamma^5] \\ &= \frac{m_\psi^2 m_\chi^2}{f^4\left(1-2\frac{m_a^2}{q^2}+\frac{m_a^4}{q^4}\right)} = \frac{m_\psi^2 m_\chi^2}{f^4} + \mathcal{O}\left(\frac{m_a^2}{q^2}\right)\,.\end{aligned} \tag{A.14}$$

In the limit of large momentum transfer $q \gg m_a$ the leading term of the amplitude is q-independent. The leading operator for derivative couplings with two a insertions is given by (5.28),

$$\frac{\partial_\mu a\,\partial^\mu a}{2\Lambda_{ha}^2} H^\dagger H\,.$$

At low energy we can integrate out the Higgs such that the derivative Higgs portal induces interactions of the type

$$\mathcal{L} \supset \frac{1}{v}\frac{\partial_\mu a \partial^\mu a}{2\Lambda_{ha}^2}\bar{\psi}\psi + \frac{1}{v}\frac{\partial_\mu a \partial^\mu a}{2\Lambda_{ha}^2}\bar{\chi}\chi\,. \tag{A.15}$$

Similar to the case of linear derivative interactions this leads to the scattering shown in Fig. A.4. The corresponding matrix element reads

$$\begin{aligned} i\mathcal{M} &= \bar{v}(p_2)\frac{iq^2}{2v\Lambda_{ha}^2}u(p_1)\ \int \frac{d^4\ell}{(2\pi^4)}\frac{i}{\ell^2-m_a^2}\frac{i}{(\ell+q)^2-m_a^2}\ \bar{u}(p_3)\frac{iq^2}{2v\Lambda_{ha}^2}v(p_4) \\ &\propto q^4 \int dx \log\left(\frac{x\Lambda_c}{m_a^2 - x(1-x)q^2}\right)\,, \end{aligned} \tag{A.16}$$

where Λ_c is a momentum cutoff of the loop integral. Obviously, the resulting amplitude $\overline{|\mathcal{M}|^2}$ has no q-independent part and vanishes $\propto q^4$ at low momentum transfer. Operators with additional derivatives increase the power of the momentum q associated with the n-point vertex. In contrast, the overall momentum transfer flowing through the diagram will always be equal to q^2. Any long-range force mediated in such a theory is momentum-suppressed.

Theories with multi-pseudoscalar exchange are therefore qualitatively different from theories with a linearly coupled pseudoscalar. The sensitivity of experiments with small momentum exchange is strongly suppressed in the case of multi-pseudoscalar exchange which makes the case for complementary approaches beyond astrophysical and precision measurements of low-energy observables.

A.2.2 FCC Projections

Complementing our LHC analysis of DIS in scalar simplified DM models at the LHC in Sec. 5.2.2, we illustrate our results for a future circular hadron collider (FCChh) with an energy of 100 TeV and an integrated luminosity of 30 ab^{-1} [201]. Just as in Chapter 5 we generate Monte Carlo events using `MadGraph5_aMC@NLO` [200] for the DM production channels

$$pp \to \phi \to ss \; , \; aa \tag{A.17}$$

where the mediator ϕ couples to gluons through the usual dimension-5 operator. For these signals we calculate the number of expected DIS events as outlined in Sec. 5.2.2. We illustrate our result in Fig. A.5. Comparing our findings for the FCC in the simplified portal model in the left panel of Fig. A.5 with those for the LHC shown in the left panel of Fig. 5.8, we see that at the FCC we expect roughly a factor of hundred more events for a given point in the parameter space. For the pseudoscalar, derivative case we compare the right panel of Fig. A.5 to the left panel of Fig. 5.9 and find a thousand times as many events for the FCC. This is expected from the momentum enhancement shown in Eq.(5.67) compared to Eq.(5.73).

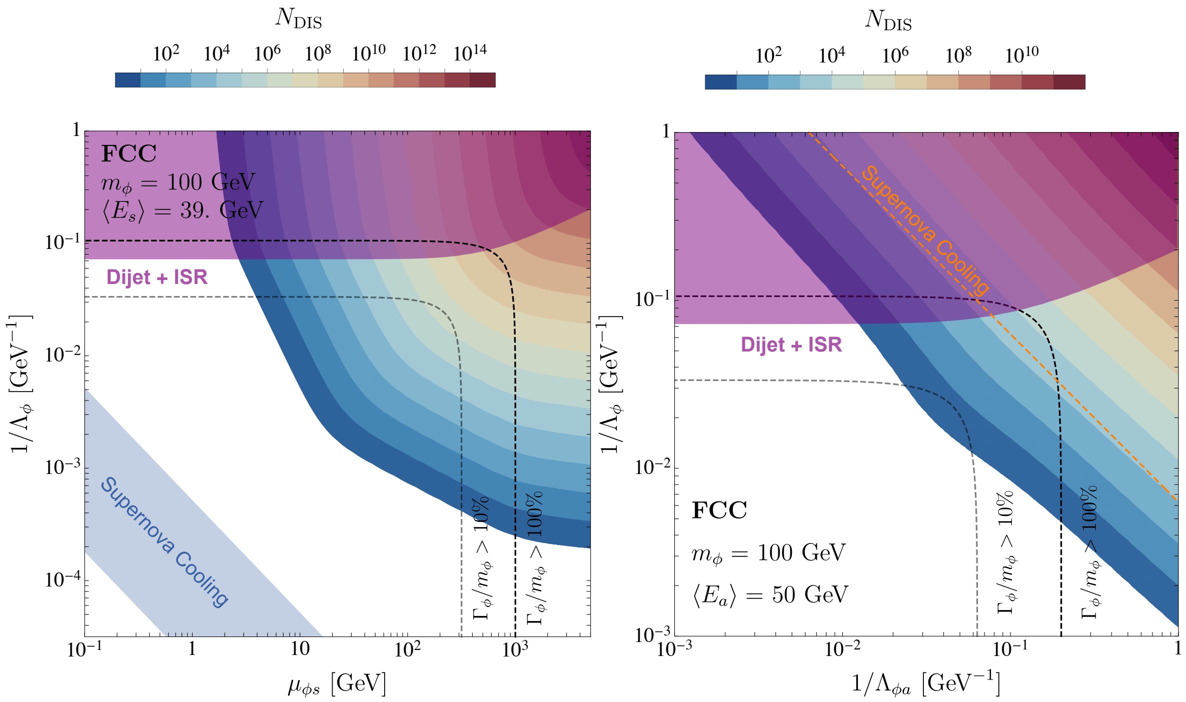

Figure A.5: Left: number of expected DIS events at the FCChh in the plane of DM-mediator coupling $\mu_{\phi s}$ versus mediator-gluon coupling Λ_ϕ for scalar ULDM with $m_\phi = 100$ GeV [2]. Right: same for the pseudoscalar ULDM [2].

References

[1] T. Plehn, P. Reimitz, and P. Richardson, "Hadronic Footprint of GeV-Mass Dark Matter," *SciPost Phys.* **8** (2020) 092, `arXiv:1911.11147 [hep-ph]`.

[2] M. Bauer, P. Foldenauer, P. Reimitz, and T. Plehn, "Light Dark Matter Annihilation and Scattering in LHC Detectors," `arXiv:2005.13551 [hep-ph]`.

[3] O. Buchmueller, C. Doglioni, and L. T. Wang, "Search for dark matter at colliders," *Nature Phys.* **13** (2017) no. 3, 217–223, `arXiv:1912.12739 [hep-ex]`.

[4] F. Kahlhoefer, "Review of LHC Dark Matter Searches," *Int. J. Mod. Phys. A* **32** (2017) no. 13, 1730006, `arXiv:1702.02430 [hep-ph]`.

[5] G. Arcadi, M. Dutra, P. Ghosh, M. Lindner, Y. Mambrini, M. Pierre, S. Profumo, and F. S. Queiroz, "The waning of the WIMP? A review of models, searches, and constraints," *Eur. Phys. J. C* **78** (2018) no. 3, 203, `arXiv:1703.07364 [hep-ph]`.

[6] S. Knapen, T. Lin, and K. M. Zurek, "Light Dark Matter: Models and Constraints," *Phys. Rev. D* **96** (2017) no. 11, 115021, `arXiv:1709.07882 [hep-ph]`.

[7] J. Gunn, B. Lee, I. Lerche, D. Schramm, and G. Steigman, "Some Astrophysical Consequences of the Existence of a Heavy Stable Neutral Lepton," *Astrophys. J.* **223** (1978) 1015–1031.

[8] F. Stecker, "The Cosmic Gamma-Ray Background from the Annihilation of Primordial Stable Neutral Heavy Leptons," *Astrophys. J.* **223** (1978) 1032–1036.

[9] Y. Zeldovich, A. Klypin, M. Khlopov, and V. Chechetkin, "Astrophysical constraints on the mass of heavy stable neutral leptons," *Sov. J. Nucl. Phys.* **31** (1980) 664–669.

[10] J. R. Ellis, R. Flores, K. Freese, S. Ritz, D. Seckel, and J. Silk, "Cosmic Ray Constraints on the Annihilations of Relic Particles in the Galactic Halo," *Phys. Lett. B* **214** (1988) 403–412.

[11] **Fermi-LAT** Collaboration, M. Ackermann *et al.*, "Searching for Dark Matter Annihilation from Milky Way Dwarf Spheroidal Galaxies with Six Years of Fermi Large Area Telescope Data," *Phys. Rev. Lett.* **115** (2015) no. 23, 231301, `arXiv:1503.02641 [astro-ph.HE]`.

[12] **Fermi-LAT, DES** Collaboration, A. Albert *et al.*, "Searching for Dark Matter Annihilation in Recently Discovered Milky Way Satellites with Fermi-LAT," *Astrophys. J.* **834** (2017) no. 2, 110, `arXiv:1611.03184 [astro-ph.HE]`.

[13] **AMS** Collaboration, M. Aguilar *et al.*, "Electron and Positron Fluxes in Primary Cosmic Rays Measured with the Alpha Magnetic Spectrometer on the International Space Station," *Phys. Rev. Lett.* **113** (2014) 121102.

[14] **AMS** Collaboration, L. Accardo *et al.*, "High Statistics Measurement of the Positron Fraction in Primary Cosmic Rays of 0.5–500 GeV with the Alpha Magnetic Spectrometer on the International Space Station," *Phys. Rev. Lett.* **113** (2014) 121101.

[15] **Planck** Collaboration, P. Ade *et al.*, "Planck 2015 results. XIII. Cosmological parameters," *Astron. Astrophys.* **594** (2016) A13, `arXiv:1502.01589 [astro-ph.CO]`.

[16] L. Bouchet, A. W. Strong, T. A. Porter, I. V. Moskalenko, E. Jourdain, and J.-P. Roques, "Diffuse emission measurement with INTEGRAL/SPI as indirect probe of cosmic-ray electrons and positrons," *Astrophys. J.* **739** (2011) 29, `arXiv:1107.0200 [astro-ph.HE]`.

[17] **e-ASTROGAM** Collaboration, M. Tavani *et al.*, "Science with e-ASTROGAM: A space mission for MeV–GeV gamma-ray astrophysics," *JHEAp* **19** (2018) 1–106, `arXiv:1711.01265 [astro-ph.HE]`.

[18] T. Sjostrand, S. Mrenna, and P. Z. Skands, "A Brief Introduction to PYTHIA 8.1," *Comput. Phys. Commun.* **178** (2008) 852–867, `arXiv:0710.3820 [hep-ph]`.

[19] G. Corcella, I. Knowles, G. Marchesini, S. Moretti, K. Odagiri, P. Richardson, M. Seymour, and B. Webber, "HERWIG 6: An Event generator for hadron emission reactions with interfering gluons (including supersymmetric processes)," *JHEP* **01** (2001) 010, `arXiv:hep-ph/0011363`.

[20] M. Cirelli, G. Corcella, A. Hektor, G. Hutsi, M. Kadastik, P. Panci, M. Raidal, F. Sala, and A. Strumia, "PPPC 4 DM ID: A Poor Particle Physicist Cookbook for Dark Matter Indirect Detection," *JCAP* **03** (2011) 051, `arXiv:1012.4515 [hep-ph]`. [Erratum: JCAP 10, E01 (2012)].

[21] G. Belanger, F. Boudjema, A. Pukhov, and A. Semenov, "MicrOMEGAs: A Program for calculating the relic density in the MSSM," *Comput. Phys. Commun.* **149** (2002) 103–120, `arXiv:hep-ph/0112278`.

[22] G. Bélanger, F. Boudjema, A. Goudelis, A. Pukhov, and B. Zaldivar, "micrOMEGAs5.0 : Freeze-in," *Comput. Phys. Commun.* **231** (2018) 173–186, `arXiv:1801.03509 [hep-ph]`.

[23] M. Backovic, K. Kong, and M. McCaskey, "MadDM v.1.0: Computation of Dark Matter Relic Abundance Using MadGraph5," *Physics of the Dark Universe* **5-6** (2014) 18–28, `arXiv:1308.4955 [hep-ph]`.

[24] F. Ambrogi, C. Arina, M. Backovic, J. Heisig, F. Maltoni, L. Mantani, O. Mattelaer, and G. Mohlabeng, "MadDM v.3.0: a Comprehensive Tool for Dark Matter Studies," *Phys. Dark Univ.* **24** (2019) 100249, `arXiv:1804.00044 [hep-ph]`.

[25] P. Gondolo, J. Edsjo, P. Ullio, L. Bergstrom, M. Schelke, and E. Baltz, "DarkSUSY: Computing supersymmetric dark matter properties numerically," *JCAP* **07** (2004) 008, `arXiv:astro-ph/0406204`.

[26] T. Bringmann, J. Edsjö, P. Gondolo, P. Ullio, and L. Bergström, "DarkSUSY 6 : An Advanced Tool to Compute Dark Matter Properties Numerically," *JCAP* **07** (2018) 033, `arXiv:1802.03399 [hep-ph]`.

[27] T. Lin, "Dark matter models and direct detection," *PoS* **333** (2019) 009, `arXiv:1904.07915 [hep-ph]`.

[28] K. M. Nollett and G. Steigman, "BBN And The CMB Constrain Light, Electromagnetically Coupled WIMPs," *Phys. Rev. D* **89** (2014) no. 8, 083508, `arXiv:1312.5725 [astro-ph.CO]`.

[29] K. M. Nollett and G. Steigman, "BBN And The CMB Constrain Neutrino Coupled Light WIMPs," *Phys. Rev. D* **91** (2015) no. 8, 083505, `arXiv:1411.6005 [astro-ph.CO]`.

[30] N. Sabti, J. Alvey, M. Escudero, M. Fairbairn, and D. Blas, "Refined Bounds on MeV-scale Thermal Dark Sectors from BBN and the CMB," *JCAP* **01** (2020) 004, `arXiv:1910.01649 [hep-ph]`.

[31] R. Hlozek, D. Grin, D. J. E. Marsh, and P. G. Ferreira, “A search for ultralight axions using precision cosmological data,” *Phys. Rev. D* **91** (2015) no. 10, 103512, `arXiv:1410.2896 [astro-ph.CO]`.

[32] Y. Stadnik and V. Flambaum, “Can dark matter induce cosmological evolution of the fundamental constants of Nature?,” *Phys. Rev. Lett.* **115** (2015) no. 20, 201301, `arXiv:1503.08540 [astro-ph.CO]`.

[33] Y. Stadnik and V. Flambaum, “Constraining scalar dark matter with Big Bang nucleosynthesis and atomic spectroscopy,” `arXiv:1504.01798 [astro-ph.CO]`.

[34] P. Brax, S. Fichet, and G. Pignol, “Bounding Quantum Dark Forces,” *Phys. Rev. D* **97** (2018) no. 11, 115034, `arXiv:1710.00850 [hep-ph]`.

[35] S. Fichet, “Quantum Forces from Dark Matter and Where to Find Them,” *Phys. Rev. Lett.* **120** (2018) no. 13, 131801, `arXiv:1705.10331 [hep-ph]`.

[36] Y. Stadnik and V. Flambaum, “Enhanced effects of variation of the fundamental constants in laser interferometers and application to dark matter detection,” *Phys. Rev. A* **93** (2016) no. 6, 063630, `arXiv:1511.00447 [physics.atom-ph]`.

[37] A. Hees, O. Minazzoli, E. Savalle, Y. V. Stadnik, and P. Wolf, “Violation of the equivalence principle from light scalar dark matter,” *Phys. Rev. D* **98** (2018) no. 6, 064051, `arXiv:1807.04512 [gr-qc]`.

[38] M. P. Jones, R. M. Potvliege, and M. Spannowsky, “Probing new physics using Rydberg states of atomic hydrogen,” *Phys. Rev. Res.* **2** (2020) no. 1, 013244, `arXiv:1909.09194 [hep-ph]`.

[39] P. Schwaller, D. Stolarski, and A. Weiler, “Emerging Jets,” *JHEP* **05** (2015) 059, `arXiv:1502.05409 [hep-ph]`.

[40] E. W. Kolb and M. S. Turner, “The Early Universe,” *Nature* **294** (1981) 521.

[41] D. Baumann, “Primordial Cosmology,” *PoS* **TASI2017** (2018) 009, `arXiv:1807.03098 [hep-th]`.

[42] **Particle Data Group** Collaboration, P. Zyla *et al.*, “Review of Particle Physics,” *PTEP* **2020** (2020) no. 8, 083C01.

[43] K. A. Olive and D. Thomas, “A light dark-matter candidate in an extended supersymmetric model,” *Nuclear Physics B* **355** (1991) no. 1, 192 – 207. `http://www.sciencedirect.com/science/article/pii/055032139190309L`.

[44] P. Gondolo and G. Gelmini, “Cosmic abundances of stable particles: Improved analysis,” *Nucl. Phys. B* **360** (1991) 145–179.

[45] L. D. Landau and L. M. Lifshitz, *Quantum Mechanics Non-Relativistic Theory, Third Edition: Volume 3.* 1981.

[46] J. Kumar and D. Marfatia, “Matrix element analyses of dark matter scattering and annihilation,” *Phys. Rev. D* **88** (2013) no. 1, 014035, `arXiv:1305.1611 [hep-ph]`.

[47] N. F. Bell, J. B. Dent, T. D. Jacques, and T. J. Weiler, “Electroweak Bremsstrahlung in Dark Matter Annihilation,” *Phys. Rev. D* **78** (2008) 083540, `arXiv:0805.3423 [hep-ph]`.

[48] V. A. Rubakov and D. S. Gorbunov, *Introduction to the Theory of the Early Universe: Hot big bang theory.* World Scientific, Singapore, 2017.

[49] P. Sørensen, “BBN Constraints on Universally Coupled Ultralight Dark Matter,”*CERN-STUDENTS-Note-2018-135* (Sep, 2018) . `https://cds.cern.ch/record/2638465`.

[50] D. J. Fixsen, "The temperature of the cosmic microwave background,"*The Astrophysical Journal* **707** (Nov, 2009) 916–920. `http://dx.doi.org/10.1088/0004-637X/707/2/916`.

[51] D. Baumann, "Inflation," in *Theoretical Advanced Study Institute in Elementary Particle Physics: Physics of the Large and the Small*, pp. 523–686. 2011. `arXiv:0907.5424 [hep-th]`.

[52] M. Bauer and T. Plehn, *Yet Another Introduction to Dark Matter: The Particle Physics Approach*, vol. 959 of *Lecture Notes in Physics*. Springer, 2019. `arXiv:1705.01987 [hep-ph]`.

[53] **Planck** Collaboration, N. Aghanim *et al.*, "Planck 2018 results. VI. Cosmological parameters," `arXiv:1807.06209 [astro-ph.CO]`.

[54] M. Markevitch, A. Gonzalez, D. Clowe, A. Vikhlinin, L. David, W. Forman, C. Jones, S. Murray, and W. Tucker, "Direct constraints on the dark matter self-interaction cross-section from the merging galaxy cluster 1E0657-56," *Astrophys. J.* **606** (2004) 819–824, `arXiv:astro-ph/0309303`.

[55] D. Clowe, M. Bradac, A. H. Gonzalez, M. Markevitch, S. W. Randall, C. Jones, and D. Zaritsky, "A direct empirical proof of the existence of dark matter," *Astrophys. J. Lett.* **648** (2006) L109–L113, `arXiv:astro-ph/0608407`.

[56] V. C. Rubin and J. Ford, W.Kent, "Rotation of the Andromeda Nebula from a Spectroscopic Survey of Emission Regions," *Astrophys. J.* **159** (1970) 379–403.

[57] V. Rubin, N. Thonnard, and J. Ford, W.K., "Rotational properties of 21 SC galaxies with a large range of luminosities and radii, from NGC 4605 /R = 4kpc/ to UGC 2885 /R = 122 kpc/," *Astrophys. J.* **238** (1980) 471.

[58] A. Bosma, "21-cm line studies of spiral galaxies. 2. The distribution and kinematics of neutral hydrogen in spiral galaxies of various morphological types.," *Astron. J.* **86** (1981) 1825.

[59] T. van Albada, J. N. Bahcall, K. Begeman, and R. Sancisi, "The Distribution of Dark Matter in the Spiral Galaxy NGC-3198," *Astrophys. J.* **295** (1985) 305–313.

[60] K. Kadota, T. Sekiguchi, and H. Tashiro, "A new constraint on millicharged dark matter from galaxy clusters," `arXiv:1602.04009 [astro-ph.CO]`.

[61] J. F. Navarro, C. S. Frenk, and S. D. White, "The Structure of cold dark matter halos," *Astrophys. J.* **462** (1996) 563–575, `arXiv:astro-ph/9508025`.

[62] T. R. Slatyer, "Indirect Detection of Dark Matter," in *Theoretical Advanced Study Institute in Elementary Particle Physics: Anticipating the Next Discoveries in Particle Physics*, pp. 297–353. 2018. `arXiv:1710.05137 [hep-ph]`.

[63] G. Giesen, M. Boudaud, Y. Génolini, V. Poulin, M. Cirelli, P. Salati, and P. D. Serpico, "AMS-02 antiprotons, at last! Secondary astrophysical component and immediate implications for Dark Matter," *JCAP* **09** (2015) 023, `arXiv:1504.04276 [astro-ph.HE]`.

[64] **AMS Collaboration** Collaboration, M. e. a. Aguilar, "First result from the alpha magnetic spectrometer on the international space station: Precision measurement of the positron fraction in primary cosmic rays of 0.5–350 gev,"*Phys. Rev. Lett.* **110** (Apr, 2013) 141102. `https://link.aps.org/doi/10.1103/PhysRevLett.110.141102`.

[65] A. Ibarra, A. S. Lamperstorfer, and J. Silk, "Dark matter annihilations and decays after the AMS-02 positron measurements," *Phys. Rev. D* **89** (2014) no. 6, 063539, `arXiv:1309.2570 [hep-ph]`.

[66] **IceCube** Collaboration, M. Aartsen *et al.*, "First observation of PeV-energy neutrinos with IceCube," *Phys. Rev. Lett.* **111** (2013) 021103, `arXiv:1304.5356 [astro-ph.HE]`.

[67] **IceCube** Collaboration, M. Aartsen *et al.*, "Evidence for High-Energy Extraterrestrial Neutrinos at the IceCube Detector," *Science* **342** (2013) 1242856, `arXiv:1311.5238 [astro-ph.HE]`.

[68] **IceCube** Collaboration, M. Aartsen *et al.*, "A combined maximum-likelihood analysis of the high-energy astrophysical neutrino flux measured with IceCube," *Astrophys. J.* **809** (2015) no. 1, 98, `arXiv:1507.03991 [astro-ph.HE]`.

[69] **IceCube** Collaboration, M. Aartsen *et al.*, "Evidence for Astrophysical Muon Neutrinos from the Northern Sky with IceCube," *Phys. Rev. Lett.* **115** (2015) no. 8, 081102, `arXiv:1507.04005 [astro-ph.HE]`.

[70] S. Ando and K. Ishiwata, "Constraints on decaying dark matter from the extragalactic gamma-ray background," *JCAP* **05** (2015) 024, `arXiv:1502.02007 [astro-ph.CO]`.

[71] K. Murase and J. F. Beacom, "Constraining Very Heavy Dark Matter Using Diffuse Backgrounds of Neutrinos and Cascaded Gamma Rays," *JCAP* **10** (2012) 043, `arXiv:1206.2595 [hep-ph]`.

[72] T. R. Slatyer and C.-L. Wu, "General Constraints on Dark Matter Decay from the Cosmic Microwave Background," *Phys. Rev. D* **95** (2017) no. 2, 023010, `arXiv:1610.06933 [astro-ph.CO]`.

[73] R. Essig, E. Kuflik, S. D. McDermott, T. Volansky, and K. M. Zurek, "Constraining Light Dark Matter with Diffuse X-Ray and Gamma-Ray Observations," *JHEP* **11** (2013) 193, `arXiv:1309.4091 [hep-ph]`.

[74] T. Cohen, K. Murase, N. L. Rodd, B. R. Safdi, and Y. Soreq, "γ -ray Constraints on Decaying Dark Matter and Implications for IceCube," *Phys. Rev. Lett.* **119** (2017) no. 2, 021102, `arXiv:1612.05638 [hep-ph]`.

[75] M. Boudaud, J. Lavalle, and P. Salati, "Novel cosmic-ray electron and positron constraints on MeV dark matter particles," *Phys. Rev. Lett.* **119** (2017) no. 2, 021103, `arXiv:1612.07698 [astro-ph.HE]`.

[76] A. Massari, E. Izaguirre, R. Essig, A. Albert, E. Bloom, and G. A. Gómez-Vargas, "Strong Optimized Conservative *Fermi*-LAT Constraints on Dark Matter Models from the Inclusive Photon Spectrum," *Phys. Rev. D* **91** (2015) no. 8, 083539, `arXiv:1503.07169 [hep-ph]`.

[77] H. Liu, W. Qin, G. W. Ridgway, and T. R. Slatyer, "Lyman-α Constraints on Cosmic Heating from Dark Matter Annihilation and Decay," `arXiv:2008.01084 [astro-ph.CO]`.

[78] O. Kalashev and M. Y. Kuznetsov, "Constraining heavy decaying dark matter with the high energy gamma-ray limits," *Phys. Rev. D* **94** (2016) no. 6, 063535, `arXiv:1606.07354 [astro-ph.HE]`.

[79] *The Pierre Auger Observatory: Contributions to the 34th International Cosmic Ray Conference (ICRC 2015).* 9, 2015. `arXiv:1509.03732 [astro-ph.HE]`.

[80] D. Kang *et al.*, "A limit on the diffuse gamma-rays measured with KASCADE-Grande," *J. Phys. Conf. Ser.* **632** (2015) no. 1, 012013.

[81] **CASA-MIA** Collaboration, M. Chantell *et al.*, "Limits on the isotropic diffuse flux of ultrahigh-energy gamma radiation," *Phys. Rev. Lett.* **79** (1997) 1805–1808, `arXiv:astro-ph/9705246`.

[82] T. R. Slatyer, N. Padmanabhan, and D. P. Finkbeiner, "CMB Constraints on WIMP Annihilation: Energy Absorption During the Recombination Epoch," *Phys. Rev. D* **80** (2009) 043526, `arXiv:0906.1197 [astro-ph.CO]`.

[83] T. R. Slatyer, "Energy Injection And Absorption In The Cosmic Dark Ages," *Phys. Rev. D* **87** (2013) no. 12, 123513, `arXiv:1211.0283 [astro-ph.CO]`.

[84] T. R. Slatyer, "Indirect dark matter signatures in the cosmic dark ages. I. Generalizing the bound on s-wave dark matter annihilation from Planck results," *Phys. Rev. D* **93** (2016) no. 2, 023527, `arXiv:1506.03811 [hep-ph]`.

[85] T. R. Slatyer, "Indirect Dark Matter Signatures in the Cosmic Dark Ages II. Ionization, Heating and Photon Production from Arbitrary Energy Injections," *Phys. Rev. D* **93** (2016) no. 2, 023521, `arXiv:1506.03812 [astro-ph.CO]`.

[86] R. K. Leane, T. R. Slatyer, J. F. Beacom, and K. C. Ng, "GeV-scale thermal WIMPs: Not even slightly ruled out," *Phys. Rev. D* **98** (2018) no. 2, 023016, `arXiv:1805.10305 [hep-ph]`.

[87] S. Seager, D. D. Sasselov, and D. Scott, "A new calculation of the recombination epoch," *Astrophys. J. Lett.* **523** (1999) L1–L5, `arXiv:astro-ph/9909275`.

[88] Y. Ali-Haimoud and C. M. Hirata, "HyRec: A fast and highly accurate primordial hydrogen and helium recombination code," *Phys. Rev. D* **83** (2011) 043513, `arXiv:1011.3758 [astro-ph.CO]`.

[89] J. Chluba and R. Thomas, "Towards a complete treatment of the cosmological recombination problem," *Mon. Not. Roy. Astron. Soc.* **412** (2011) 748, `arXiv:1010.3631 [astro-ph.CO]`.

[90] A. Lewis and A. Challinor, "Evolution of cosmological dark matter perturbations," *Phys. Rev. D* **66** (2002) 023531, `arXiv:astro-ph/0203507`.

[91] J. Lesgourgues, "The Cosmic Linear Anisotropy Solving System (CLASS) I: Overview," `arXiv:1104.2932 [astro-ph.IM]`.

[92] C. Weniger, P. D. Serpico, F. Iocco, and G. Bertone, "CMB bounds on dark matter annihilation: Nucleon energy-losses after recombination," *Phys. Rev. D* **87** (2013) no. 12, 123008, `arXiv:1303.0942 [astro-ph.CO]`.

[93] S. Galli, F. Iocco, G. Bertone, and A. Melchiorri, "CMB constraints on Dark Matter models with large annihilation cross-section," *Phys. Rev. D* **80** (2009) 023505, `arXiv:0905.0003 [astro-ph.CO]`.

[94] D. P. Finkbeiner, S. Galli, T. Lin, and T. R. Slatyer, "Searching for Dark Matter in the CMB: A Compact Parameterization of Energy Injection from New Physics," *Phys. Rev. D* **85** (2012) 043522, `arXiv:1109.6322 [astro-ph.CO]`.

[95] V. Poulin, J. Lesgourgues, and P. D. Serpico, "Cosmological constraints on exotic injection of electromagnetic energy," *JCAP* **03** (2017) 043, `arXiv:1610.10051 [astro-ph.CO]`.

[96] T. Lin, H.-B. Yu, and K. M. Zurek, "On Symmetric and Asymmetric Light Dark Matter," *Phys. Rev. D* **85** (2012) 063503, `arXiv:1111.0293 [hep-ph]`.

[97] M. Cirelli, N. Fornengo, B. J. Kavanagh, and E. Pinetti, "Integral X-ray constraints on sub-GeV Dark Matter," `arXiv:2007.11493 [hep-ph]`.

[98] J. Campbell, J. Huston, and F. Krauss, *The Black Book of Quantum Chromodynamics: A Primer for the LHC Era.* Oxford University Press, 12, 2017.

[99] S. P. Liew, M. Papucci, A. Vichi, and K. M. Zurek, "Mono-X Versus Direct Searches: Simplified Models for Dark Matter at the LHC," *JHEP* **06** (2017) 082, `arXiv:1612.00219 [hep-ph]`.

[100] **ALEPH, DELPHI, L3, OPAL, SLD, LEP Electroweak Working Group, SLD Electroweak Group, SLD Heavy Flavour Group** Collaboration, S. Schael *et al.*, "Precision electroweak measurements on the Z resonance," *Phys. Rept.* **427** (2006) 257–454, `arXiv:hep-ex/0509008`.

[101] **CMS** Collaboration, A. M. Sirunyan *et al.*, "Search for invisible decays of a Higgs boson produced through vector boson fusion in proton-proton collisions at $\sqrt{s} = 13$ TeV," *Phys. Lett. B* **793** (2019) 520–551, `arXiv:1809.05937 [hep-ex]`.

[102] **ATLAS** Collaboration, M. Aaboud *et al.*, "Combination of searches for invisible Higgs boson decays with the ATLAS experiment," *Phys. Rev. Lett.* **122** (2019) no. 23, 231801, `arXiv:1904.05105 [hep-ex]`.

[103] C. Bernaciak, T. Plehn, P. Schichtel, and J. Tattersall, "Spying an invisible Higgs boson," *Phys. Rev. D* **91** (2015) 035024, `arXiv:1411.7699 [hep-ph]`.

[104] A. Biekoetter, T. Corbett, and T. Plehn, "The Gauge-Higgs Legacy of the LHC Run II," *SciPost Phys.* **6** (2019) no. 6, 064, `arXiv:1812.07587 [hep-ph]`.

[105] M. Chala, F. Kahlhoefer, M. McCullough, G. Nardini, and K. Schmidt-Hoberg, "Constraining Dark Sectors with Monojets and Dijets," *JHEP* **07** (2015) 089, `arXiv:1503.05916 [hep-ph]`.

[106] S. Baum, R. Catena, and M. B. Krauss, "Constraints on New Scalar and Vector Mediators from LHC Dijet Searches," *J. Phys. G* **47** (2020) no. 5, 055001, `arXiv:1812.01585 [hep-ph]`.

[107] A. Filimonova and S. Westhoff, "Long live the Higgs portal!," *JHEP* **02** (2019) 140, `arXiv:1812.04628 [hep-ph]`.

[108] A. Filimonova, R. Schäfer, and S. Westhoff, "Probing dark sectors with long-lived particles at BELLE II," *Phys. Rev. D* **101** (2020) no. 9, 095006, `arXiv:1911.03490 [hep-ph]`.

[109] F. Blekman, N. Desai, A. Filimonova, A. R. Sahasransu, and S. Westhoff, "Soft displaced leptons at the LHC," `arXiv:2007.03708 [hep-ph]`.

[110] T. Marrodán Undagoitia and L. Rauch, "Dark matter direct-detection experiments," *J. Phys. G* **43** (2016) no. 1, 013001, `arXiv:1509.08767 [physics.ins-det]`.

[111] V. Nesvizhevsky, G. Pignol, and K. Protasov, "Neutron scattering and extra short range interactions," *Phys. Rev. D* **77** (2008) 034020, `arXiv:0711.2298 [hep-ph]`.

[112] S. Schlamminger, K.-Y. Choi, T. Wagner, J. Gundlach, and E. Adelberger, "Test of the equivalence principle using a rotating torsion balance," *Phys. Rev. Lett.* **100** (2008) 041101, `arXiv:0712.0607 [gr-qc]`.

[113] E. Adelberger, J. Gundlach, B. Heckel, S. Hoedl, and S. Schlamminger, "Torsion balance experiments: A low-energy frontier of particle physics," *Prog. Part. Nucl. Phys.* **62** (2009) 102–134.

[114] T. Wagner, S. Schlamminger, J. Gundlach, and E. Adelberger, "Torsion-balance tests of the weak equivalence principle," *Class. Quant. Grav.* **29** (2012) 184002, `arXiv:1207.2442 [gr-qc]`.

[115] S. Smullin, A. Geraci, D. Weld, J. Chiaverini, S. P. Holmes, and A. Kapitulnik, "New constraints on Yukawa-type deviations from Newtonian gravity at 20 microns," *Phys. Rev. D* **72** (2005) 122001, `arXiv:hep-ph/0508204`. [Erratum: Phys.Rev.D 72, 129901 (2005)].

[116] Y.-J. Chen, W. Tham, D. Krause, D. Lopez, E. Fischbach, and R. Decca, "Stronger Limits on Hypothetical Yukawa Interactions in the 30–8000 nm Range," *Phys. Rev. Lett.* **116** (2016) no. 22, 221102, `arXiv:1410.7267 [hep-ex]`.

[117] E. Salumbides, A. Schellekens, B. Gato-Rivera, and W. Ubachs, "Constraints on extra dimensions from precision molecular spectroscopy," *New J. Phys.* **17** (2015) no. 3, 033015, `arXiv:1502.02838 [physics.atom-ph]`.

[118] P. Touboul *et al.*, "MICROSCOPE Mission: First Results of a Space Test of the Equivalence Principle," *Phys. Rev. Lett.* **119** (2017) no. 23, 231101, `arXiv:1712.01176 [astro-ph.IM]`.

[119] K. Van Tilburg, N. Leefer, L. Bougas, and D. Budker, “Search for ultralight scalar dark matter with atomic spectroscopy,” *Phys. Rev. Lett.* **115** (2015) no. 1, 011802, `arXiv:1503.06886 [physics.atom-ph]`.

[120] A. Hees, J. Guéna, M. Abgrall, S. Bize, and P. Wolf, “Searching for an oscillating massive scalar field as a dark matter candidate using atomic hyperfine frequency comparisons,” *Phys. Rev. Lett.* **117** (2016) no. 6, 061301, `arXiv:1604.08514 [gr-qc]`.

[121] G. Raffelt, *Stars as laboratories for fundamental physics: The astrophysics of neutrinos, axions, and other weakly interacting particles.* 5, 1996.

[122] K. A. Olive and M. Pospelov, “Environmental dependence of masses and coupling constants,” *Phys. Rev. D* **77** (2008) 043524, `arXiv:0709.3825 [hep-ph]`.

[123] W.-Y. Keung, K.-W. Ng, H. Tu, and T.-C. Yuan, “Supernova bounds on Weinberg’s Goldstone bosons,” *Phys. Rev. D* **90** (2014) no. 7, 075014, `arXiv:1312.3488 [hep-ph]`.

[124] M. S. Turner, “Axions from SN 1987a,” *Phys. Rev. Lett.* **60** (1988) 1797.

[125] Y. Zhang, “Supernova Cooling in a Dark Matter Smog,” *JCAP* **11** (2014) 042, `arXiv:1404.7172 [hep-ph]`.

[126] G. Elor, N. L. Rodd, T. R. Slatyer, and W. Xue, “Model-Independent Indirect Detection Constraints on Hidden Sector Dark Matter,” *JCAP* **06** (2016) 024, `arXiv:1511.08787 [hep-ph]`.

[127] G. Elor, N. L. Rodd, and T. R. Slatyer, “Multistep cascade annihilations of dark matter and the Galactic Center excess,” *Phys. Rev. D* **91** (2015) 103531, `arXiv:1503.01773 [hep-ph]`.

[128] L. Bergstrom, “Radiative Processes in Dark Matter Photino Annihilation,” *Phys. Lett. B* **225** (1989) 372–380.

[129] R. Flores, K. A. Olive, and S. Rudaz, “Radiative Processes in Lsp Annihilation,” *Phys. Lett. B* **232** (1989) 377–382.

[130] E. Baltz and L. Bergstrom, “Detection of leptonic dark matter,” *Phys. Rev. D* **67** (2003) 043516, `arXiv:hep-ph/0211325`.

[131] T. Bringmann, L. Bergstrom, and J. Edsjo, “New Gamma-Ray Contributions to Supersymmetric Dark Matter Annihilation,” *JHEP* **01** (2008) 049, `arXiv:0710.3169 [hep-ph]`.

[132] L. Bergstrom, T. Bringmann, and J. Edsjo, “New Positron Spectral Features from Supersymmetric Dark Matter - a Way to Explain the PAMELA Data?,” *Phys. Rev. D* **78** (2008) 103520, `arXiv:0808.3725 [astro-ph]`.

[133] V. Barger, Y. Gao, W. Y. Keung, and D. Marfatia, “Generic dark matter signature for gamma-ray telescopes,” *Phys. Rev. D* **80** (2009) 063537, `arXiv:0906.3009 [hep-ph]`.

[134] N. F. Bell, J. B. Dent, T. D. Jacques, and T. J. Weiler, “W/Z Bremsstrahlung as the Dominant Annihilation Channel for Dark Matter,” *Phys. Rev. D* **83** (2011) 013001, `arXiv:1009.2584 [hep-ph]`.

[135] N. F. Bell, J. B. Dent, A. J. Galea, T. D. Jacques, L. M. Krauss, and T. J. Weiler, “W/Z Bremsstrahlung as the Dominant Annihilation Channel for Dark Matter, Revisited,” *Phys. Lett. B* **706** (2011) 6–12, `arXiv:1104.3823 [hep-ph]`.

[136] N. F. Bell, J. B. Dent, T. D. Jacques, and T. J. Weiler, “Dark Matter Annihilation Signatures from Electroweak Bremsstrahlung,” *Phys. Rev. D* **84** (2011) 103517, `arXiv:1101.3357 [hep-ph]`.

[137] P. Ciafaloni, M. Cirelli, D. Comelli, A. De Simone, A. Riotto, and A. Urbano, "On the Importance of Electroweak Corrections for Majorana Dark Matter Indirect Detection," *JCAP* **06** (2011) 018, `arXiv:1104.2996 [hep-ph]`.

[138] M. Garny, A. Ibarra, and S. Vogl, "Antiproton constraints on dark matter annihilations from internal electroweak bremsstrahlung," *JCAP* **07** (2011) 028, `arXiv:1105.5367 [hep-ph]`.

[139] N. F. Bell, A. J. Brennan, and T. D. Jacques, "Neutrino signals from electroweak bremsstrahlung in solar WIMP annihilation," *JCAP* **10** (2012) 045, `arXiv:1206.2977 [hep-ph]`.

[140] A. De Simone, A. Monin, A. Thamm, and A. Urbano, "On the effective operators for Dark Matter annihilations," *JCAP* **02** (2013) 039, `arXiv:1301.1486 [hep-ph]`.

[141] P. Ciafaloni, D. Comelli, A. De Simone, E. Morgante, A. Riotto, and A. Urbano, "The Role of Electroweak Corrections for the Dark Matter Relic Abundance," *JCAP* **10** (2013) 031, `arXiv:1305.6391 [hep-ph]`.

[142] N. F. Bell, Y. Cai, J. B. Dent, R. K. Leane, and T. J. Weiler, "Enhancing Dark Matter Annihilation Rates with Dark Bremsstrahlung," *Phys. Rev. D* **96** (2017) no. 2, 023011, `arXiv:1705.01105 [hep-ph]`.

[143] T. Bringmann, F. Calore, A. Galea, and M. Garny, "Electroweak and Higgs Boson Internal Bremsstrahlung: General considerations for Majorana dark matter annihilation and application to MSSM neutralinos," *JHEP* **09** (2017) 041, `arXiv:1705.03466 [hep-ph]`.

[144] F. D'Eramo and S. Profumo, "Sub-GeV Dark Matter Shining at Future MeV γ -Ray Telescopes," *Phys. Rev. Lett.* **121** (2018) no. 7, 071101, `arXiv:1806.04745 [hep-ph]`.

[145] I. Baldes, F. Calore, K. Petraki, V. Poireau, and N. L. Rodd, "Indirect searches for dark matter bound state formation and level transitions," `arXiv:2007.13787 [hep-ph]`.

[146] A. Coogan, L. Morrison, and S. Profumo, "Hazma: A Python Toolkit for Studying Indirect Detection of Sub-GeV Dark Matter," *JCAP* **01** (2020) 056, `arXiv:1907.11846 [hep-ph]`.

[147] T. Sjöstrand, S. Ask, J. R. Christiansen, R. Corke, N. Desai, P. Ilten, S. Mrenna, S. Prestel, C. O. Rasmussen, and P. Z. Skands, "An Introduction to PYTHIA 8.2," *Comput. Phys. Commun.* **191** (2015) 159–177, `arXiv:1410.3012 [hep-ph]`.

[148] T. Sjostrand, S. Mrenna, and P. Z. Skands, "PYTHIA 6.4 Physics and Manual," *JHEP* **05** (2006) 026, `arXiv:hep-ph/0603175 [hep-ph]`.

[149] L. N. Chang, O. Lebedev, W. Loinaz, and T. Takeuchi, "Constraints on gauged B - 3 L(tau) and related theories," *Phys. Rev. D* **63** (2001) 074013, `arXiv:hep-ph/0010118`.

[150] M.-C. Chen, A. de Gouvea, and B. A. Dobrescu, "Gauge Trimming of Neutrino Masses," *Phys. Rev. D* **75** (2007) 055009, `arXiv:hep-ph/0612017`.

[151] E. Salvioni, A. Strumia, G. Villadoro, and F. Zwirner, "Non-universal minimal Z' models: present bounds and early LHC reach," *JHEP* **03** (2010) 010, `arXiv:0911.1450 [hep-ph]`.

[152] H.-S. Lee and E. Ma, "Gauged $B - x_i L$ origin of R Parity and its implications," *Phys. Lett. B* **688** (2010) 319–322, `arXiv:1001.0768 [hep-ph]`.

[153] T. Araki, J. Heeck, and J. Kubo, "Vanishing Minors in the Neutrino Mass Matrix from Abelian Gauge Symmetries," *JHEP* **07** (2012) 083, `arXiv:1203.4951 [hep-ph]`.

[154] J. Heeck, M. Lindner, W. Rodejohann, and S. Vogl, "Non-Standard Neutrino Interactions and Neutral Gauge Bosons," *SciPost Phys.* **6** (2019) no. 3, 038, `arXiv:1812.04067 [hep-ph]`.

[155] T. Bringmann, A. Galea, A. Hryczuk, and C. Weniger, "Novel Spectral Features in MeV Gamma Rays from Dark Matter," *Phys. Rev. D* **95** (2017) no. 4, 043002, `arXiv:1610.04613 [hep-ph]`.

[156] P. Sikivie and Q. Yang, "Bose-Einstein Condensation of Dark Matter Axions," *Phys. Rev. Lett.* **103** (2009) 111301, `arXiv:0901.1106 [hep-ph]`.

[157] J. A. Frieman, C. T. Hill, A. Stebbins, and I. Waga, "Cosmology with ultralight pseudo Nambu-Goldstone bosons," *Phys. Rev. Lett.* **75** (1995) 2077–2080, `arXiv:astro-ph/9505060`.

[158] W. Hu, R. Barkana, and A. Gruzinov, "Cold and fuzzy dark matter," *Phys. Rev. Lett.* **85** (2000) 1158–1161, `arXiv:astro-ph/0003365`.

[159] L. Amendola and R. Barbieri, "Dark matter from an ultra-light pseudo-Goldsone-boson," *Phys. Lett. B* **642** (2006) 192–196, `arXiv:hep-ph/0509257`.

[160] D. J. Marsh and P. G. Ferreira, "Ultra-Light Scalar Fields and the Growth of Structure in the Universe," *Phys. Rev. D* **82** (2010) 103528, `arXiv:1009.3501 [hep-ph]`.

[161] L. Hui, J. P. Ostriker, S. Tremaine, and E. Witten, "Ultralight scalars as cosmological dark matter," *Phys. Rev. D* **95** (2017) no. 4, 043541, `arXiv:1610.08297 [astro-ph.CO]`.

[162] X. Du, C. Behrens, and J. C. Niemeyer, "Substructure of fuzzy dark matter haloes," *Mon. Not. Roy. Astron. Soc.* **465** (2017) no. 1, 941–951, `arXiv:1608.02575 [astro-ph.CO]`.

[163] I. Tkachev, "Coherent scalar field oscillations forming compact astrophysical objects," *Sov. Astron. Lett.* **12** (1986) 305–308.

[164] J. Goodman, "Repulsive dark matter," *New Astron.* **5** (2000) 103, `arXiv:astro-ph/0003018`.

[165] P. Peebles, "Fluid dark matter," *Astrophys. J. Lett.* **534** (2000) L127, `arXiv:astro-ph/0002495`.

[166] J. Fan, "Ultralight Repulsive Dark Matter and BEC," *Phys. Dark Univ.* **14** (2016) 84–94, `arXiv:1603.06580 [hep-ph]`.

[167] P. S. B. Dev, M. Lindner, and S. Ohmer, "Gravitational waves as a new probe of Bose–Einstein condensate Dark Matter," *Phys. Lett. B* **773** (2017) 219–224, `arXiv:1609.03939 [hep-ph]`.

[168] J.-W. Lee, "Brief History of Ultra-light Scalar Dark Matter Models," *EPJ Web Conf.* **168** (2018) 06005, `arXiv:1704.05057 [astro-ph.CO]`.

[169] S. Davidson, "Axions: Bose Einstein Condensate or Classical Field?," *Astropart. Phys.* **65** (2015) 101–107, `arXiv:1405.1139 [hep-ph]`.

[170] A. H. Guth, M. P. Hertzberg, and C. Prescod-Weinstein, "Do Dark Matter Axions Form a Condensate with Long-Range Correlation?," *Phys. Rev. D* **92** (2015) no. 10, 103513, `arXiv:1412.5930 [astro-ph.CO]`.

[171] L. Abbott and P. Sikivie, "A Cosmological Bound on the Invisible Axion," *Phys. Lett. B* **120** (1983) 133–136.

[172] J. Preskill, M. B. Wise, and F. Wilczek, "Cosmology of the Invisible Axion," *Phys. Lett. B* **120** (1983) 127–132.

[173] G. Alonso-Álvarez, J. Gehrlein, J. Jaeckel, and S. Schenk, "Very Light Asymmetric Dark Matter," *JCAP* **09** (2019) 003, `arXiv:1906.00969 [hep-ph]`.

[174] M. Pospelov, A. Ritz, and M. B. Voloshin, "Bosonic super-WIMPs as keV-scale dark matter," *Phys. Rev. D* **78** (2008) 115012, `arXiv:0807.3279 [hep-ph]`.

[175] G. Grilli di Cortona, E. Hardy, J. Pardo Vega, and G. Villadoro, "The QCD axion, precisely," *JHEP* **01** (2016) 034, `arXiv:1511.02867 [hep-ph]`.

[176] T. Plehn, "Lectures on LHC Physics," *Lect. Notes Phys.* **844** (2012) 1–193, `arXiv:0910.4182 [hep-ph]`.

[177] J. F. Gunion, H. E. Haber, G. L. Kane, and S. Dawson, *The Higgs Hunter's Guide*, vol. 80. 2000.

[178] **Particle Data Group** Collaboration, M. Tanabashi *et al.*, "Review of Particle Physics," *Phys. Rev. D* **98** (2018) no. 3, 030001.

[179] R. H. Cyburt, B. D. Fields, K. A. Olive, and T.-H. Yeh, "Big Bang Nucleosynthesis: 2015," *Rev. Mod. Phys.* **88** (2016) 015004, `arXiv:1505.01076 [astro-ph.CO]`.

[180] A. L. Erickcek, P. J. Steinhardt, D. McCammon, and P. C. McGuire, "Constraints on the Interactions between Dark Matter and Baryons from the X-ray Quantum Calorimetry Experiment," *Phys. Rev. D* **76** (2007) 042007, `arXiv:0704.0794 [astro-ph]`.

[181] J. H. Davis, "Probing Sub-GeV Mass Strongly Interacting Dark Matter with a Low-Threshold Surface Experiment," *Phys. Rev. Lett.* **119** (2017) no. 21, 211302, `arXiv:1708.01484 [hep-ph]`.

[182] **XENON** Collaboration, E. Aprile *et al.*, "Search for Light Dark Matter Interactions Enhanced by the Migdal Effect or Bremsstrahlung in XENON1T," *Phys. Rev. Lett.* **123** (2019) no. 24, 241803, `arXiv:1907.12771 [hep-ex]`.

[183] **CRESST** Collaboration, A. Abdelhameed *et al.*, "First results from the CRESST-III low-mass dark matter program," *Phys. Rev. D* **100** (2019) no. 10, 102002, `arXiv:1904.00498 [astro-ph.CO]`.

[184] **CDEX** Collaboration, Z. Liu *et al.*, "Constraints on Spin-Independent Nucleus Scattering with sub-GeV Weakly Interacting Massive Particle Dark Matter from the CDEX-1B Experiment at the China Jinping Underground Laboratory," *Phys. Rev. Lett.* **123** (2019) no. 16, 161301, `arXiv:1905.00354 [hep-ex]`.

[185] **EDELWEISS** Collaboration, E. Armengaud *et al.*, "Searching for low-mass dark matter particles with a massive Ge bolometer operated above-ground," *Phys. Rev. D* **99** (2019) no. 8, 082003, `arXiv:1901.03588 [astro-ph.GA]`.

[186] J. Jaeckel and A. Ringwald, "The Low-Energy Frontier of Particle Physics," *Ann. Rev. Nucl. Part. Sci.* **60** (2010) 405–437, `arXiv:1002.0329 [hep-ph]`.

[187] S. Weinberg, "Goldstone Bosons as Fractional Cosmic Neutrinos," *Phys. Rev. Lett.* **110** (2013) no. 24, 241301, `arXiv:1305.1971 [astro-ph.CO]`.

[188] M. Ruhdorfer, E. Salvioni, and A. Weiler, "A Global View of the Off-Shell Higgs Portal," *SciPost Phys.* **8** (2020) 027, `arXiv:1910.04170 [hep-ph]`.

[189] **CRESST** Collaboration, G. Angloher *et al.*, "Results on MeV-scale dark matter from a gram-scale cryogenic calorimeter operated above ground," *Eur. Phys. J. C* **77** (2017) no. 9, 637, `arXiv:1707.06749 [astro-ph.CO]`.

[190] S. Andreas, *Light Weakly Interacting Particles: Constraints and Connection to Dark Matter.* PhD thesis, Hamburg U., 2013.

[191] L. Marsicano, M. Battaglieri, M. Bondi', C. R. Carvajal, A. Celentano, M. De Napoli, R. De Vita, E. Nardi, M. Raggi, and P. Valente, "Dark photon production through positron annihilation in beam-dump experiments," *Phys. Rev. D* **98** (2018) no. 1, 015031, `arXiv:1802.03794 [hep-ex]`.

[192] M. Bauer, P. Foldenauer, and J. Jaeckel, “Hunting All the Hidden Photons,” *JHEP* **18** (2020) 094, `arXiv:1803.05466 [hep-ph]`.

[193] **ATLAS** Collaboration, G. Aad *et al.*, “The ATLAS Experiment at the CERN Large Hadron Collider,” *JINST* **3** (2008) S08003.

[194] K. Kovarik *et al.*, “nCTEQ15 - Global analysis of nuclear parton distributions with uncertainties in the CTEQ framework,” *Phys. Rev. D* **93** (2016) no. 8, 085037, `arXiv:1509.00792 [hep-ph]`.

[195] D. Clark, E. Godat, and F. Olness, “ManeParse : A Mathematica reader for Parton Distribution Functions,” *Comput. Phys. Commun.* **216** (2017) 126–137, `arXiv:1605.08012 [hep-ph]`.

[196] L. Harland-Lang, A. Martin, P. Motylinski, and R. Thorne, “Parton distributions in the LHC era: MMHT 2014 PDFs,” *Eur. Phys. J. C* **75** (2015) no. 5, 204, `arXiv:1412.3989 [hep-ph]`.

[197] **LHC Higgs Cross Section Working Group** Collaboration, D. de Florian *et al.*, “Handbook of LHC Higgs Cross Sections: 4. Deciphering the Nature of the Higgs Sector,” `arXiv:1610.07922 [hep-ph]`.

[198] **CMS** Collaboration, A. M. Sirunyan *et al.*, “Search for low mass vector resonances decaying into quark-antiquark pairs in proton-proton collisions at $\sqrt{s} = 13$ TeV,” *JHEP* **01** (2018) 097, `arXiv:1710.00159 [hep-ex]`.

[199] **CMS** Collaboration, A. M. Sirunyan *et al.*, “Search for low mass vector resonances decaying into quark-antiquark pairs in proton-proton collisions at $\sqrt{s} = 13$ TeV,” *Phys. Rev. D* **100** (2019) no. 11, 112007, `arXiv:1909.04114 [hep-ex]`.

[200] J. Alwall, R. Frederix, S. Frixione, V. Hirschi, F. Maltoni, O. Mattelaer, H. S. Shao, T. Stelzer, P. Torrielli, and M. Zaro, “The automated computation of tree-level and next-to-leading order differential cross sections, and their matching to parton shower simulations,” *JHEP* **07** (2014) 079, `arXiv:1405.0301 [hep-ph]`.

[201] **FCC** Collaboration, A. Abada *et al.*, “FCC-hh: The Hadron Collider: Future Circular Collider Conceptual Design Report Volume 3,” *Eur. Phys. J. ST* **228** (2019) no. 4, 755–1107.

[202] **SND** Collaboration, M. N. Achasov *et al.*, “Study of the reaction $e^+e^- \to \pi^0\gamma$ with the SND detector at the VEPP-2M collider,” *Phys. Rev.* **D93** (2016) no. 9, 092001, `arXiv:1601.08061 [hep-ex]`.

[203] **KLOE** Collaboration, F. Ambrosino *et al.*, “Measurement of $\sigma(e^+e^- \to \pi^+\pi^-\gamma(\gamma)$ and the dipion contribution to the muon anomaly with the KLOE detector,” *Phys. Lett.* **B670** (2009) 285–291, `arXiv:0809.3950 [hep-ex]`.

[204] **BaBar** Collaboration, B. Aubert *et al.*, “Precise measurement of the $e^+e^- \to \pi^+\pi^-(\gamma)$ cross section with the Initial State Radiation method at BABAR,” *Phys. Rev. Lett.* **103** (2009) 231801, `arXiv:0908.3589 [hep-ex]`.

[205] **BaBar** Collaboration, J. P. Lees *et al.*, “Precise Measurement of the $e^+e^- \to \pi^+\pi^-(\gamma)$ Cross Section with the Initial-State Radiation Method at BABAR,” *Phys. Rev.* **D86** (2012) 032013, `arXiv:1205.2228 [hep-ex]`.

[206] H. Czyz, A. Grzelinska, and J. H. Kuhn, “Narrow resonances studies with the radiative return method,” *Phys. Rev.* **D81** (2010) 094014, `arXiv:1002.0279 [hep-ph]`.

[207] **BaBar** Collaboration, B. Aubert *et al.*, “Study of $e^+e^- \to \pi^+\pi^-\pi^0$ process using initial state radiation with BaBar,” *Phys. Rev.* **D70** (2004) 072004, `arXiv:hep-ex/0408078 [hep-ex]`.

[208] H. Czyz, A. Grzelinska, J. H. Kuhn, and G. Rodrigo, “Electron-positron annihilation into three pions and the radiative return,” *Eur. Phys. J.* **C47** (2006) 617–624, `arXiv:hep-ph/0512180 [hep-ph]`.

[209] **BaBar** Collaboration, J. P. Lees *et al.*, “Initial-State Radiation Measurement of the $e^+e^- \to \pi^+\pi^-\pi^+\pi^-$ Cross Section,” *Phys. Rev.* **D85** (2012) 112009, `arXiv:1201.5677 [hep-ex]`.

[210] **BaBar** Collaboration, J. P. Lees *et al.*, “Measurement of the $e^+e^-{\to}\pi^+\pi^-\pi^0\pi^0$ cross section using initial-state radiation at BABAR,” *Phys. Rev.* **D96** (2017) no. 9, 092009, `arXiv:1709.01171 [hep-ex]`.

[211] H. Czyz, J. H. Kuhn, and A. Wapienik, “Four-pion production in tau decays and e+e- annihilation: An Update,” *Phys. Rev.* **D77** (2008) 114005, `arXiv:0804.0359 [hep-ph]`.

[212] M. N. Achasov *et al.*, “Updated measurement of the $e^+e^- \to \omega\pi^0 \to \pi^0\pi^0\gamma$ cross section with the SND detector,” *Phys. Rev.* **D94** (2016) no. 11, 112001, `arXiv:1610.00235 [hep-ex]`.

[213] **BaBar** Collaboration, J. P. Lees *et al.*, “Study of $e^+e^- \to p\bar{p}$ via initial-state radiation at BABAR,” *Phys. Rev.* **D87** (2013) no. 9, 092005, `arXiv:1302.0055 [hep-ex]`.

[214] **BESIII** Collaboration, M. Ablikim *et al.*, “Measurement of the proton form factor by studying $e^+e^- \to p\bar{p}$,” *Phys. Rev.* **D91** (2015) no. 11, 112004, `arXiv:1504.02680 [hep-ex]`.

[215] **CLEO** Collaboration, T. K. Pedlar *et al.*, “Precision measurements of the timelike electromagnetic form-factors of pion, kaon, and proton,” *Phys. Rev. Lett.* **95** (2005) 261803, `arXiv:hep-ex/0510005 [hep-ex]`.

[216] B. Delcourt *et al.*, “Study of the Reaction $e^+e^- \to p\bar{p}$ in the Total Energy Range 1925-MeV - 2180-MeV,” *Phys. Lett.* **86B** (1979) 395–398.

[217] M. Castellano, G. Di Giugno, J. W. Humphrey, E. Sassi Palmieri, G. Troise, U. Troya, and S. Vitale, “The reaction $e^+e^- \to p\bar{p}$ at a total energy of 2.1 gev,” *Nuovo Cim.* **A14** (1973) 1–20.

[218] A. Antonelli *et al.*, “The first measurement of the neutron electromagnetic form-factors in the timelike region,” *Nucl. Phys.* **B517** (1998) 3–35.

[219] **E760** Collaboration, T. A. Armstrong *et al.*, “Measurement of the proton electromagnetic form-factors in the timelike region at $8.9 - GeV^2 - 13 - GeV^2$,” *Phys. Rev. Lett.* **70** (1993) 1212–1215.

[220] **E835** Collaboration, M. Ambrogiani *et al.*, “Measurements of the magnetic form-factor of the proton in the timelike region at large momentum transfer,” *Phys. Rev.* **D60** (1999) 032002.

[221] M. Andreotti *et al.*, “Measurements of the magnetic form-factor of the proton for timelike momentum transfers,” *Phys. Lett.* **B559** (2003) 20–25.

[222] V. Punjabi *et al.*, “Proton elastic form-factor ratios to $Q^2 = 3.5\text{GeV}^2$ by polarization transfer,” *Phys. Rev.* **C71** (2005) 055202, `arXiv:nucl-ex/0501018 [nucl-ex]`. [Erratum: Phys. Rev.C71,069902(2005)].

[223] A. J. R. Puckett *et al.*, “Final Analysis of Proton Form Factor Ratio Data at $\mathbf{Q^2} = \mathbf{4.0}$, 4.8 and 5.6 GeV$^{\mathbf{2}}$,” *Phys. Rev.* **C85** (2012) 045203, `arXiv:1102.5737 [nucl-ex]`.

[224] O. Gayou *et al.*, “Measurements of the elastic electromagnetic form-factor ratio mu(p) G(Ep) / G(Mp) via polarization transfer,” *Phys. Rev.* **C64** (2001) 038202.

[225] A. J. R. Puckett *et al.*, “Recoil Polarization Measurements of the Proton Electromagnetic Form Factor Ratio to $Q^2 = 8.5\text{GeV}^2$,” *Phys. Rev. Lett.* **104** (2010) 242301, `arXiv:1005.3419 [nucl-ex]`.

[226] A. J. R. Puckett *et al.*, “Polarization Transfer Observables in Elastic Electron Proton Scattering at Q^2 =2.5, 5.2, 6.8, and 8.5 GeV^2,” *Phys. Rev.* **C96** (2017) no. 5, 055203, `arXiv:1707.08587 [nucl-ex]`. [erratum: Phys. Rev.C98,no.1,019907(2018)].

[227] **A1** Collaboration, T. Pospischil *et al.*, “Measurement of G(E(p))/G(M(p)) via polarization transfer at $Q^2 = 0.4 -$ GeV$/c^2$,” *Eur. Phys. J.* **A12** (2001) 125–127.

[228] **Jefferson Laboratory E93-038** Collaboration, B. Plaster *et al.*, “Measurements of the neutron electric to magnetic form-factor ratio G(En) / G(Mn) via the H-2(polarized-e, e-prime,polarized-n)H-1 reaction to $Q^2 = 1.45 - (\text{GeV}/c)^2$,” *Phys. Rev.* **C73** (2006) 025205, `arXiv:nucl-ex/0511025 [nucl-ex]`.

[229] **BLAST** Collaboration, E. Geis *et al.*, “The Charge Form Factor of the Neutron at Low Momentum Transfer from the H-2-polarized (e-polarized, e-prime n) p Reaction,” *Phys. Rev. Lett.* **101** (2008) 042501, `arXiv:0803.3827 [nucl-ex]`.

[230] L. Andivahis *et al.*, “Measurements of the electric and magnetic form-factors of the proton from $Q^2 = 1.75\text{GeV}/c^2$ to $8.83\text{GeV}/c^2$,” *Phys. Rev.* **D50** (1994) 5491–5517.

[231] H. Czyż, J. H. Kühn, and S. Tracz, “Nucleon form factors and final state radiative corrections to $e^+e^- \to p\bar{p}\gamma$,” *Phys. Rev.* **D90** (2014) no. 11, 114021, `arXiv:1407.7995 [hep-ph]`.

[232] M. N. Achasov *et al.*, “Study of the $e^+e^- \to \eta\gamma$ process with SND detector at the VEPP-2M e+ e- collider,” *Phys. Rev.* **D74** (2006) 014016, `arXiv:hep-ex/0605109 [hep-ex]`.

[233] M. N. Achasov *et al.*, “Measurement of the $e^+e^- \to \eta\pi^+\pi^-$ cross section with the SND detector at the VEPP-2000 collider,” *Phys. Rev.* **D97** (2018) no. 1, 012008, `arXiv:1711.08862 [hep-ex]`.

[234] **BaBar** Collaboration, J. P. Lees *et al.*, “Study of the process $e^+e^- \to \pi^+\pi^-\eta$ using initial state radiation,” *Phys. Rev.* **D97** (2018) 052007, `arXiv:1801.02960 [hep-ex]`.

[235] H. Czyż, M. Gunia, and J. H. Kühn, “Simulation of electron-positron annihilation into hadrons with the event generator PHOKHARA,” *JHEP* **08** (2013) 110, `arXiv:1306.1985 [hep-ph]`.

[236] **BaBar** Collaboration, B. Aubert *et al.*, “The $e^+e^- \to 2(\pi^+\pi^-)\pi^0, 2(\pi^+\pi^-)\eta, K^+K^-\pi^+\pi^-\pi^0 and K^+K^-\pi^+\pi^-\eta$ Cross Sections Measured with Initial-State Radiation,” *Phys. Rev.* **D76** (2007) 092005, `arXiv:0708.2461 [hep-ex]`. [Erratum: Phys. Rev.D77,119902(2008)].

[237] **CMD-2** Collaboration, R. R. Akhmetshin *et al.*, “Study of the process $e^+e^- \to \pi^+\pi^-\pi^+\pi^-\pi^0$ with CMD-2 detector,” *Phys. Lett.* **B489** (2000) 125–130, `arXiv:hep-ex/0009013 [hep-ex]`.

[238] **BaBar** Collaboration, J. P. Lees *et al.*, “Study of the reactions $e^+e^- \to \pi^+\pi^-\pi^0\pi^0\pi^0\gamma$ and $\pi^+\pi^-\pi^0\pi^0\eta\gamma$ at center-of-mass energies from threshold to 4.35 GeV using initial-state radiation,” *Phys. Rev.* **D98** (2018) no. 11, 112015, `arXiv:1810.11962 [hep-ex]`.

[239] **BaBar** Collaboration, B. Aubert *et al.*, “Measurements of $e^+e^- \to K^+K^-\eta$, $K^+K^-\pi^0$ and $K^0_s K^\pm\pi^\mp$ cross- sections using initial state radiation events,” *Phys. Rev.* **D77** (2008) 092002, `arXiv:0710.4451 [hep-ex]`.

[240] M. N. Achasov *et al.*, “Measurement of the $e^+e^- \to \eta K^+K^-$ Cross Section by Means of the SND Detector,” *Phys. Atom. Nucl.* **81** (2018) no. 2, 205–213. [Yad. Fiz.81,no.2,195(2018)].

[241] M. N. Achasov *et al.*, “Measurement of the $e^+e^- \to \omega\eta$ cross section below $\sqrt{s} = 2$ GeV,” *Phys. Rev.* **D94** (2016) no. 9, 092002, `arXiv:1607.00371 [hep-ex]`.

[242] **BaBar** Collaboration, J. P. Lees *et al.*, “Cross sections for the reactions $e^+e^- \to K^0_S K^0_L \pi^0$, $K^0_S K^0_L \eta$, and $K^0_S K^0_L \pi^0\pi^0$ from events with initial-state radiation,” *Phys. Rev.* **D95** (2017) no. 5, 052001, `arXiv:1701.08297 [hep-ex]`.

[243] M. N. Achasov *et al.*, “Measurements of the parameters of the $\phi(1020)$ resonance through studies of the processes $e^+e^- \to K^+K^-$, K_SK_L, and $\pi^+\pi^-\pi^0$,” *Phys. Rev.* **D63** (2001) 072002, `arXiv:hep-ex/0009036 [hep-ex]`.

[244] M. N. Achasov *et al.*, “Experimental study of the reaction $e^+e^- \to K_S^0K_L^0$ in the energy range $\sqrt{s} = 1.04$ GeV to 1.38 GeV,” *J. Exp. Theor. Phys.* **103** (2006) no. 5, 720–727, `arXiv:hep-ex/0606057 [hep-ex]`. [Zh. Eksp. Teor. Fiz.130,no.5,831(2006)].

[245] F. Mane, D. Bisello, J. C. Bizot, J. Buon, A. Cordier, and B. Delcourt, “Study of the Reaction $e^+e^- \to K_S^0K_L^0$ in the Total Energy Range 1.4-GeV to 2.18-GeV and Interpretation of the K^+ and K^0 Form-factors,” *Phys. Lett.* **99B** (1981) 261–264.

[246] **CMD-3** Collaboration, E. A. Kozyrev *et al.*, “Study of the process $e^+e^- \to K_S^0K_L^0$ in the center-of-mass energy range 1004–1060 MeV with the CMD-3 detector at the VEPP-2000 e^+e^- collider,” *Phys. Lett.* **B760** (2016) 314–319, `arXiv:1604.02981 [hep-ex]`.

[247] **BaBar** Collaboration, J. P. Lees *et al.*, “Cross sections for the reactions $e^+e^- \to K_S^0K_L^0$, $K_S^0K_L^0\pi^+\pi^-$, $K_S^0K_S^0\pi^+\pi^-$, and $K_S^0K_S^0K^+K^-$ from events with initial-state radiation,” *Phys. Rev.* **D89** (2014) no. 9, 092002, `arXiv:1403.7593 [hep-ex]`.

[248] **CMD-2** Collaboration, R. R. Akhmetshin *et al.*, “Measurement of $e^+e^- \to \phi \to K^+K^-$ cross section with the CMD-2 detector at VEPP-2M Collider,” *Phys. Lett.* **B669** (2008) 217–222, `arXiv:0804.0178 [hep-ex]`.

[249] **BaBar** Collaboration, J. P. Lees *et al.*, “Precision measurement of the $e^+e^- \to K^+K^-(\gamma)$ cross section with the initial-state radiation method at BABAR,” *Phys. Rev.* **D88** (2013) no. 3, 032013, `arXiv:1306.3600 [hep-ex]`.

[250] **BaBar** Collaboration, J. P. Lees *et al.*, “Study of the $e^+e^- \to K^+K^-$ reaction in the energy range from 2.6 to 8.0 GeV,” *Phys. Rev.* **D92** (2015) no. 7, 072008, `arXiv:1507.04638 [hep-ex]`.

[251] M. N. Achasov *et al.*, “Measurement of the $\mathbf{e^+e^- \to K^+K^-}$ cross section in the energy range $\sqrt{\mathbf{s}} = \mathbf{1.05 - 2.0}$ GeV,” *Phys. Rev.* **D94** (2016) no. 11, 112006, `arXiv:1608.08757 [hep-ex]`.

[252] M. N. Achasov *et al.*, “Measurement of the $\mathbf{e^+e^- \to K_SK_L}\pi^\mathbf{0}$ cross section in the energy range $\sqrt{\mathbf{s}} = \mathbf{1.3 - 2.0}$ GeV,” *Phys. Rev.* **D97** (2018) no. 3, 032011, `arXiv:1711.07143 [hep-ex]`.

[253] D. Bisello *et al.*, “Observation of an isoscalar vector meson at approximately $= 1650\text{MeV}/c^2$ in the $e^+e^- \to K\bar{K}\pi$ reaction,” *Z. Phys.* **C52** (1991) 227–230.

[254] F. Mane, D. Bisello, J. C. Bizot, J. Buon, A. Cordier, and B. Delcourt, “Study of $e^+e^- \to K_S^0K^\pm\pi^\mp$ in the 1.4-GeV to 2.18-GeV Energy Range: A New Observation of an Isoscalar Vector Meson ϕ' (1.65-GeV),” *Phys. Lett.* **112B** (1982) 178–182.

[255] H. B. O’Connell, B. C. Pearce, A. W. Thomas, and A. G. Williams, “$\rho - \omega$ mixing, vector meson dominance and the pion form-factor,” *Prog. Part. Nucl. Phys.* **39** (1997) 201–252, `arXiv:hep-ph/9501251 [hep-ph]`.

[256] G. Rodrigo, H. Czyz, J. H. Kuhn, and M. Szopa, “Radiative return at NLO and the measurement of the hadronic cross-section in electron positron annihilation,” *Eur. Phys. J.* **C24** (2002) 71–82, `arXiv:hep-ph/0112184 [hep-ph]`.

[257] H. Czyż, P. Kisza, and S. Tracz, “Modeling interactions of photons with pseudoscalar and vector mesons,” *Phys. Rev.* **D97** (2018) no. 1, 016006, `arXiv:1711.00820 [hep-ph]`.

[258] D. H. Cohen, D. Ayres, R. Diebold, S. Kramer, A. Pawlicki, and A. Wicklund, “Amplitude Analysis of the K- K+ System Produced in the Reactions pi- p —> K- K+ n and pi+ n —> K- K+ p at 6-GeV/c,” *Phys. Rev. D* **22** (1980) 2595.

[259] S. Cassel, "Sommerfeld factor for arbitrary partial wave processes," *J. Phys. G* **37** (2010) 105009, `arXiv:0903.5307 [hep-ph]`.

[260] I. Aitchison, "K-MATRIX FORMALISM FOR OVERLAPPING RESONANCES," *Nucl. Phys. A* **189** (1972) 417–423.

[261] J. H. A. Nogueira, I. Bediaga, A. B. R. Cavalcante, T. Frederico, and O. Lourenço, "*cp* violation: Dalitz interference, *cpt*, and final state interactions,"*Phys. Rev. D* **92** (Sep, 2015) 054010. `https://link.aps.org/doi/10.1103/PhysRevD.92.054010`.

[262] **Jefferson Lab Hall A** Collaboration, O. Gayou *et al.*, "Measurement of G(Ep) / G(Mp) in polarized-e p —> e polarized-p to $Q^2 = 5.6\text{GeV}^2$," *Phys. Rev. Lett.* **88** (2002) 092301, `arXiv:nucl-ex/0111010 [nucl-ex]`.

[263] **E93-038** Collaboration, R. Madey *et al.*, "Measurements of G(E)n / G(M)n from the H-2(polarized-e,e-prime polarized-n) reaction to $Q^2 = 1.45(\text{GeV}/c)^2$," *Phys. Rev. Lett.* **91** (2003) 122002, `arXiv:nucl-ex/0308007 [nucl-ex]`.

[264] **BES** Collaboration, M. Ablikim *et al.*, "Measurement of the cross section for $e^+e^- \to p\bar{p}$ at center-of-mass energies from 2.0-GeV to 3.07-GeV," *Phys. Lett.* **B630** (2005) 14–20, `arXiv:hep-ex/0506059 [hep-ex]`.

[265] **Belle** Collaboration, D. Epifanov *et al.*, "Study of $\tau^- \to K_S^0\pi^-\nu_\tau$ decay at Belle," *Phys. Lett.* **B654** (2007) 65–73, `arXiv:0706.2231 [hep-ex]`.

[266] S. M. Flatte, "Coupled - Channel Analysis of the pi eta and K anti-K Systems Near K anti-K Threshold," *Phys. Lett.* **63B** (1976) 224–227.

[267] **BES** Collaboration, M. Ablikim *et al.*, "Resonances in $J/\psi \to \phi\pi^+\pi^-$ and ϕK^+K^-," *Phys. Lett.* **B607** (2005) 243–253, `arXiv:hep-ex/0411001 [hep-ex]`.

[268] M. Davier, A. Hoecker, B. Malaescu, and Z. Zhang, "Reevaluation of the Hadronic Contributions to the Muon g-2 and to alpha(MZ)," *Eur. Phys. J.* **C71** (2011) 1515, `arXiv:1010.4180 [hep-ph]`. [Erratum: Eur. Phys. J.C72,1874(2012)].

[269] iminuit team, "iminuit – a python interface to minuit." `https://github.com/scikit-hep/iminuit`.

[270] F. James and M. Roos, "Minuit – a system for function minimization and analysis of the parameter errors and correlations,"*Computer Physics Communications* **10** (Dec., 1975) 343–367.